

University of Southampton Research Repository ePrints Soton

Copyright © and Moral Rights for this thesis are retained by the author and/or other copyright owners. A copy can be downloaded for personal non-commercial research or study, without prior permission or charge. This thesis cannot be reproduced or quoted extensively from without first obtaining permission in writing from the copyright holder/s. The content must not be changed in any way or sold commercially in any format or medium without the formal permission of the copyright holders.

When referring to this work, full bibliographic details including the author, title, awarding institution and date of the thesis must be given e.g.

AUTHOR (year of submission) "Full thesis title", University of Southampton, name of the University School or Department, PhD Thesis, pagination

UNIVERSITY OF SOUTHAMPTON
FACULTY OF PHYSICAL SCIENCES AND ENGINEERING
Physics and Astronomy

**Higgs and Collider Phenomenology of Physics Beyond the Standard
Model**

by

Matthew S. Brown

Thesis for the degree of Doctor of Philosophy

November 2013

UNIVERSITY OF SOUTHAMPTON

ABSTRACT

FACULTY OF PHYSICAL SCIENCES AND ENGINEERING

Physics and Astronomy

Doctor of Philosophy

HIGGS AND COLLIDER PHENOMENOLOGY OF PHYSICS BEYOND THE
STANDARD MODEL

by **Matthew S. Brown**

This thesis explores three classes of beyond-the-Standard Model (BSM) theories: Minimal Universal Extra Dimensions (MUED), the 4D Composite Higgs Model (4DCHM) and Technicolor. In particular, Higgs boson data from the Large Hadron Collider (LHC) is used to test the viability of these models and constrain their parameter spaces. It turns out that this provides a valuable constraint for MUED, requiring that the compactification scale R^{-1} of the theory be greater than 500 GeV. More direct searches for MUED are also considered, and the creation of a software implementation of MUED in CalcHEP is discussed. This implementation is used to determine that the tri-lepton final state is the most promising discovery signature due to the high lepton multiplicity in MUED and that the exclusion reach of MUED using this signature is up to $R^{-1} \approx 1200$ GeV with 20 fb^{-1} of data from the 8 TeV LHC. The 4DCHM is also analysed in light of the Higgs data. It is found that, once direct detection constraints are applied, the model is actually a slightly better fit to Higgs data than the Standard Model for most points in the 4DCHM parameter space considered. Finally, various Technicolor models are tested against Higgs data using a more sophisticated statistical analysis and it is found that most provide viable Higgs boson candidates with broadly Standard Model-like couplings.

Dedicated to my wonderful parents

Contents

Declaration of Authorship	xv
Acknowledgements	xvii
1 Introduction	1
2 The Standard Model	5
2.1 The SM gauge symmetry and matter content	6
2.2 Electroweak symmetry breaking and the Higgs boson	11
2.3 Incorporating fermion masses	13
2.4 Gauge fixing, Goldstones and Ghosts	13
3 Discovering and characterising the Higgs boson	17
3.1 Preliminaries	18
3.2 Higgs production and decay	19
3.3 Exclusion, discovery and characterisation	21
3.3.1 The likelihood function	21
3.3.2 Excluding a hypothesis	23
3.3.3 Quantifying a discovery	26
3.3.4 Characterising the excess	28
3.4 Log-likelihood ratios, the CL_s method, and all that	28
3.4.1 Test statistics and hypothesis testing	29
3.4.2 Choosing the test statistic	31
3.4.3 The CL_s method	32
3.4.4 Systematic and theory uncertainties	33
3.4.5 LHC procedure for limits and discovery	34
3.5 Higgs phenomenology in theories beyond the Standard Model	35
4 Minimal Universal Extra Dimensions	39
4.1 Compactification	40
4.2 Chirality from orbifolding	41
4.3 Field content and the Lagrangian	44
4.4 Lorentz symmetry, KK number and KK parity	46
4.5 Implementing MUED in LanHEP and CalcHEP	48
4.5.1 Loop-corrected masses	49
4.5.2 Diagonalising the fermions	53
4.5.3 Diagonalising the bosons	54
4.5.4 Implementation details	55

4.6	Mass spectrum and decay modes	56
4.7	Unitarity of WW scattering	61
4.8	Discovering MUED at the LHC: the tri-lepton signature	61
4.9	Constraining MUED using LHC Higgs boson searches	62
4.9.1	Evaluation of amplitudes for Higgs production and decay in MUED	63
4.9.2	Calculating the MUED cross-section enhancement	68
4.9.3	Constraining the parameter space	71
4.9.3.1	Using one channel	71
4.9.3.2	Statistical combination	71
4.9.4	Results	73
4.10	Conclusions	77
5	The 4D Composite Higgs Model	79
5.1	The hierarchy problem	79
5.2	Composite Higgs models	81
5.3	The 4D composite Higgs model: particle content and parameter space	82
5.4	Signal enhancement factors from the Lagrangian	85
5.5	Statistical procedure	86
5.6	Results	87
5.7	Conclusions	93
6	Technicolor	95
6.1	Electroweak gauge boson masses through strong dynamics	96
6.2	Fermion masses and Extended Technicolor	97
6.3	The Technicolor Higgs	99
6.4	The effective Lagrangian and the loop couplings	99
6.5	Statistical Procedure	102
6.5.1	Assumptions and approximations	106
6.6	Results	107
6.6.1	Minimal Walking Technicolor	109
6.6.2	Weinberg-Susskind, partially-gauged and two-scale Technicolor	111
6.6.3	One-family Technicolor	112
6.7	Conclusions	114
7	Conclusions and outlook	117
A	MUED Higgs calculation	119
A.1	Feynman rules	119
A.1.1	Propagators	119
A.1.2	Vertices	120
A.2	$gg \rightarrow H$ amplitude	122
A.2.1	Specialising couplings	124
A.2.1.1	Standard Model	124
A.2.1.2	Including KK modes	124
A.3	$H \rightarrow \gamma\gamma$ amplitude	125
A.3.1	Fermion contribution	125
A.3.2	Gauge boson contribution	126
A.3.3	Summing the diagrams	130

A.3.4	Scalar contribution	131
A.4	P-V functions and conventions	132
A.4.1	Three-point PV function	132
A.4.2	Two-point PV function	132
A.4.3	PV Reduction	133
References		135

List of Figures

3.1	Important Higgs production processes as a function of m_H	20
3.2	Branching ratios and total width of the Higgs as a function of m_H	21
3.3	Reproduction of figure from ATLAS Higgs discovery paper showing Bazil band exclusion plot, local p -value for discovery and best-fit signal strength, each as function of hypothesised m_H	25
3.4	Reproduction of figure from CMS paper showing best-fit signal strengths in five decay channels for $m_H = 125.7$ GeV	29
3.5	Possible choices of critical regions	30
3.6	Leading order diagrams for $H \rightarrow \gamma\gamma$ and $H \rightarrow gg$ in the Standard Model	36
4.1	Turning a circle S^1 into an S^1/\mathbb{Z}_2 orbifold.	42
4.2	Example of a KK number-violating process	46
4.3	Mass spectrum of MUED at tree and one-loop level	57
4.4	Variation of the $n = 1$ particle masses as a function of Λ , both quantities given in units of the compactification scale	58
4.5	Variation of the $n = 1$ particle masses as a function of R^{-1}	59
4.6	Decay chains for the first KK gluon for two R^{-1} benchmarks.	60
4.7	Comparison of unitary behaviour of $WW \rightarrow W^{(n)}W^{(n)}$ scattering between our model and the existing DKM model	61
4.8	Exclusion and discovery potentials of MUED for different LHC energies and integrated luminosities	62
4.9	SM $gg \rightarrow H$ and $H \rightarrow \gamma\gamma$ amplitudes as functions of m_H together with the relative amplitudes in MUED	69
4.10	MUED cross-section enhancements for different values of R^{-1} as a function of m_H for $\gamma\gamma$ and W^+W^-/ZZ channels	70
4.11	95% CL exclusion of MUED parameter space from combined ATLAS and CMS Higgs search limits in $\gamma\gamma$, W^+W^- and ZZ channels. The second figure shows this limit combined with limits from other considerations	74
4.12	Variation with respect to R^{-1} of the MUED cross-sections for $gg \rightarrow H \rightarrow \gamma\gamma$, $gg \rightarrow H \rightarrow W^+W^-/ZZ$ and $W^+W^-/ZZ \rightarrow H \rightarrow \gamma\gamma$ channels relative to the SM for $m_H = 125$ GeV, with and without loop-corrected masses	75
4.13	Update of Figure 4.11 with new data	76
5.1	Limits on the masses and production cross-sections of T_1 and B_1 from CMS direct t' and b' searches	84
5.2	Correlation between $\mu_{\gamma\gamma}$ and μ_{VV} for scan with $f = 1$ TeV and $g_* = 2$	88
5.3	κ_H values as functions of m_{T_1} and m_{B_1} in the 4DCHM for $f = 1$ TeV and $g_* = 2$	90

5.4	κ_g values as functions of m_{T_1} and m_{B_1} in the 4DCHM for $f = 1$ TeV and $g_* = 2$	91
5.5	$\kappa_{\gamma\gamma}$ values as functions of m_{T_1} and m_{B_1} in the 4DCHM for $f = 1$ TeV and $g_* = 2$	91
5.6	Comparison of the μ 's from Equation 5.10 with the measured experimental values by ATLAS and CMS in the 4DCHM for all benchmark points in f and g_*	92
5.7	χ^2 fit in the 4DCHM for all benchmark points in f and g_*	93
6.1	Estimate of $ a_{\sigma\gamma\gamma} $ ($\pm 1\sigma$) from the $\Gamma_{\sigma \rightarrow \gamma\gamma}$ partial width, as a function of the constituent u and d quark masses.	102
6.2	68% CL (and 95% CL in the ATLAS case) contours, comparing our fit (dotted lines) to official ATLAS and CMS fits.	104
6.3	2σ exclusion contours for the $SU(3)_{2S}$ MWT model (NMWT) in the $(c_t, a_{H\gamma\gamma})$ plane	110
6.4	2σ exclusion contours for the $SU(2)_{\text{Adj}}$ MWT model (with three hypercharge assignments) and $SU(3)_{\text{Adj}}$ MWT model	111
6.5	2σ exclusion contours of WSTC with one and two weak technidoublets and different numbers of technicolours and hypercharge assignments	112
6.6	2σ exclusion contours for one-family Technicolor (OFTC) with $N_{\text{TC}} = 2$ in three planes of interest	114

List of Tables

2.1	Matter content of one of the three generations of the Standard Model fermions	7
4.1	Matter content of MUED	45
5.1	Particle content of the 4DCHM, showing the EM and colour charges. . . .	82
5.2	Parameters in the 4DCHM	82
5.3	Summary of the LHC measurements of some μ parameters from ATLAS and CMS data	88
6.1	Extra particle content of Technicolor theories under consideration	108
6.2	Loop factors for the Technicolor contribution to $g_{H\gamma\gamma}$ and the value of the “naive” S parameter for the TC theories under consideration	111

Declaration of Authorship

I, **Matthew S. Brown**, declare that the thesis entitled *Higgs and Collider Phenomenology of Physics Beyond the Standard Model* and the work presented in the thesis are both my own, and have been generated by me as the result of my own original research. I confirm that:

- this work was done wholly or mainly while in candidature for a research degree at this University;
- where any part of this thesis has previously been submitted for a degree or any other qualification at this University or any other institution, this has been clearly stated;
- where I have consulted the published work of others, this is always clearly attributed;
- where I have quoted from the work of others, the source is always given. With the exception of such quotations, this thesis is entirely my own work;
- I have acknowledged all main sources of help;
- where the thesis is based on work done by myself jointly with others, I have made clear exactly what was done by others and what I have contributed myself;
- parts of this work have been published as: [1, 2, 3, 4, 5, 6]

Signed:.....

Date:.....

Acknowledgements

First, I would like to thank my supervisor, Dr Alexander Balyaev, for his encouragement, guidance and support throughout the course of my PhD.

I am grateful to all those with whom I have collaborated, in particular to Jesús Moreno and Chloé Papineau for their hospitality and for making my stays in Madrid so stimulating.

Thank you to all of my Southampton colleagues for the inspiration, guidance and laughter. Thanks to Ken Mimasu for always being willing to help, and to Patrik Svantesson for advice on all things CalcHEP. I am of course thankful to James Lyon for his (frankly terrifying) ability to always know the answer to any question I had.

Special thanks go to Daniele Barducci for putting up with my incessant questioning and helping me to understand the intricacies of the 4D Composite Higgs Model.

Finally, thank you to my family and friends for their unwavering support.

Chapter 1

Introduction

The Standard Model of particle physics (SM) surely stands as one of mankind's greatest achievements. It was completed in two parts. First, Weinberg's 1967 paper [7] combined Glashow's [8] electroweak (EW) theory of massless vector bosons with the Higgs mechanism [9, 10] to explain weak decay. Once it had been shown [11, 12, 13] in 1972 that non-Abelian gauge theories could be renormalisable, the quark model of the hadrons was quickly formulated as a gauge theory involving gluons, called QCD, and the Standard Model was born.

The Standard Model has been hugely successful since its creation. It predicted the existence of the W boson, extending Fermi's theory of beta decay to render it unitary, and also predicted a related particle, the Z boson, and its attendant neutral current interactions. It successfully anticipated the charm quark, required by the GIM mechanism to explain the experimental lack of flavour changing neutral current interactions (FCNCs) and also the top and bottom quarks in order to explain observed CP violation. Finally, it predicted the existence of the Higgs boson, which was finally discovered on 4th July 2012 by the ATLAS [14] and CMS [15] experimental collaborations at the Large Hadron Collider (LHC). It is not just the existence of particles: the SM has correctly predicted the outcome of (almost) every experiment ever performed to test it and it is remarkable that a theory built from such simple symmetry principles can describe the almost overwhelmingly complex reality of particle interactions.

So, the Standard Model a successful theory, but it is not a Theory of Everything. Most obviously, no-one has proven that it is possible to incorporate Einstein's theory of gravity, General Relativity, into a renormalisable quantum field theory. Phenomenologically, this is not a serious problem for the foreseeable future: gravity and the SM can be combined into an effective quantum field theory that only ceases to be reliable when probing energies above the Planck scale ($\sim 10^{19}$ GeV). For comparison, the LHC, the most powerful particle collider ever produced, will operate at a peak energy of 14 TeV, and the highest particle collision energy ever recorded in nature [16] was 3×10^{11} GeV.

Nevertheless, for a truly complete theory of nature one must incorporate gravity consistently at all energies. String theory, with its requisite extra dimensions of space, is (arguably) the most promising framework for a consistent quantum theory of gravity and it could lead to interesting and measurable effects, even at experimentally accessible energy scales.

Another problem with the SM is the observed *acceleration* in the expansion of the universe. This could be explained by the quantum fields in empty space having a nonzero energy density (so-called “Dark Energy”). It is often stated that the SM predicts a vacuum energy 600 orders of magnitude too large to explain the acceleration, although such calculations make assumptions about the behaviour of gravity at high energies, meaning they should be interpreted carefully.

Also within astronomy, numerous observations of gravitational effects lead us to believe that there must be huge amounts of “Dark Matter”, matter that interacts gravitationally but that cannot be observed optically, in the universe. Explanations completely within the SM, such as the DM being dense, isolated clumps of cold, ordinary matter existing in the halos of galaxies (massive compact halo objects, or “MACHOs”), are very hard to reconcile with observations of gravitational microlensing. The most popular hypothesis is that DM is formed from new weakly interacting massive particles (WIMPs), about which the Standard Model has nothing to say. Another issue is the problem of Baryogenesis: why is there so much more matter than antimatter in the universe? This asymmetry requires *CP* violation higher than that contained in the Standard Model.

Moving from galactic scale to our solar system, it has been observed that neutrinos from the sun change flavour on their journey to Earth, implying that they have mass in rank contradiction of the Standard Model. Neutrino masses can be incorporated into extensions of the Standard Model in several ways, but the data is currently not good enough to constrain the possibilities (for example, the data is so-far consistent with neutrinos being either Dirac or Majorana particles).

In addition to the Standard Model being inconsistent with observations, there are aesthetic problems that may also hint that it is not even *self*-consistent. If the Standard Model is interpreted as an effective theory, valid up to some high cutoff energy scale, then there is a “hierarchy problem” due to the Higgs boson. This becomes manifest when calculating the physical Higgs mass. One must tune the bare mass of the Higgs to incredible precision to cancel the huge one-loop correction corrections. Without this “fine tuning”, the Higgs mass would naturally be around the scale of the new physics, which must be as least as high as 1 TeV to evade our experimental searches so far.

Another fine-tuning problem in the Standard Model, this time involving the strong interactions, is the “strong CP problem”. This is the mystery of why a particular CP-violating term in the QCD sector, completely compatible with the SM gauge symmetries,

must nevertheless be very close to zero in order to be consistent with experimental measurements.

Finally, there is the “flavour problem”: the problem of explaining the pattern of fermion masses and mixing angles in the Standard Model.

All of these problems (and more) have spurred generations of physicists to look beyond the Standard Model for new physics. In this thesis I study three so-called “beyond-the-Standard Model” (BSM) theories. The first is Minimal Universal Extra Dimensions (MUED), which postulates the existence of a compactified extra dimension of space. The motivation for studying such extra dimensional theories comes from attempts to quantise gravity and, in particular, string theory. MUED also has a good candidate particle to solve the problem of Dark Matter.

The second theory considered here is called the 4D composite Higgs model (4DCHM). This theory is one of a class of “composite Higgs” models that were devised to solve the hierarchy problem (explained in more detail in Section 5.1). Composite Higgs models do this by imagining that the Higgs boson of the Standard Model is a composite particle, made up new types of strongly interacting fermions. Moreover, the composite Higgs is light because it is a Goldstone boson of a spontaneously broken global symmetry.

The third theory (or, rather, class of theories) under study here is “Technicolor”. This class of models was also proposed to facilitate electroweak symmetry breaking (and so give the Standard Model particles masses) whilst avoiding fine tuning. Again, this is accomplished in by assuming the existence of a new sector of strongly interacting fermions (“techniquarks”). However, instead of forming a Higgs field from Goldstone bosons, the strong dynamics of the theory spontaneously break *chiral* symmetry, and the Goldstone bosons from this breaking provide longitudinal modes for the weak gauge bosons, giving them mass. This is all done without a Higgs field, leaving the theory free of fine-tuning.

It is not enough to propose theories: we must put all theories to the test. The work presented here is concerned with testing the three BSM theories described above using measurements of the recently-discovered Higgs boson [14, 15]. In order to survive as viable theories of nature, MUED, 4DCHM and Technicolor must all be able to explain the observation of a scalar particle at around 125 GeV and correctly predict its interactions with other particles. We will see that the Higgs boson measurements can provide powerful constraints on BSM theories.

The outline of this thesis is as follows. The next chapter describes the Standard Model, summarising the important principles involved in its construction and setting notation for the rest of this document. Chapter 3 describes the method by which experimentalists searched for the Higgs boson and how they have sought to characterise its behaviour since its discovery, finishing with a brief discussion of how one might use experimental

Higgs data to test BSM theories. Chapter 4 discusses the theory of MUED in some detail before describing two projects on the subject. In the first, I worked to create an implementation of MUED in the LanHEP and CalcHEP software packages to facilitate rapid and reliable calculations in MUED. The second project was concerned with testing MUED using data from the experimental Higgs searches (prior to the Higgs discovery). In Chapter 5 I introduce the principles of composite Higgs theories. Concentrating on the 4DCHM, I describe the work I did on confronting the model with data about the behaviour of the newly-discovered Higgs boson. In Chapter 6 I motivate the ideas of Technicolor and describe some promising Technicolor models before constraining these models using Higgs measurements. Finally, I discuss my conclusions in Chapter 7.

Chapter 2

The Standard Model

In this chapter I outline the Standard Model and set up notation that will be used throughout this thesis. The Standard Model is a renormalisable quantum field theory built using the principles of gauge symmetry. To fully define a quantum field theory (QFT), one must specify the fields that exist, and their behaviour under Lorentz transformations. Then one must specify the dynamics of the fields: this is done most straightforwardly by giving a Lagrangian density (hereafter referred to simply as a “Lagrangian”). The “action”, which is constructed from the Lagrangian by integrating over all spacetime, can be used to form the “path integral”, which is a generating functional for calculating correlation functions of the fields. These correlation functions can then be used to construct any observables one might want to predict.

Within this QFT framework, to build a particular model is “simply” to write down a Lagrangian. However, the Lagrangian cannot be just any arbitrary function of the fields: most choices will lead to inconsistent quantum field theories. There are two typical symptoms of this inconsistency: nonunitarity and nonrenormalisability. The former means that probabilities calculated from the resulting QFT can be greater than one. The latter also manifests itself as nonsensically-large probabilities but is more subtle: the presence of infinite probabilities is generic, even in consistent QFTs. Typically one writes the functional form of the Lagrangian as a sum of simple functions (often products) of the fields with free parameters in front of each term. The infinite probabilities can be rendered finite by tuning the parameters carefully, such that certain predictions coincide with their measured values. In renormalisable QFTs, one only needs to tune a finite number of parameters to fit a finite number of measurements and then the entire theory is infinity-free. In nonrenormalisable theories, however, one must tune an infinite number of free parameters to remove every infinity and so the theory loses predictivity. Having said this, nonrenormalisability is not necessarily a problem if one takes the theory to be an effective theory, valid only up to some cutoff energy scale. In this case, as long as one performs calculations concerning energies well below the cutoff, the theory remains *mostly* predictive, up to some energy-dependent uncertainty.

When building a consistent QFT, it is therefore important to choose the Lagrangian carefully. One of the methods that has historically been very successful in ensuring well-behaved quantum behaviour is to require the Lagrangian to obey symmetries under the shuffling of the fields between each other in some well-prescribed manner. In particular, requiring the Lagrangian to be symmetric under groups of transformations that alter the fields differently at each point in spacetime (so-called “gauge” symmetries) frequently guarantees good quantum behaviour and also provides constraints on the allowed interactions between matter and the force fields which match observations very well. The modern approach to Lagrangian building is then to start by hypothesising a symmetry group of gauge transformations. Then, fields representing matter are postulated. Matter particles, by definition, obey Fermi-Dirac statistics so, by the spin-statistics theorem, the fields responsible for these particles must have half-integer spins. Then a choice is made about what representation of the gauge group the matter fields must transform under. The Lagrangian is then formed by writing a polynomial of the fields and their derivatives which is globally invariant under the symmetry group of the theory. The Lagrangian must have a mass dimension of 4 in order to integrate to a dimensionless action (I work throughout this thesis in Planck units where Planck’s constant \hbar and the speed of light c are equal to 1). Any monomial of fields in the Lagrangian with mass dimension different from 4 must therefore have dimensionful coefficients (“couplings”). To ensure the theory is renormalisable, one then rejects terms with couplings of negative mass dimension.

The Lagrangian at this stage is globally symmetric, but terms involving derivatives spoil the local “gauge” invariance. This is remedied by introducing a vector field that transforms in the adjoint representation of the gauge group and promoting all derivatives to “gauge covariant” derivatives, i.e.

$$\partial_\mu \mapsto \partial_\mu + igA_\mu, \quad (2.1)$$

where g is a free parameter that is related to the strength of the coupling between the gauge field and any matter fields present. The gauge field takes values in the Lie algebra of the gauge group and can be written as a superposition of the generators t^i of the group such that

$$A_\mu = A_\mu^i t^i. \quad (2.2)$$

Both A_μ^i and A_μ will be referred to as gauge fields throughout this thesis.

2.1 The SM gauge symmetry and matter content

Following the prescription above, the Standard Model can be fully described by stating that it obeys an $SU(3)_c \times SU(2)_W \times U(1)_Y$ gauge symmetry. The subscript c denotes the conserved QCD colour charge and $SU(2)_W \times U(1)_Y$ is the symmetry group governing the

Field	Lorentz	SU(3) _c	SU(2) _W	U(1) _Y
$Q_L = \begin{pmatrix} u_L \\ d_L \end{pmatrix}$	$(\frac{1}{2}, \mathbf{0})$	3	2	$\frac{1}{3}$
u_R	$(\mathbf{0}, \frac{1}{2})$	3	1	$\frac{4}{3}$
d_R	$(\mathbf{0}, \frac{1}{2})$	3	1	$-\frac{2}{3}$
$L_L = \begin{pmatrix} \nu_L \\ e_L \end{pmatrix}$	$(\frac{1}{2}, \mathbf{0})$	1	2	-1
e_R	$(\mathbf{0}, \frac{1}{2})$	1	1	-2

Table 2.1: Matter content of one of the three generations of the Standard Model fermions

weak and electromagnetic interactions. Next, matter fields are postulated, and chosen to be left- or right-handed Weyl spinors (i.e. to transform respectively under the $(\frac{1}{2}, \mathbf{0})$ or $(\mathbf{0}, \frac{1}{2})$ representations of the Lorentz group, $SO(1,3)$). These choices, or “charge assignments”, are shown in Table 2.1. Fields in the fundamental of $SU(2)_W$ are written as doublets, showing the weak isospin $T_3 = \pm\frac{1}{2}$ components explicitly. The hypercharge has been assigned so that the electric charge of the particle is given in multiples of the charge of the proton, e , by the formula

$$Q = T_3 + Y/2, \quad (2.3)$$

where T_3 is the third component of weak isospin (i.e. the eigenvalue of the third generator of the $SU(2)_W$ group). This relation between electric charge and weak hypercharge is related to electroweak symmetry breaking (EWSB): the above combination of $SU(2)_W$ and $U(1)_Y$ generators is the only one that remains unbroken after EWSB and so is identified with the conserved electric charge. In fact, the hypercharge assignments are completely specified up to an overall normalisation by requiring that all gauge and gravity anomalies to cancel.

Continuing with the renormalisable gauge theory prescription, one should now write down the most general Lorentz and $SU(3)_c \times SU(2)_W \times U(1)_Y$ invariant Lagrangian that can be formed from local products of the matter fields and their derivatives (“local” meaning that the fields and derivatives are all evaluated at the same spacetime point) with couplings that have mass dimension less than or equal to zero.

Finally, the $SU(3)_c \times SU(2)_W \times U(1)_Y$ symmetry should be promoted to a local symmetry by introducing gauge fields G_μ , W_μ and B_μ , each transforming under the adjoint representation of each of the respective $SU(3)_c$, $SU(2)_W$ and $U(1)_Y$ factors of the SM gauge group. All derivatives should be promoted to gauge covariant derivatives of the form

$$D_\mu = \partial_\mu - ig_s G_\mu - ig W_\mu - ig' B_\mu, \quad (2.4)$$

where the gauge fields are Lie algebra-valued fields. The action of the fields when acting on fermions in the fundamental representation of $SU(3)_c$ and $SU(2)_W$, and in the hypercharge Y representation of $U(1)_Y$, is given by

$$G_\mu = G_\mu^a \frac{\lambda^a}{2} \quad (2.5)$$

$$W_\mu = W_\mu^a \frac{\tau^a}{2} \quad (2.6)$$

$$B_\mu = B_\mu^Y \mathbb{I} \quad (2.7)$$

where λ^a and τ^a are the well-known Gell-Mann and Pauli matrices respectively, and \mathbb{I} is the identity matrix. Quantities without generator indices should be understood as being Lie algebra-valued, whereas fields with generator indices are number-valued.

Interpreting the gauge fields as dynamical quantum fields requires us to introduce gauge invariant kinetic terms for each of them. Considering a general gauge field $A_\mu = A_\mu^a t^a$, we form a field strength tensor

$$F_{\mu\nu} = \frac{i}{g} [D_\mu, D_\nu] = \partial_\mu A_\nu - \partial_\nu A_\mu - ig[A_\mu, A_\nu] \quad (2.8)$$

and the kinetic term is the gauge-invariant combination $-\frac{1}{2} \text{tr}(F_{\mu\nu} F^{\mu\nu})$. Writing the field strength as linear combinations of the group generators $F_{\mu\nu} = F_{\mu\nu}^a t^a$, we can say that

$$F_{\mu\nu}^a = \partial_\mu A_\nu^a - \partial_\nu A_\mu^a + gf^{abc} A_\mu^b A_\nu^c, \quad (2.9)$$

where the structure constants of the group f^{abc} are defined by $[t^a, t^b] = if^{abc} t^c$. Using the relation $\text{tr}(t^a t^b) = \frac{\delta^{ab}}{2}$ in any matrix representation of the group, we can write the field's kinetic term as

$$-\frac{1}{2} \text{tr}(F_{\mu\nu} F^{\mu\nu}) = -\frac{1}{4} F_{\mu\nu}^a F_a^{\mu\nu}. \quad (2.10)$$

At this stage, the Lagrangian is then

$$\begin{aligned} \mathcal{L}_{\text{no EWSB}} = & -\frac{1}{4} G_{\mu\nu}^a G_a^{\mu\nu} - \frac{1}{4} W_{\mu\nu}^a W_b^{\mu\nu} - \frac{1}{4} B^{\mu\nu} B_{\mu\nu} \\ & + iQ_L^\dagger \bar{\sigma}^\mu D_\mu Q_L + iL_L^\dagger \bar{\sigma}^\mu D_\mu L_L + iu_R^\dagger \sigma^\mu D_\mu u_R + id_R^\dagger \sigma^\mu D_\mu d_R + ie_R^\dagger \sigma^\mu D_\mu e_R. \end{aligned} \quad (2.11)$$

Here, the fermions are still being treated as two-component spinors. The daggers represent matrix Hermitian conjugation and the sigma matrices are generalisations of the Pauli matrices σ^i , defined by

$$\sigma^\mu = (1, \sigma^1, \sigma^2, \sigma^3); \quad \bar{\sigma}^\mu = (1, -\sigma^1, -\sigma^2, -\sigma^3). \quad (2.12)$$

Note that the covariant derivatives act differently, depending on the representation under which the succeeding fermion field transforms.

So far, it is not clear how this Lagrangian can possibly describe nature. The first step is to notice that the left- and right-handed fermion fields can be interpreted as the left and right components of four-component Dirac fields. Seen in this way, Equation 2.11 is a theory of two quarks (an “up” quark u and “down” quark d) and two leptons (the electron e and the purely left-handed neutrino ν). For example, the Weyl fields u_L and u_R can be grouped into a single Dirac fermion, written in the Weyl basis as $u = \begin{pmatrix} u_L \\ u_R \end{pmatrix}$.

If we define the gamma matrices in this basis to be

$$\gamma^\mu = \begin{pmatrix} 0 & \sigma^\mu \\ \bar{\sigma}^\mu & 0 \end{pmatrix}, \quad \gamma^5 = \begin{pmatrix} -1 & 0 \\ 0 & 1 \end{pmatrix}, \quad (2.13)$$

with the left and right projection operators being given by

$$P_{L,R} = \frac{1 \mp \gamma^5}{2}, \quad (2.14)$$

we can write $u_{L,R} = P_{L,R}u$,¹ and similarly for the other fermions. Using this notation, Equation 2.11 can be written as

$$\begin{aligned} \mathcal{L}_{\text{no EWSB}} = & -\frac{1}{4}G_{\mu\nu}^a G_a^{\mu\nu} - \frac{1}{4}W_{\mu\nu}^a W_b^{\mu\nu} - \frac{1}{4}B^{\mu\nu} B_{\mu\nu} \\ & + i\bar{Q}_L \gamma^\mu D_\mu Q_L + i\bar{L}_L \gamma^\mu D_\mu L_L + i\bar{u}_R \gamma^\mu D_\mu u_R + i\bar{d}_R \gamma^\mu D_\mu d_R + i\bar{e}_R \gamma^\mu D_\mu e_R. \end{aligned} \quad (2.15)$$

The quarks u and d interact by virtue of their $SU(3)_c$ colour charge via eight types of gluon G_μ^a . Both the leptons (e and ν) and the quarks interact via the four vector bosons W_μ^i and B_μ .

The most obvious deficiency of this theory is that it does not contain charm, strange, top and bottom quarks, nor mu- or tau-type leptons. However, these can easily be accommodated by adding two further copies (known as “generations”) of the fermion content and we will assume that the fermions possess an implicit generation index for the rest of this chapter.

A trickier problem is that the particles described by Equation 2.15 are *massless*. (Adding any mass terms would break the gauge symmetry.) This is not a problem for the gluons: they mediate the strong force which is believed to exhibit “colour confinement” at low energies. This means that objects (such as quarks) with colour charge must be bound irrevocably into colour-neutral objects (“hadrons”). Because $SU(3)_c$ is non-Abelian, gluons themselves have colour charge and so are also trapped in hadrons: the strong force is therefore only significant at distance scales of around 10^{-15} m.

¹This is an (albeit common) abuse of notation. To be precise, $P_L u = \frac{(1-\gamma^5)}{2} \begin{pmatrix} u_L \\ u_R \end{pmatrix} = \begin{pmatrix} u_L \\ 0 \end{pmatrix}$

Turning to the “electroweak” bosons W_μ^i and B_μ , we expect one linear combination of these to correspond to the massless photon A_μ . But this leaves three more massless bosons that we do not observe in reality. The fermions are also all massless, in contradiction to observations. Adding Dirac mass terms, mixing the left- and right-handed fermions, would be consistent with the $SU(3)_c$ symmetry. Indeed, a theory of massive quarks interacting via massless (yet confined) gluons, Quantum Chromodynamics (QCD), is completely consistent. It is the “electroweak” symmetry $SU(2)_W \times U(1)_Y$ that is incompatible with fermion masses and so we concentrate on this sector of the Lagrangian for the remainder of this chapter.

To re-write (2.11) in a more physically-transparent form, let us first define the following linear combinations of the electroweak bosons:

$$W_\mu^\pm \equiv \frac{1}{\sqrt{2}}(W_\mu^1 \mp W_\mu^2) \quad (2.16)$$

$$Z_\mu \equiv \cos \theta_W W_\mu^3 - \sin \theta_W B_\mu \quad (2.17)$$

$$A_\mu \equiv \sin \theta_W W_\mu^3 + \cos \theta_W B_\mu. \quad (2.18)$$

The “Weinberg angle” θ_W is left unspecified at the moment. The electroweak Lagrangian can be written as

$$\begin{aligned} \mathcal{L}_{EW} = & i\bar{u}\not{\partial}u + i\bar{d}\not{\partial}d + i\bar{e}\not{\partial}e + i\bar{\nu}_e\not{\partial}\nu_e \\ & + g(W_\mu^+ J_{W^+}^\mu + W_\mu^- J_{W^-}^\mu) \\ & + gZ_\mu J_Z^\mu \\ & + eA_\mu J_A^\mu \end{aligned} \quad (2.19)$$

where the charged currents are given by

$$\begin{aligned} J_{W^+}^\mu &= \frac{1}{\sqrt{2}}(\bar{u}\gamma^\mu P_L d + \bar{\nu}\gamma^\mu P_L e) \\ J_{W^-}^\mu &= \frac{1}{\sqrt{2}}(\bar{d}\gamma^\mu P_L u + \bar{e}\gamma^\mu P_L \nu), \end{aligned} \quad (2.20)$$

the neutral currents by

$$\begin{aligned} J_Z^\mu = & \frac{1}{\cos \theta_W} \left\{ \bar{u}\gamma^\mu \left[\left(\frac{1}{2} - \frac{2}{3} \sin^2 \theta_W \right) P_L + \left(-\frac{2}{3} \sin^2 \theta_W \right) P_R \right] u \right. \\ & + \bar{d}\gamma^\mu \left[\left(-\frac{1}{2} + \frac{1}{3} \sin^2 \theta_W \right) P_L + \left(\frac{1}{3} \sin^2 \theta_W \right) P_R \right] d \\ & + \bar{e}\gamma^\mu \left[\left(-\frac{1}{2} + \sin^2 \theta_W \right) P_L + \sin^2 \theta_W P_R \right] e \\ & \left. + \bar{\nu}\gamma^\mu \left(\frac{1}{2} \right) P_L \nu \right\}, \end{aligned} \quad (2.21)$$

and the electromagnetic currents by

$$J_A^\mu = \bar{u}\gamma^\mu \left(\frac{2}{3}\right) u + \bar{d}\left(-\frac{1}{3}\right) d + \bar{e}\gamma^\mu(-1)e. \quad (2.22)$$

2.2 Electroweak symmetry breaking and the Higgs boson

So far, all particles in the SM Lagrangian Equation 2.15 are massless: bosonic or fermionic mass terms would break the gauge symmetry of the theory and so are forbidden. More precisely, it is the electroweak $SU(2)_W \times U(1)_Y$ symmetry that is broken by mass terms (fermionic mass terms do not break $SU(3)_c$, and the gluons are expected to be massless anyway). Some mechanism of *electroweak symmetry breaking* (EWSB) is therefore required.

In the SM, EWSB is accomplished through the Higgs mechanism. A scalar field ϕ (the “Higgs field”) is introduced into the theory. It is defined to be a singlet of $SU(3)_c$, a doublet of $SU(2)_W$ and to have a weak hypercharge of 1. Gauge symmetry and renormalisability restrict the form of the pure-Higgs and gauge-Higgs contributions to the SM Lagrangian to be

$$\mathcal{L}_{\text{Higgs}} = (D^\mu \phi)^\dagger (D_\mu \phi) + \mu^2 |\phi|^2 - \lambda |\phi|^4, \quad (2.23)$$

where D^μ is the gauge covariant derivative in the appropriate representation. Looking at the “Higgs potential” (the negative of the quadratic and quartic terms not involving derivatives) and reasoning semi-classically, one can see that the lowest energy configurations are not necessarily those in which ϕ is zero everywhere. If the sign of μ^2 and λ are chosen to be positive, the minimum energy (vacuum) configurations have $|\phi| = v/\sqrt{2}$,² where $v \equiv \mu/\sqrt{\lambda}$. From the quantum point of view, the modulus of the field has a “vacuum expectation value” (vev) of $v/2$. One is free to choose the vev to point in any direction in weak isospin space, and then the field is written as perturbations around this vacuum. The most convenient choice of vacuum alignment is $\phi = \frac{1}{\sqrt{2}} \begin{pmatrix} 0 \\ v \end{pmatrix}$. Configurations that are a small perturbation away from this vacuum can then be written as

$$\phi = \frac{1}{\sqrt{2}} \begin{pmatrix} \chi^1 + i\chi^2 \\ v + H + i\chi^0 \end{pmatrix} = \begin{pmatrix} \chi^+ \\ \frac{1}{\sqrt{2}}(v + H + i\chi^0) \end{pmatrix}. \quad (2.24)$$

The vev breaks most of the EW symmetry, leaving behind a residual $U(1)_{\text{EM}}$ symmetry that we identify as the gauge symmetry for electromagnetism. This $U(1)_{\text{EM}}$ is generated by the linear combination of EW generators $Q = T^3 + Y/2$. Varying χ^+ and χ^0 moves between field configurations that can be related by transformations involving the broken EW generators and so correspond to unphysical “Goldstone bosons”. We can picture

²The factor of $\sqrt{2}$ is to match a common convention.

the configuration space of the Higgs field as being partitioned into equivalence classes (called “gauge orbits”) of configurations that are related by EW gauge transformations. We are then free to choose a representative from each gauge orbit where χ^+ and χ^0 are zero: this choice is called the “unitary gauge”.

We can proceed for now in the unitary gauge,³ parameterise the Higgs field as

$$\phi = \frac{1}{\sqrt{2}} \begin{pmatrix} 0 \\ v + H \end{pmatrix} \quad (2.25)$$

and substitute this expression into the Higgs Lagrangian. The first term in (2.23) becomes

$$(D^\mu \phi)^\dagger (D_\mu \phi) \stackrel{\text{unitary}}{\underset{\text{gauge}}{=}} \frac{1}{2} \partial^\mu H \partial_\mu H \left(m_W^2 W^+ W^- + \frac{1}{2} m_Z^2 Z^2 \right) \left(1 + 2 \frac{H}{v} + \frac{H^2}{v^2} \right), \quad (2.26)$$

giving us a kinetic term for the physical Higgs boson H , mass terms for the weak bosons W^\pm (2.16) and Z (2.17) and interaction terms between the weak bosons and the Higgs boson. The masses of the weak bosons are

$$m_W = gv/2 \quad (2.27)$$

$$m_Z = \left(\sqrt{g^2 + g'^2} \right) v/2 \quad (2.28)$$

and the mass of the photon $m_A = 0$, as expected. The Weinberg angle comes out to be

$$\tan \theta_W = g'/g. \quad (2.29)$$

For future reference, Fermi’s coupling constant G_F for beta decay ultimately derives from the W mass (the W boson mediates beta decay) and takes the value

$$G_F = \frac{1}{\sqrt{2}v^2} \approx 1.17 \times 10^{-5} \text{ GeV}^{-2}. \quad (2.30)$$

For completeness, the Higgs potential gives a mass term and quartic self-interaction for the Higgs boson as follows

$$\mu^2 |\phi|^2 - \lambda |\phi|^4 \stackrel{\text{unitary}}{\underset{\text{gauge}}{=}} -\frac{1}{2} m_H^2 H^2 - \frac{m_H^2}{v} H^3 + \frac{m_H^2}{2v^2} H^4 + \text{const.} \quad (2.31)$$

where the constant term is a contribution to the vacuum energy and the Higgs mass is given by

$$m_H = \sqrt{2\lambda}v = \sqrt{2}\mu. \quad (2.32)$$

³Fixing the gauge like this is problematic when quantising the theory: this is discussed in Section 2.4.

2.3 Incorporating fermion masses

In addition to the terms in Equation 2.23, one can add ‘‘Yukawa terms’’ coupling the Higgs field to the fermions. The renormalisable, gauge-invariant terms are given by

$$\mathcal{L}_{\text{Yuk}} = -y_d \bar{Q}_L \phi d_R - y_u \bar{Q}_L \tilde{\phi} u_R - y_e \bar{L}_L \phi e_R + \text{h.c.}, \quad (2.33)$$

where $\tilde{\phi} = -i\sigma^2 \phi$. Substituting in Equation 2.25 yields

$$\mathcal{L}_{\text{Yuk}} = -m_u \bar{u}u - m_d \bar{d}d - m_e \bar{e}e - \frac{m_u}{v} \bar{u}uH - \frac{m_d}{v} \bar{d}dH - \frac{m_e}{v} \bar{e}eH, \quad (2.34)$$

where the fermion masses are given in terms of the Yukawa couplings by $m_\psi = \frac{y_\psi v}{\sqrt{2}}$. In the above I have suppressed the fermion generation index. With this restored, we can see that the Yukawa couplings in Equation 2.33 are, in fact, matrices. In general, these can have arbitrary complex entries, leading to a quadratic mixing of the fermion generations: this means that the fermion fields are not good mass eigenstates. There is freedom, however, to redefine the fields so that the fermion mass matrices are rendered diagonal. The Yukawa (and hence mass) matrices are not in general normal, so they cannot necessarily be diagonalised by a unitary similarity transformation. But, according to the singular value decomposition theorem [17], any matrix M can be written in the form $M = U^\dagger D V$, where D is diagonal and U and V are unitary. This means that if we can perform an independent change of basis on each of the fields u_L , u_R , d_L , d_R , e_L and e_R such that the mass matrices m_u , m_d and m_L are diagonal. If the ν_L field is transformed by the same similarity transformation as e_L , then the lepton sector of the SM Lagrangian does not change form. The quarks are not so simple, however. One has to rotate u_L and d_L independently to diagonalise both quark mass matrices, which means the terms involving Q_L in odd powers, namely the charged current interactions, *will* change form. If U_{u_L} and U_{d_L} are the similarity transformations acting on u_L and d_L , then the charged currents in Equation 2.20 become

$$\begin{aligned} J_{W^+}^\mu &= \frac{1}{\sqrt{2}} (\bar{u} \gamma^\mu V_{\text{CKM}} P_L d + \bar{\nu} \gamma^\mu P_L e) \\ J_{W^-}^\mu &= \frac{1}{\sqrt{2}} (d \gamma^\mu V_{\text{CKM}}^\dagger P_L u + \bar{e} \gamma^\mu P_L \nu), \end{aligned} \quad (2.35)$$

where the ‘‘Cabibbo-Kobayashi-Maskawa’’ (CKM) matrix is given by $V_{\text{CKM}} = U_{u_L}^\dagger U_{d_L}$.

2.4 Gauge fixing, Goldstones and Ghosts

At the classical level, we now have a complete Lagrangian $\mathcal{L}_{\text{SM}} = \mathcal{L}_{\text{no ESWS}} + \mathcal{L}_{\text{Higgs}} + \mathcal{L}_{\text{Yuk}}$ describing massive quarks and leptons interacting via massless gluons, massive

weak vector bosons, and the photon, and also the Higgs boson, H that couples directly to all particles with mass.

When one tries to use this Lagrangian in quantum calculations, the question of how to interpret the gauge symmetry arises. In the previous section we worked in the unitary gauge where the Goldstone bosons vanished. In a general gauge there are many more Lagrangian terms involving the Goldstones. Particularly problematic are the terms

$$(\mathcal{D}^\mu \phi)^\dagger (\mathcal{D}_\mu \phi) \supset im_W (W_\mu^- \partial^\mu \chi^+ - W_\mu^+ \partial^\mu \chi^-) - m_Z Z_\mu \partial^\mu \chi^0, \quad (2.36)$$

containing derivative couplings of a single Goldstone to a single gauge boson. We will see that these derivative couplings, and the problem of gauge fixing, are solved through a procedure called the Faddeev-Popov method.

In a classical theory, the gauge symmetry is seen as a redundancy in the coordinates we have used to describe the true degrees of freedom of the system. This is in analogy to classical electrodynamics, where different choices of the vector potential A_μ can correspond to the same physical state: transformations between equivalent configurations are called gauge transformations. This redundancy causes problems when forming the path integral. Considering, for the moment, a theory involving just a U(1) gauge field A governed by a gauge invariant action $S[A] = \int d^4x \mathcal{L}(A(x))$, if one naively writes the path integral as

$$Z = \int \mathcal{D}A e^{iS[A]}, \quad (2.37)$$

the result is badly divergent due to integrating over an infinite number of physically-equivalent field configurations. One also finds a problem when calculating the free propagator: the kinetic operator is singular so its Green's function is undefined.

Instead, one should “fix the gauge”, picking a single representative configuration \bar{A} from each gauge orbit, and integrating over those physical configurations using a delta functional, i.e.

$$Z = \int \mathcal{D}\bar{A} e^{iS} = \int \mathcal{D}A \delta[A - \bar{A}] e^{iS}. \quad (2.38)$$

Using the “Faddeev-Popov” method, one can remove the delta function. First, the gauge fixing condition can be written using a functional $F[A]$, defined so that $F[\bar{A}] = 0$. One then needs to rewrite the delta function using this condition, remembering to normalise it correctly, i.e. $\delta(A - \bar{A}) = \det(M) \delta[F[A]]$, where $\det M$ is the functional determinant of the “matrix” with components

$$M_{x,y} = \frac{\delta F[A(x)]}{\delta \alpha(y)}, \quad (2.39)$$

and $\alpha(x)$ is the gauge transformation parameter. We could equally-well have chosen another gauge-fixing functional $F[A(x)] - \omega(x)$ without changing the expression (including

the determinant) above. Since Z is gauge- (and therefore ω -) independent, we can multiply our expression by a gaussian functional of $\omega(x)$ and functionally integrate over ω to give

$$\int \mathcal{D}\omega e^{-\int d^4x \frac{i\omega^2}{2\xi}} Z = \int \mathcal{D}A \mathcal{D}\omega \det(M) \delta[F - \omega] e^{iS} e^{-i \int d^4x \frac{\omega^2}{2\xi}} \quad (2.40)$$

$$Z = N \int \mathcal{D}A \det(M) \exp \left[-i \int d^4x (\mathcal{L} + \mathcal{L}_{\text{GF}}) \right] \quad (2.41)$$

where the Gauge fixing Lagrangian $\mathcal{L}_{\text{GF}} = -\frac{1}{2\xi} F^2$ is the result of integrating the complex Gaussian over ω . Finally, we can write the functional determinant in terms of a functional integral over Grassmann-valued fields (which nevertheless have bosonic statistics: particles of such fields would violate the spin-statistics theorem and therefore cannot appear as physical states), given by

$$\det(M) = \int \mathcal{D}c \mathcal{D}\bar{c} \exp \left[i \int d^4x \mathcal{L}_{\text{FP}} \right]. \quad (2.42)$$

where the ‘‘Faddeev-Popov Lagrangian’’ is $\mathcal{L}_{\text{FP}} = \bar{c}(-M)c$. The path integral is then ultimately

$$Z = N \int \mathcal{D}A \mathcal{D}c \mathcal{D}\bar{c} \exp \left[- \int d^4x (\mathcal{L} + \mathcal{L}_{\text{GF}} + \mathcal{L}_{\text{FP}}) \right]. \quad (2.43)$$

The constant factor N is unimportant because it always cancels in ratios when calculating physical observables and S matrix elements.

If the field A considered above is an Abelian gauge field (so that it transforms as $A_\mu \mapsto A_\mu - \frac{1}{g} \partial_\mu \alpha$, where g is a coupling constant), then a suitable gauge fixing condition is $F[A(x)] = \partial_\mu A^\mu(x)$. When $\omega = 0$, this corresponds to the Lorentz gauge in classical electrodynamics. With this choice, $M_{xy} = -\frac{\partial^2}{g} \delta(x-y)$, $\mathcal{L}_{\text{GF}} = -\frac{1}{2\xi} (\partial_\mu A^\mu)^2$ and $\mathcal{L}_{\text{FP}} = \frac{1}{g} \bar{c} \partial^2 c$.

The integral is now convergent and the extra terms quadratic in A from \mathcal{L}_{GF} render the kinetic operator non-singular, allowing us to derive the free propagator.

When gauge fixing theories involving spontaneous symmetry breaking, such as the electroweak portion of the SM Lagrangian, it is convenient to use a modified version of the Lorentz gauge fixing condition called the R_ξ gauge. That gauge ensures the cancellation of the troublesome quadratic terms, mentioned at the beginning of the previous subsection, that mix gauge and Goldstone bosons. We have four electroweak gauge fields, W^a and B . If we parameterise the Higgs field as in Equation 2.24, the gauge fixing

conditions in the R_ξ gauge are

$$G^1 = \partial^\mu W_\mu^1 - \xi \frac{g^v}{2} \chi^2 \quad (2.44)$$

$$G^2 = \partial^\mu W_\mu^2 - \xi \frac{g^v}{2} \chi^1 \quad (2.45)$$

$$G^3 = \partial^\mu W_\mu^3 + \xi \frac{g^v}{2} \chi^0 \quad (2.46)$$

$$G^Y = \partial^\mu B_\mu - \xi \frac{g^v}{2} \chi^0. \quad (2.47)$$

After writing the gauge fields in their mass eigenstates, the resultant gauge fixing terms are

$$\begin{aligned} \mathcal{L}_{\text{GF}} &= - \sum_{a=1}^3 \frac{(G^a)^2}{2\xi} - \frac{(G^Y)^2}{2\xi} \\ &= -\frac{1}{\xi} |\partial^\mu W_\mu^+ + i\xi m_W \chi^+|^2 - \frac{1}{2\xi} (\partial^\mu Z_\mu - i\xi m_Z \chi^0)^2 - \frac{1}{2\xi} (\partial^\mu A_\mu)^2. \end{aligned} \quad (2.48)$$

These terms contribute an extra term to the gauge bosons' kinetic operators, kinetic terms and ξ -dependent mass terms for the Goldstone bosons, and terms that cancel the gauge-Goldstone couplings from the Higgs Lagrangian (after integrating by parts).

Chapter 3

Discovering and characterising the Higgs boson

The Higgs sector of the SM, described by (2.23) and (2.33), had not been directly probed experimentally until recently, with the discovery of a neutral particle at the Large Hadron Collider (LHC). This discovery was announced by the ATLAS [14] and CMS [15] experimental collaborations on 4th July 2012. Since then, the major research programme of ATLAS and CMS has been to measure the properties of the new particle (hereafter called the Higgs boson, or just the Higgs), such as spin [18, 19, 20] and its couplings to the other SM particles [21, 22]. So far, all data are consistent with the SM Higgs hypothesis but the uncertainty in the measurements are large and we could well discover a deviation from SM as the LHC records more data. For example, regarding the spin of the new particle, spin-2 and pseudoscalar Higgs hypotheses are still both consistent with the data [18, 19, 20], although the SM scalar hypothesis is preferred. In addition, some of the couplings of the new particle to the other SM particles have been measured [21, 22], but the error bars on many of these measurements are huge; indeed, only Higgs couplings to gluons, electroweak bosons, taus, and bottom quarks have so far been measured with any precision at all.

In this chapter I will describe the process experimentalists followed in order to discover and then characterise the Higgs boson. In the first section below I explain some important, simplifying assumptions that are generally made when investigating Higgs phenomenology and in Section 3.2 I discuss the production and decay modes of the SM Higgs within this approximate framework. In Section 3.3 I discuss the main language and techniques used to exclude bad Higgs hypotheses, quantify promising hypothesis and finally classify any resulting discovery, all making use of the central statistical quantity: the likelihood function. This section ignores or glosses over several technical details that complicate understanding on a first pass: these details are elaborated on in Section 3.4. Finally, in Section 3.5, I outline a framework in which BSM models can be compared

with the Higgs data. This framework is used throughout the rest of the thesis to test three classes of BSM theory.

3.1 Preliminaries

Here I outline the framework in which Higgs physics is studied. This summary takes a pre-LHC viewpoint and motivates the search strategy of the ATLAS and CMS collaborations based on the previous searches of the second run of the Large Electron-Positron Collider (LEP2).

The Standard Model Higgs is an unstable particle and so we would expect to observe it as a resonance. When evaluating the cross-section for events that could involve a Higgs as an intermediate state, the interference of Higgs amplitudes with non-Higgs amplitudes is assumed to be negligible. This allows one to talk meaningfully about signal events (those involving the Higgs) and background events (those not involving the Higgs).

Going further, the SM Higgs is predicted to have a narrow width. The exact value of the width depends on the mass of the Higgs m_H , which is a free parameter in the Standard Model. However, assuming the Standard Model is correct, the Higgs (along with other SM particles such as the top quark) will enter into loop-level calculations of quantities such as the Z boson propagator, so precise SM predictions of the Z boson mass will depend on m_H . Precision measurements of the physical Z boson mass and parameters such as the effective weak mixing angle — so-called “electroweak precision tests” (EWPT) — as well as other parameters, including the top quark mass, allow one to estimate the mass of the SM Higgs. Before the LHC, the best-fit value was $m_H = 114_{-45}^{+69}$ GeV with a 95% CL upper bound of $m_H < 260$ GeV (see, for example, [23] for a review). Direct searches for the Higgs provided another constraint: LEP2 placed a lower bound on the Higgs mass of $m_H > 114.4$ GeV at the 95% confidence level (CL) [24].

Within the mass range $114.4 \leq m_H \leq 260$ defined by the 95% CL limits from EWPT data and direct searches, the SM Higgs width is predicted to vary between 3 MeV and 5 GeV [25]. Even at the extreme end of this range, the width is much smaller than the Higgs mass and so it can be taken as narrow. This narrow width approximation (NWA) introduces theoretical uncertainty at the percent level, which could become significant in future precision experiments, for instance at the future International Linear Collider.

Higgs signal events can then be described in two steps: the production of an on-shell Higgs, followed by an on-shell Higgs decay.

3.2 Higgs production and decay

The LHC is a proton-proton collider, so SM Higgs bosons will be produced from the collision of a parton (quark or gluon) from each proton. At tree-level, the SM Higgs couples to SM particles in proportion to their masses. There is therefore no tree-level coupling of two gluons to a Higgs, and the coupling of a valence u or d quark from one proton with a corresponding sea antiquark from the other will be small due to both the small Yukawa coupling and the parton distribution function suppression. In fact, the most significant production process is gluon-gluon fusion (ggF), where the gluons couple to the Higgs at the loop level. The leading-order contribution is from a triangle loop of top quarks. The next most significant production mechanism is vector boson fusion (VBF), where quarks from both protons each radiate a W or Z boson that fuse to form a Higgs boson. This will mean there are two quarks produced in association with the Higgs. There is also Higgs production in association with a weak gauge boson, also known as Higgs-strahlung. Finally, the least significant of the production processes generally studied is production with associated top quarks (ttH). Leading-order Feynman diagrams for each of the above processes, as well as a graph showing the cross-sections of each process as a function of the Higgs mass, are shown in Figure 3.1.

The NWA also simplifies the inclusion of parton distribution functions (PDFs) for the gluon fusion production cross-section (which is the most important of the production processes). In general, the production of a Higgs from a pair of protons colliding with centre-of-mass energy \sqrt{s} via gluon-gluon fusion can be written as

$$\sigma_{\text{ggF}} = \int dx_1 dx_2 f_1(x_1) f_2(x_2) \hat{\sigma}_{\text{ggF}}(\hat{s}), \quad (3.1)$$

where $x_{1,2}$ are the longitudinal momenta carried by each of the two partons as a fraction of the hadronic centre-of-mass energy \sqrt{s} ; $f_{1,2}$ are the gluonic PDFs of the two protons; $\sqrt{\hat{s}} = \sqrt{s x_1 x_2}$ is the centre-of-mass energy of the interacting partons; and $\hat{\sigma}_{\text{ggF}}$ is the partonic cross-section for the process. In the NWA, the partonic cross-section can be written as

$$\hat{\sigma}(\hat{s}) = \bar{\sigma}_{\text{ggF}}(m_H^2) \delta(\hat{s} - m_H^2). \quad (3.2)$$

The model-independent part of the partonic cross-section can then be brought outside the integral involving PDFs given in Equation 3.1, i.e.

$$\sigma_{\text{ggF}} = \bar{\sigma}_{\text{ggF}}(m_H^2) \int dx_1 dx_2 f_1(x_1) f_2(x_2) \delta(\hat{s} - m_H^2). \quad (3.3)$$

If σ_{ggF} denotes the hadronic cross-section for the production of a Higgs boson of mass m_H in an arbitrary model, when forming the ratio with the SM prediction we find that

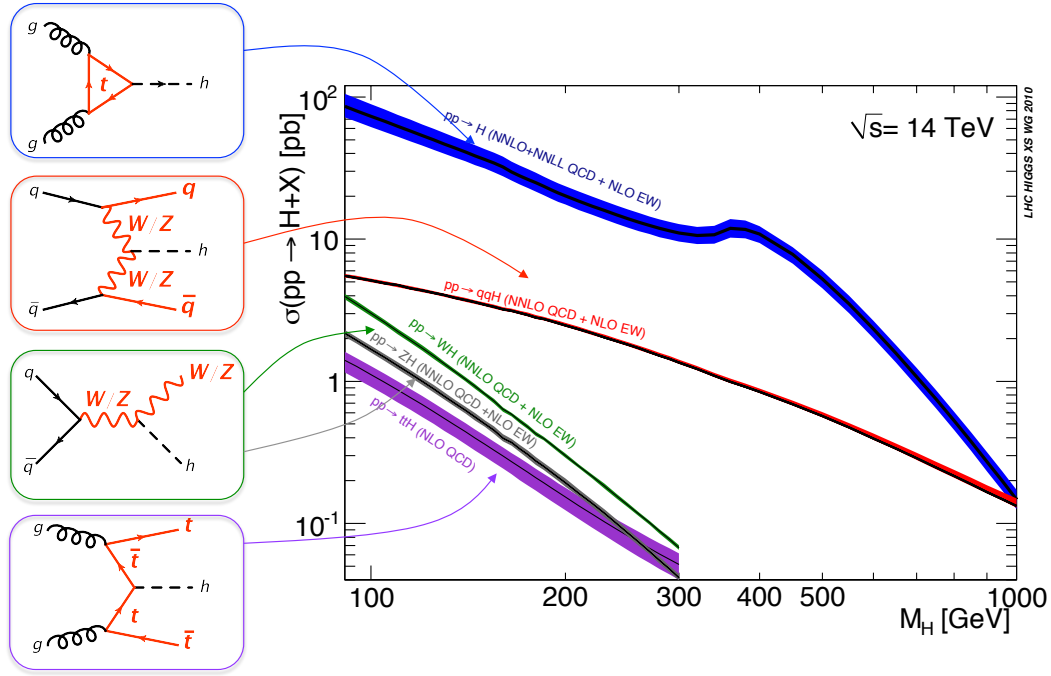


Figure 3.1: The four most important Higgs production processes and their cross-sections as a function of Higgs mass. The cross-sections graph is from Fig. 42 of [25]. The graph is for a centre-of-mass energy of 14 TeV, although changing this within reasonable limits only noticeably affects the overall normalisation.

the (model-independent) PDF integrals cancel in the ratio to give

$$\frac{\sigma_{ggF}}{\sigma_{ggF}^{\text{SM}}} = \frac{\bar{\sigma}_{ggF}}{\bar{\sigma}_{ggF}^{\text{SM}}}. \quad (3.4)$$

It should be noted that this cancellation of PDF dependence does not apply to other production processes that involve associated particles in the final state. However, in this thesis I consider only models where the production cross-sections have SM-like dependence on the partonic momenta and differ only from the SM by a scale factor. Thus, when forming ratios of the cross section (at the hadronic level) of a BSM production process (e.g. vector boson fusion) and the relevant SM value, the answer is simply the scale factor.

Once the SM Higgs has been produced, it will decay into a pair of SM particles. A graph of the main Higgs decay modes is shown in Figure 3.2, together with the total width, both as a function m_H . For example, one can see that for Higgs masses in the region of 125 GeV (where the Higgs was discovered) the decay with the largest branching ratio is to a bottom quark pair ($H \rightarrow b\bar{b}$).

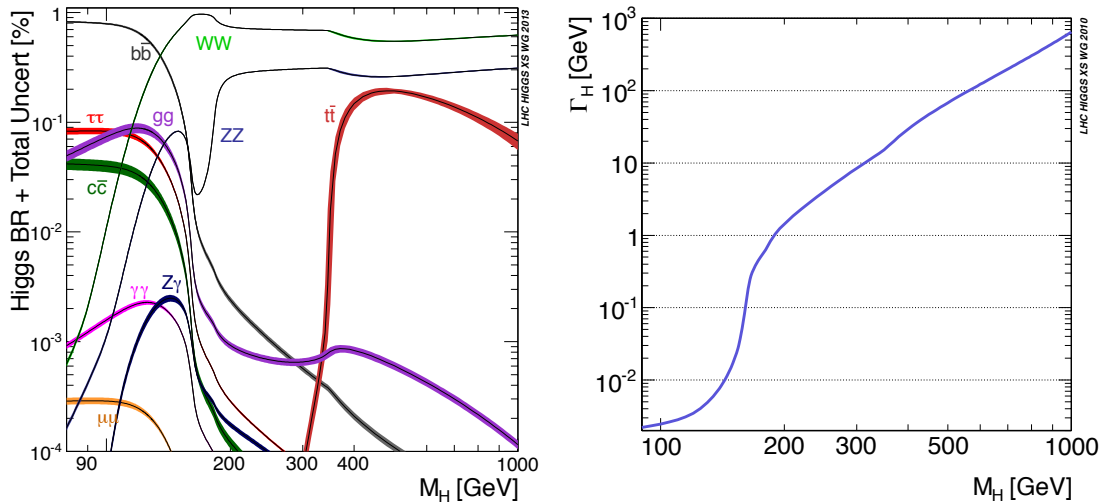


Figure 3.2: Left: the branching ratios of the most important SM Higgs decay modes and their branching ratios as a function of Higgs mass. Right: the total SM Higgs width. Both graphs are from the companion website <https://twiki.cern.ch/twiki/bin/view/LHCPhysics/CrossSections> for [25].

3.3 Exclusion, discovery and characterisation

Within the framework described in the previous section, here I sketch the process the experimental collaborations went through to exclude different Higgs mass hypotheses, quantify the significance of the Higgs discovery and finally investigate the properties of the newly discovered boson. The sections following this summary go into more detail about selected points.

3.3.1 The likelihood function

The Higgs searches performed at the LHC can be classified as either “cut and count” or “shape” analyses. Cut-based experiments pick out (“cut”) particular kinds of events based on the identity and kinematics of the final state particles. These cuts are chosen to reject as many background events whilst accepting as many signal events as possible (i.e. to maximise the signal-to-background ratio). The number of events surviving the cuts are then counted. To test a hypothesis, such as the SM Higgs, one calculates the number of events one would expect to pass the cuts if the model were true, together with the theoretical and experimental uncertainties, and the result is compared to number of observed events. Large deviations (relative to the uncertainties) imply the hypothesis is not a good description of nature.

Shape analyses take into account how the number of observed events are distributed with some kinematical variable or variables. In fact, these analyses can also be seen

as counting experiments: one can separate the events into different bins according to the value of the measured kinematical variables. Then one can count the number of events in each bin and interpret the bins as cut categories.

Due to the statistical nature of quantum field theory, one can only predict from theory the probability of observing a particular number of events. Each proton-proton collision can be seen as an independent Bernoulli trial. The probability p of a collision leading to an event that survives the cut being considered will generally be small. In N collisions, the probability of observing n interesting events is given by a binomial distribution parameterised by N and p . Events passing the cuts are very rare, and we are considering very large numbers of events, so the binomial distribution can be approximated by a Poisson distribution

$$P(n; \nu) = \frac{\nu^n e^{-\nu}}{n!} \quad (3.5)$$

parameterised by $\nu = Np$. This parameter is equal to both the variance and the expected number of events $\bar{n} = \bar{s} + \bar{b}$ (\bar{s} and \bar{b} being the expected number of signal and background events respectively).

So far we have considered a discrete probability distribution, but it is very convenient to work with continuous, analytic functions. If the number of events surviving the cut is large (greater than 10, as a rule of thumb) then the discrete Poisson can be approximated by a continuous Gaussian probability density function

$$\rho(n|\bar{n}) \propto \exp \left[-\frac{(n - \bar{n})^2}{2\bar{n}} \right] \quad (3.6)$$

whose mean equals its variance. The normalisation is typically chosen to give $\int_{-\infty}^{\infty} \rho(n) dn = 1$ or $\int_0^{\infty} \rho(n) dn = 1$ although, if the Gaussian approximation is valid, the difference between these normalisations should be small.

Typically, a model will contain several free parameters which we can write as a vector $\boldsymbol{\mu} = (\mu_1, \mu_2, \dots, \mu_M)$. Similarly, the experiment will make several different measurements $\mathbf{n} = (n_1, n_2, \dots, n_N)$. The model's prediction for the expected values of the N measurements will be a function of the M model parameters, i.e. $\bar{\mathbf{n}}(\boldsymbol{\mu})$. The probability density function for observing \mathbf{n} , given a particular model $\boldsymbol{\mu}$ is simply the product of the individual probability functions for each measurement.

When hypothesis testing, the question one intuitively wants to answer is: “how likely is it that a hypothesis under test is true, given the observed data?” In the classical “frequentist” approach to probability, the question is not well-defined. We can only define probability for the inverse of the question, i.e. “what is the probability that we observe particular data, given that the hypothesis under test is true?” In the Bayesian approach to statistics, the definition of probability is modified to describe *confidence* in a particular hypothesis. The experimental collaborations at the LHC use a mostly-frequentist approach, as set out in [26, 27]. Despite this, it is conventional to use

Bayesian-flavoured language and *define* the “likelihood function” (intuitively measuring the likelihood of a model being correct, given the observed data \mathbf{n}) as

$$\mathcal{L}(\boldsymbol{\mu}|\mathbf{n}) = \rho(\mathbf{n}|\boldsymbol{\mu}) = \prod_{i=1}^N \rho(n_i|\boldsymbol{\mu}) \quad (3.7)$$

and interpret it as a function of the model parameters $\boldsymbol{\mu}$.

3.3.2 Excluding a hypothesis

Throughout the Higgs searches, two hypotheses were considered: the “background only” hypothesis and the “signal plus background” hypothesis.

The background-only hypothesis is simply the Standard Model without the Higgs boson. This isn’t actually a theoretically well-defined model because, without the Higgs, vector boson masses break gauge invariance and cause problems with renormalisation. Also, the theory is not unitary at high energies. But we have seen that (due to negligible signal-to-background interference) it is meaningful to talk about background events and Higgs signal events: the background-only model simply means that the expected number of events is calculated using the full SM, but the signal events are not included in the total, so that $\bar{\mathbf{n}} = \bar{\mathbf{b}}$. In the background-only model, there are no free parameters.

In the SM Higgs (“signal plus background”) model, the full result is kept so that $\bar{\mathbf{n}} = \bar{\mathbf{s}}(m_H) + \bar{\mathbf{b}}(m_H)$. In this model, there is one free parameter: the Higgs mass m_H .

The dependence of the signal on the Higgs mass is clear, but the dependence of the background events on m_H is less obvious. The SM Higgs hypothesis is a “composite” hypothesis in that it can be seen as a family of related “simple” hypotheses: one for each value of the free parameter m_H . Each simple hypothesis can be compared to data separately. The important point to understand here is that the kinematical cuts performed on the data should be *hypothesis*-dependent: they depended on m_H . (They have been specifically designed around the model in order to exclude as much background and keep as much signal as possible.) This is why the number of both signal and background events *after cuts* are functions of m_H .

The procedure for excluding a particular mass hypothesis is as follows. First, the expected number of events (after all cuts) should be calculated in the SM Higgs model for a particular value of m_H . Next, the number of observed events are counted (after the same m_H -dependent cuts). If the number of observed events are less than the number predicted by the hypothesis and, in particular, if the number of events is similar to the number predicted in the background-only hypothesis, then it suggests that the hypothesis is bad. Of course, the downwards fluctuation of \mathbf{n} could be a statistical fluke and the model could still be correct.

In order to objectively exclude the hypothesis, the “unlikeliness” of the downward fluctuation should be quantified, perhaps by calculating the probability of seeing the observed downward fluctuation, given the m_H hypothesis. Actually, this probability will always be small (the probability of observing any particular number of events is tiny) so a more useful question to ask is: “what is the probability of measuring the observed downward fluctuation *or worse*, given the m_H hypothesis?” This probability is called the p -value and can be defined simply for a single measurement as

$$p = \int_0^{n_{\text{obs}}} \mathcal{L}(m_H|n) \, dn, \quad (3.8)$$

where n_{obs} is the actual outcome of the measurement. When the data consist of more than one measurement, the meaning of “*or worse*” in the above question needs to be more carefully defined. It is taken to mean “values of \mathbf{n} which are less likely to be observed than \mathbf{n}_{obs} , given the m_H hypothesis.” With this definition, the p -value becomes

$$p = \int_{\Omega} \mathcal{L}(m_H|\mathbf{n}) \, d^N \mathbf{n}, \quad (3.9)$$

where Ω is the region of the N dimensional space of possible values of \mathbf{n} such that $\mathcal{L}(m_H|\mathbf{n}) < \mathcal{L}(m_H|\mathbf{n}_{\text{obs}})$.

If this p -value is small for a particular hypothesis m_H , given the particular observed data \mathbf{n}_{obs} , then we can exclude the hypothesis. Conventionally, a critical value of $p = 0.05$ is chosen as the exclusion threshold, and one describes a hypothesis with a p -value lower than this as being excluded at the 95% confidence level (CL). (The confidence level is defined as $\text{CL} = 1 - p$.)

The collaborations could have produced graphs of p (or, equivalently, CL) as a function of m_H but, in fact, they chose to display this information differently. To understand their method, it should be noticed that if the observed number of events is similar to the background expectation, a signal model that predicts a large excess events is easier to exclude than a model that predicts a small excess. With this motivation, the signal model can be modified with an extra parameter μ that uniformly enhances the signal cross-sections in all channels. In this new, generalised model, the expected number of events is then $\bar{\mathbf{n}} = \mu \bar{\mathbf{s}}(m_H) + \bar{\mathbf{b}}(m_H)$. One then proceeds as before, calculating the p -value for each choice of the parameters (m_H, μ) . What was plotted by the collaborations was $\mu_{95\%}^{\text{obs}}$. This is the value of μ for which the signal plus background model is excluded by the observed data at exactly the 95% CL. These plots, an example of which is shown in Figure 3.3, became known as “Brazil band” plots because of their green and yellow colour scheme. The solid line shows the $\mu_{95\%}^{\text{obs}}$ defined above.

Before the official Higgs discovery, it was desirable to look at the exclusion plot such as in Figure 3.3 (top) and get an idea of whether the failure to exclude a particular mass value was because there really is no signal, or just because enough data had not yet been

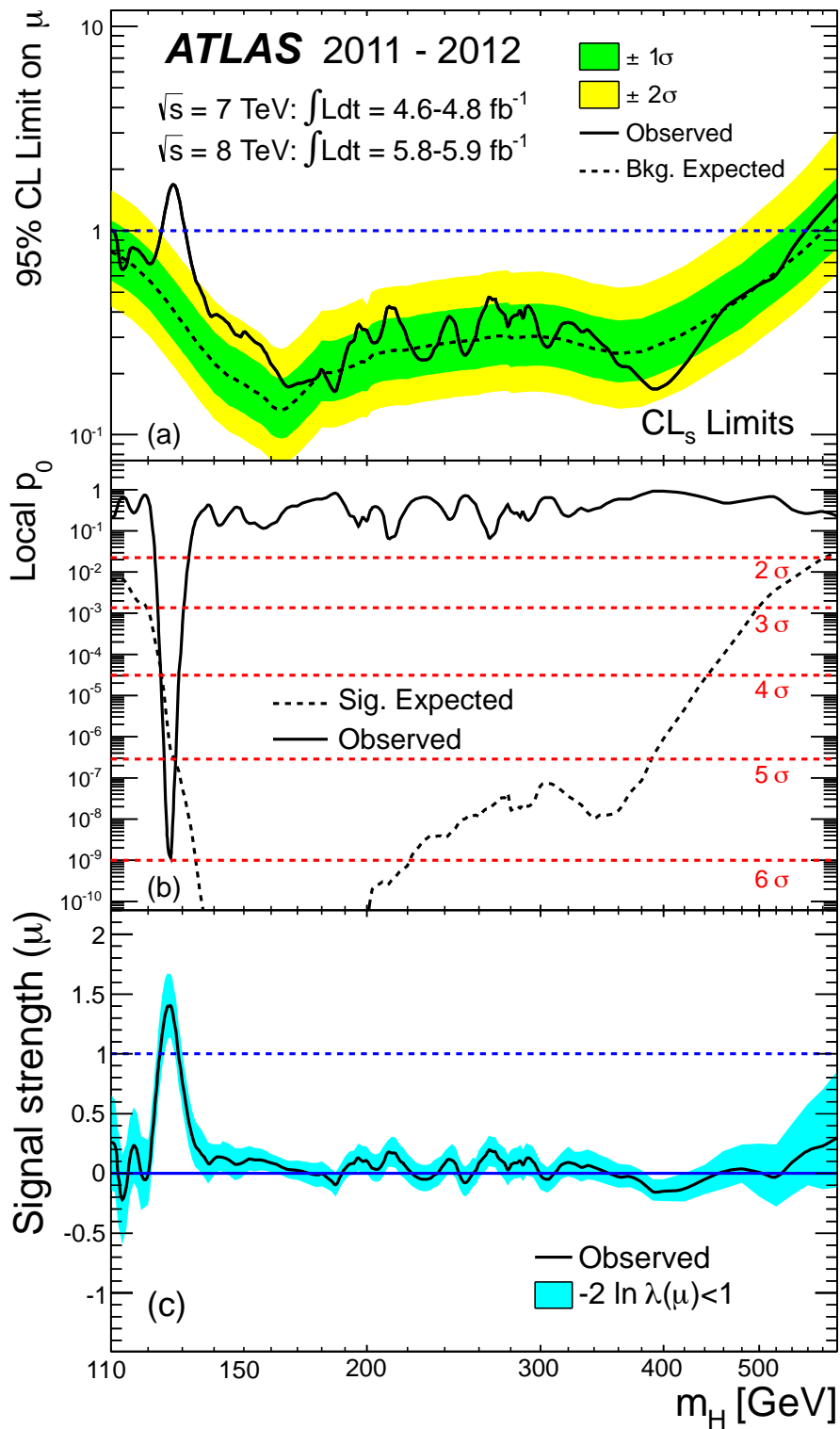


Figure 3.3: Fig. 7 from ATLAS Higgs discovery paper [14] showing the combined “Brazil band” exclusion plot (top), the local p value for the background only hypothesis (middle) and the best-fit value for the global signal strength parameter (bottom), all as a function of Higgs mass m_H .

collected to place strong limits on the hypothesis. This is the purpose of the dashed line and associated bands in the figure. The dashed line shows $\mu_{95\%}^{\text{exp}}$, a quantity that can be calculated before observations are made. It is imagined that the background only hypothesis is correct, and that the number of observed events in each channel is exactly what would be expected under this hypothesis. Then the “signal plus background” hypothesis is then tested as before, but with $\mathbf{n}_{\text{obs}} = \bar{\mathbf{b}}(m_H)$. For each choice of m_H , the value of μ for which $p=0.05$ (i.e. CL = 95%) is defined to be $\mu_{95\%}^{\text{exp}}$. This process is then repeated for values of \mathbf{n}_{obs} that are one and two standard deviations above and below the background expectation in each channel (where the standard deviation in the background-only model in channel i is simply $\sqrt{\bar{b}_i}$). This leads to the green and yellow bands.

If, once the experiment is performed, $\mu_{95\%}^{\text{obs}}$ is larger than $\mu_{95\%}^{\text{exp}}$, this means that there have been more events than would be expected if the background-only hypothesis were true, making it harder to exclude a particular signal hypothesis. If the difference is large (relative to the standard deviation within the background-only hypothesis) then it is unlikely the background “fluctuated up” to the observed data, and so it becomes more plausible that there is actually a signal.

Fluctuations of data *below* the background expectation do not have a plausible explanation except for a statistical fluctuation. The only other possibilities are either that there are signal processes destructively interfering with the background processes (in which case the framework we have been using up to now is invalid) or that our understanding of the background is not as good as we believed. The latter seems particularly unlikely given how much work has gone into understanding background SM processes at the LHC, LEP and the Tevatron.

If the SM Higgs model were true with a Higgs mass of m_H , and if the mass resolution and cuts were perfect and an infinite amount of events were observed, one would eventually expect the solid and dashed lines (and the bands) to be zero everywhere except for at m_H . There, the dashed line and bands would remain zero, but the solid line would take the value 1.

3.3.3 Quantifying a discovery

The $\mu_{95\%}^{\text{obs}}$ prescription provides a reasonably intuitive way of confidently excluding Higgs mass hypotheses when the data is more background- than signal-like. However, when an excess of events above the background expectation begins to be observed for some value of m_H , understanding this excess quantitatively within the above prescription become difficult.

A “discovery” is simply classed as a significant deviation from the background-only expectation. We work again with the pure SM Higgs hypothesis (i.e. $\mu = 1$) and define

the likelihood function for the background-only hypothesis as

$$\mathcal{L}_b(m_H|\mathbf{n}) = \rho(\mathbf{n}|\bar{\mathbf{n}} = \bar{\mathbf{b}}(m_H)). \quad (3.10)$$

This is, confusingly, a function of m_H , despite ostensibly not being anything to do with the signal hypothesis involving the Higgs. In fact, the dependence comes from the m_H -dependent cuts that have been applied. If there is an excess of events \mathbf{n} above the background-only expectation $\bar{\mathbf{b}}$ then this can be quantified by defining the “local p -value” as

$$p_0^{\text{obs}} = \int_{\Omega} \mathcal{L}_B(m_H|\mathbf{n}) d^N \mathbf{n}, \quad (3.11)$$

where the integral is over a region Ω of the N -parameter space of possible \mathbf{n} values where $\mathcal{L}_B(m_H|\mathbf{n}) < \mathcal{L}_B(m_H|\mathbf{n}_{\text{obs}})$.¹ In Figure 3.3, the solid line in the middle plot shows p_0^{obs} .

For *discovery*, we set the critical p -value at the 5σ significance level (for comparison, the 95% CL exclusion limit corresponds to approximately 2σ). To convert from a significance z to a p -value, the relation is

$$p = 1 - \text{erf}(z/\sqrt{2}) \quad (3.12)$$

where the error function is defined to be

$$\text{erf}(x) = \frac{2}{\sqrt{\pi}} \int_0^x e^{-t^2} dt. \quad (3.13)$$

So when the solid line in the middle plot of Figure 3.3 drops below the 5σ line, one can confidently say there is a signal.

The dashed line in local p_0 plot of Figure 3.3 fulfils a similar role to the dashed line in the top plot. In regions where p_0 is high, it allows one to say whether this is due to the model being excluded, or simply just that there have not yet been enough data recorded. It is calculated in the same way as p_0^{obs} , except that we imagine $\bar{\mathbf{s}} + \bar{\mathbf{b}}$ events were observed, instead of the actual \mathbf{n}_{obs} .

The quantity p_0 is termed the “local” p -value because it is the p -value found ignoring the “look-elsewhere” effect. For each value of m_H chosen (which leads to a particular cut) the number of events are counted, and each count can be seen as a separate bin. One would not be surprised to see a large deviation in *one* of the bins studied. A 5σ excess for one choice of m_H is not as significant as unlikely (assuming the background-only hypothesis is true) as it first appears because one must remember that many other m_H values are also being considered and one would expect to see quite large fluctuations *somewhere*. This “look-elsewhere” effect is compensated for using a method described in [27]. However, as data rules out more and more of the Higgs parameter space, a

¹There is a subtlety here around whether one restricts the domain Ω to regions where $\mathbf{n} > \mathbf{n}_{\text{obs}}$ (a so-called “one-tailed” test) or allows \mathbf{n} to take any value (a “two-tailed” test). In reality, the experimental collaborations use a significantly different statistical approach to the one outlined here so that this issue is dealt with in a different way.

narrower and narrower range of m_H is considered when new data is available, leading the look-elsewhere effect to become increasingly less important as more data is collected.

3.3.4 Characterising the excess

ATLAS [14] and CMS [15] jointly announced the official discovery of the Higgs boson (meaning the putative signal exceeded the background to a significance of better than 5σ) on 4th July 2012. The signal was consistent with a resonance caused by a bosonic particle with mass around 125 GeV. This resonance (referred to as “the Higgs” in this thesis, regardless of its ultimate nature) seemed to interact with SM particles in ways consistent with the SM Higgs in all the channels accessible to the experiments. After the discovery, the next step was to measure the properties of the Higgs more precisely to determine whether it really is the SM Higgs, or something from beyond the Standard Model.

First, one can look again at the generalised SM Higgs model which is SM-like except for an overall enhancement in all of the Higgs production cross-sections by a factor of μ . It was described in the previous section how this parameterisation could be used to define $\mu_{95\%}^{\text{obs}}$. One can also vary μ in order to find the best-fit value $\hat{\mu}$, i.e. the value of μ that maximises the combined likelihood $\mathcal{L}(\mu, m_H | \mathbf{n}_{\text{obs}})$. If this is done separately for each choice of m_H , one can produce a plot like the bottom graph in Figure 3.3.

Instead of using all the data, one can restrict oneself to data from a particular channel, such as considering only events with particular particles in the final state. One can then calculate $\hat{\mu}_Y$: the best-fit value of μ for each final state Y . This is an effective measurement of the strength of the couplings of the Higgs boson to particular SM particles, relative to the SM values. Figure 3.4 shows values of $\hat{\mu}_Y$ determined by CMS [22] using data from several different final states Y , along with 1σ uncertainties.

3.4 Log-likelihood ratios, the CL_s method, and all that

The the previous section an intuitive understanding of the procedure for hunting for the Higgs, excluding mass hypotheses, quantifying an observed excess, and finally characterising the discovery. However, it glossed over several details and the actual methods employed by ATLAS and CMS are considerably different. In this section, first I talk about the method of calculating p -values from test statistics rather than from multi-dimensional integrals and introduce the log-likelihood ratio. Next I explain how experimental and theoretical uncertainties (so far neglected) are incorporated into definition of the likelihood function, which leads to the “profiled log likelihood ratio” test statistic.

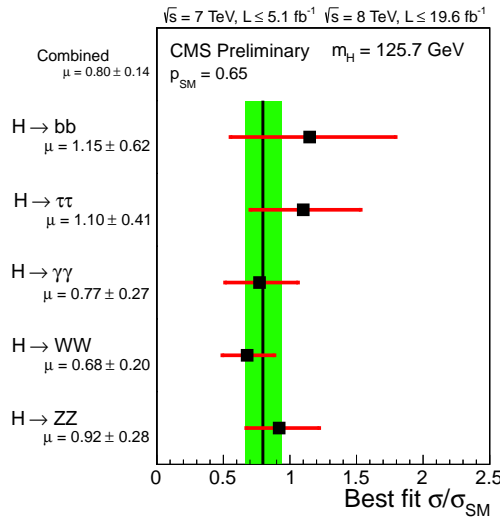


Figure 3.4: Scatter plot from the CMS paper [22] showing the best-fit values (with 1σ uncertainties) of the signal enhancement factor μ when considering various final states separately.

3.4.1 Test statistics and hypothesis testing

The method of hypothesis testing outlined Section 3.3.2, involving the computation of a p -value of some model such as in Equation 3.9, is a form Fisher significance testing. The procedure actually employed by ATLAS and CMS for excluding SM Higgs hypotheses of various masses and also quantifying an observed excess is closer in practical terms to the Neyman-Pearson hypothesis testing. When either distinguishing between two hypotheses (*à la* Neyman-Pearson) or rejecting a single hypothesis at a given significance (*à la* Fisher), one adopts the following general procedure.

1. Identify a null hypothesis H_0 that one wishes to confront with data.
2. Devise an experiment that measures N quantities $\mathbf{n} = (n_1, n_2, \dots, n_N)$ that are predicted to be distributed as independent random variables by H_0 .
3. Set the significance level α (conventionally $\alpha = 0.05$).
4. Choose a region C of the space of outcomes \mathbf{n} such that the outcome is predicted to fall in C with a probability of α , according to H_0 , i.e.

$$\alpha = \int_C \rho(\mathbf{n}|H_0) d^N \mathbf{n}, \quad (3.14)$$

where $\rho(\mathbf{n}|H_0)$ is the probability density function for \mathbf{n} according to H_0 . The complement C^* is sometimes called the acceptance region.

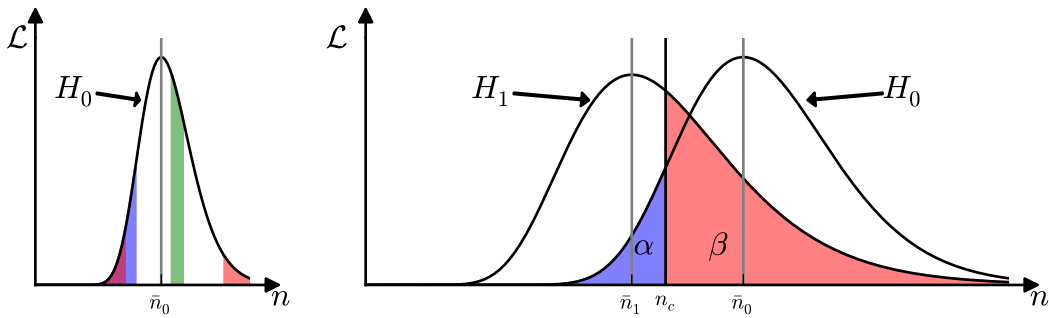


Figure 3.5: Left: possible choices of critical regions of size 5% with red corresponding to a two-tailed test, blue to a one-tailed test, and green to another valid, but useless, choice of critical region. Right: likelihood functions for the background and “signal plus background” hypotheses showing the definition of Type I (α) and Type II (β) errors.

5. Measure \mathbf{n} , finding the outcome \mathbf{n}_{obs} . If \mathbf{n}_{obs} lies in C , reject H_0 at the $(1 - \alpha)$ confidence level. If \mathbf{n}_{obs} falls in C^* then we have failed to exclude H_0 at the 95% confidence level.

The subtlety of this procedure is in the choice of C . If \mathbf{n}_i is a vector of continuous parameters, there is an infinite number of regions in the vector space that have a “size” of α (i.e. that contain 5% of the probability according to H_0). Consider, for simplicity, a situation with just one measured value n . Possible choices of C are shown in Figure 3.5 (left). The green region is valid, but not useful. One commonly-chosen region is the one-sided limit, shown in blue, where $C = [0, n_c]$ for some n_c such that $\int_0^{n_c} \rho(n|H_0) dn = \alpha$. Another is the two-sided, or central, region. This disconnected region (shown in red) is defined by $C = [0, n_{c_1}] \cup [n_{c_2}, \infty]$, where $\int_0^{n_{c_1}} \rho(n|H_0) dn = \int_{n_{c_2}}^{\infty} \rho(n|H_0) dn = \alpha/2$. Another choice sometimes used for two-sided limits is due to Crow and Gardener [28] (not shown in Figure 3.5) is $C = [0, n_{c_1}] \cup [n_{c_2}, \infty]$, where $\rho(n_{c_1}) = \rho(n_{c_2})$. This differs from the central limit definition above when the probability distribution is not symmetrical (such as for a Poisson process).

There is therefore some ambiguity in choosing C . Some choices (such as the green region in Figure 3.5) are obviously bad, but others are less clear-cut. The situation becomes even more ambiguous when we consider many measured variables \mathbf{n} and more complicated probability distributions. We need an “ordering principle” to choose the order in which we add points to the critical region. Another way of stating this is that we need to define a “test statistic” t , a function of \mathbf{n} that is large when \mathbf{n} is, in some sense, “hypothesis-like”, and small when \mathbf{n} is far from the values typically predicted by H_0 . This statistic can then act as a rank to decide in which order we add points \mathbf{n} to the region C . The critical region C is a potentially complicated (and possibly disconnected) region in the \mathbf{n} outcome space, but in this prescription maps to a connected interval in

t , i.e. $C = [0, t_c]$. Recognising that t is a function of \mathbf{n} , we can derive the probability density function for t and write

$$\alpha = \int_C \rho(\mathbf{n}|H_0) d^N \mathbf{n} = \int_0^{t_c} \rho(t|H_0) dt. \quad (3.15)$$

Similarly, we can redefine the expression for the p -value (previously defined in Equation 3.9) of a hypothesis H_0 in the light of a measurement \mathbf{n}_{obs} in terms of the test statistic as

$$p = \int_0^{t_{\text{obs}}} \rho(t|H_0) dt, \quad (3.16)$$

where $t_{\text{obs}} = t(\mathbf{n}_{\text{obs}})$.

3.4.2 Choosing the test statistic

One way to choose a suitable test statistic (equivalent to choosing a good critical region C) is to compare the null hypothesis to some alternative hypothesis H_1 . If the observed outcome \mathbf{n}_{obs} falls in C^* , we cannot exclude the null hypothesis at the $1 - \alpha$ confidence level. However, it might be the case that H_1 is correct, and we have mistakenly failed to reject H_0 in its favour. The probability (assuming H_1 is true) for this is

$$\beta = \int_{C^*} \rho(\mathbf{n}|H_1) d^N \mathbf{n}. \quad (3.17)$$

A good measure of a “good” critical region is to choose it in such a way as to minimise β or, equivalently, maximise the “statistical power” $1 - \beta$.

An alternative hypothesis H_1 is shown for the $N = 1$ case in Figure 3.5 (right), along with a reproduction of H_0 from the left-hand figure. In the context of Higgs searches, the scenario shown would correspond to a test of the SM Higgs hypothesis H_0 for some choice of Higgs mass, compared to the background-only hypothesis H_1 . In the figure shown, I have chosen the critical region to be the one-sided interval $C = [0, n_c]$. This interval is of “size” α (as shown shaded in blue). The quantity β defined above is shaded in red.

In general, the Neyman-Pearson lemma states that in order to choose a critical region that maximises the statistical power $1 - \beta$, there is no better choice than the ratio of likelihood functions of the two hypotheses. Take H_0 to be the modified SM hypothesis with a Higgs mass m_H and a signal strength parameter μ so that the number of events are given by $\mu \bar{\mathbf{s}} + \bar{\mathbf{b}}$. Define H_1 to be H_0 with $\mu = 0$, so that the number of expected events is given by $\bar{\mathbf{b}}$. In each case, $\bar{\mathbf{s}}$ and $\bar{\mathbf{b}}$ are functions of m_H . Let us define the likelihoods to be $\mathcal{L}(\mu, m_H|\mathbf{n}) = \rho(\mathbf{n}|H_0)$ and $\mathcal{L}(0|\mathbf{n}) = \rho(\mathbf{n}|H_1)$, giving the likelihood ratio

$$Q_\mu(\mathbf{n}) = \frac{\mathcal{L}(\mu, m_h|\mathbf{n})}{\mathcal{L}(0|\mathbf{n})}. \quad (3.18)$$

In fact, what is generally used in practice is the “log-likelihood ratio”

$$q_\mu(\mathbf{n}) = -2 \ln \left(\frac{\mathcal{L}(\mu, m_h | \mathbf{n})}{\mathcal{L}(0 | \mathbf{n})} \right). \quad (3.19)$$

One can then set limits on the signal-plus-background hypothesis H_0 after observing data \mathbf{n}_{obs} by calculating $q_\mu^{\text{obs}} = q_\mu(\mathbf{n}_{\text{obs}})$ and then evaluating the p -value

$$p = \int_{q_\mu^{\text{obs}}}^{\infty} \rho(q_\mu) dq_\mu \quad (3.20)$$

(noting that q_μ gets bigger as \mathbf{n} get less like H_0 in contrast to Q_μ , which has the inverse relationship).

In practice, this Neyman-Pearson test statistic is not used by the LHC collaborations; instead the “profiled log-likelihood ratio” is used due to its advantageous asymptotic properties. This is described in Section 3.4.4.

3.4.3 The CL_s method

A problem with the log-likelihood ratio defined in Equation 3.19 is that a test performed using the statistic has a chance of ruling out both the model under test *and* the background-only hypothesis due to the number of observed events being too low. A number of events *higher* than the background is easily explainable in terms of new physics giving extra contributions to the process being measured, but it is much harder to explain a *deficit* of events. Using the maxim “extraordinary claims require extraordinary evidence”, it would be desirable if our test became progressively less aggressive at ruling out a test hypothesis due to a deficit of events as μ approaches zero.

One method for protecting against this ruling out of background was used at LEP and was called the CL_s method. This method calls the usual p -value, calculated using the signal-plus-background hypothesis, CL_{s+b} , i.e.²

$$CL_{s+b} \equiv \int_{q_\mu^{\text{obs}}}^{\infty} \rho(q_\mu | H_0) dq_\mu. \quad (3.21)$$

The method then calls for one to calculate the same quantity (using the same test statistic q_μ), but using probability distribution function under the background-only hypothesis instead, i.e.

$$CL_b \equiv \int_{q_\mu^{\text{obs}}}^{\infty} \rho(q_\mu | H_1) dq_\mu. \quad (3.22)$$

²This notation is potentially confusing because a value of CL_{s+b} corresponds to a confidence level of $1 - CL_{s+b}$.

The quantity that is then quoted as the result of the test is then

$$CL_s = \frac{CL_{s+b}}{CL_b}. \quad (3.23)$$

If there is a good separation between the H_0 and H_1 hypothesis, and if the number of observed events are well above the predictions of H_1 , then CL_s is approximately equal to the standard p -value defined in Equation 3.20.

This CL_s method is also used at the LHC but, in contrast to the LEP method, it utilises the profiled log-likelihood test statistic defined in the next subsection.

3.4.4 Systematic and theory uncertainties

So far we have seen that the experimental observations are counts of numbers of events that pass particular cuts. To determine whether an event meets a cut requirement involves measuring kinematical properties of the final state particles in the tracking chambers and calorimeters of the detector and each of these measurements has some associated uncertainty. These experimental uncertainties, caused by incomplete understanding of the experimental apparatus, are systematic in the sense that measurements are consistently mis-measured in one direction. An example of an experimental uncertainty is the jet energy scale (JES): uncertainty in this quantity is one of the main source of experimental uncertainty in measurements involving jets in the final state [29]. The number of events one would expect to observe is a function of the JES because as the JES changes, jet energy measurements changes and so whether or not an event passes a kinematical cut changes. As such, the JES can be seen as *part of the model* with an attendant model parameter j . The number of expected events in a particular channel is then a function of the theoretical model parameters $\boldsymbol{\mu}$ (as always) *and* the JES parameter, once the effects of cuts are predicted: $\bar{n} = \bar{n}(\boldsymbol{\mu}, j)$. There will also be other extra parameters for each source of experimental uncertainty, which I do not show here.

In the previous section, we considered a model with some model parameters $\boldsymbol{\mu}$ (in particular, $\boldsymbol{\mu} = (m_H, \mu)$), and considered taking measurements \mathbf{n} from N counting experiments. We then formed a probability density function for each experiment and multiplied them together to give a joint probability density for observing the data \mathbf{n} , given the model $\boldsymbol{\mu}$. We can extend this to include the new model parameter by considering an additional “calibration” experiment measuring some observable J . This observable is chosen so that its predicted expectation value \bar{J} is a function of j (and, for simplicity, assume that it is not a function of the other parameters). We would write down a probability density function $\rho(J|j)$. In this expanded picture, we can write a

joint probability density

$$\rho(\mathbf{n}, J|\boldsymbol{\mu}, j) \propto \prod_{i=1}^N \exp \left[-\frac{(n_i - \bar{n}_i(\boldsymbol{\mu}, j))^2}{2\bar{n}_i(\boldsymbol{\mu}, j)} \right] \times \rho(J|j). \quad (3.24)$$

If we then performed the calibration experiment and measure a value $J = J_{\text{obs}}$, we could use the probability density function to deduce a best-fit value \hat{j} of the model parameter j , and also a standard deviation σ_j . Let $\tilde{n}_i = \bar{n}_i(\boldsymbol{\mu}, \hat{j})$. If varying j one standard deviation σ_j from its estimated value \hat{j} leads to a deviation in \bar{n}_i of Δ_j and if \bar{n}_i is distributed about \tilde{n}_i as a Gaussian with standard deviation of Δ_j , then we can make a change of variables $j \rightarrow \theta_j$ so that the joint probability density function looks like

$$\rho(\mathbf{n}|\boldsymbol{\mu}, \theta_j) \propto \prod_{i=1}^N \exp \left[-\frac{(n_i - \bar{n}_i(\boldsymbol{\mu}, \theta_j))^2}{2\bar{n}_i(\boldsymbol{\mu}, \theta_j)} \right] \times e^{-\theta^2/2}, \quad (3.25)$$

where $\bar{n}_i(\boldsymbol{\mu}, \theta_j) = \tilde{n}_i \times (1 + \theta_j \Delta_j)$.

In general, we can introduce all sources of experimental error as new effective model parameters which we can write as $\boldsymbol{\theta} = (\theta_1, \theta_2, \dots)$. The joint probability density function becomes

$$\rho(\mathbf{n}|\boldsymbol{\mu}, \boldsymbol{\theta}) \propto \prod_{i=1}^N \exp \left[-\frac{(n_i - \bar{n}_i(\boldsymbol{\mu}, \boldsymbol{\theta}))^2}{2\bar{n}_i(\boldsymbol{\mu}, \boldsymbol{\theta})} \right] \times \rho(\boldsymbol{\theta}). \quad (3.26)$$

3.4.5 LHC procedure for limits and discovery

Consider again the generalised standard model with two free parameters m_H and μ . Usually, m_H is fixed at some value and the likelihood function, defined by

$$\mathcal{L}(\mu, \boldsymbol{\theta}|\mathbf{n}) \equiv \rho(\mathbf{n}|\mu, \boldsymbol{\theta}). \quad (3.27)$$

is interpreted as a function of μ and the experimental “nuisance” parameters $\boldsymbol{\theta}$ only. The “profiled log-likelihood ratio” is then defined as

$$\tilde{q}_\mu = -2 \ln \left(\frac{\mathcal{L}(\mu, \hat{\boldsymbol{\theta}}_\mu|\mathbf{n})}{\mathcal{L}(\hat{\mu}, \hat{\boldsymbol{\theta}}|\mathbf{n})} \right), \quad 0 \leq \hat{\mu} \leq \mu. \quad (3.28)$$

In the denominator, the hatted quantities are values that maximise the likelihood function for the given value of \mathbf{n} . In the numerator, $\hat{\boldsymbol{\theta}}_\mu$ is the value of $\boldsymbol{\theta}$ that maximises the likelihood for given \mathbf{n} and μ . As such, the statistic is a function of μ , but not $\boldsymbol{\theta}$. We have “marginalised” over the nuisance parameters $\boldsymbol{\theta}$. The lower constraint on $\hat{\mu}$ is from the requirement that the signal be non-zero (to avoid a statistical downwards fluctuation ruling out background). The upper constraint forces the the test to be one-sided so that the signal hypothesis cannot be ruled out by the excess being too *large*.

This is the test statistic used to set limits and quantify discovery at the LHC by both ATLAS and CMS. Note that this is different from the Neyman-Pearson test statistic defined in Equation 3.19.

When no, or small, excesses of events beyond the background expectations were seen at the LHC, ATLAS and CMS used Equation 3.28 to compute CL_s , defined in Equation 3.23. This was done for a range of choices of m_H and μ . If $CL_s < 0.05$ then the hypothesis (for that choice of m_H and μ) was rejected at the 95% confidence level. To form the ‘‘Brazil band’’ exclusion plots, ATLAS and CMS followed the method described in Equation 3.3.2, but using CL_s instead of the simple p -value defined in Equation 3.9.

Once the excess of events around 125 GeV began to be observed, the local p -value was calculated for each m_H hypothesis using the background-only form of Equation 3.28, i.e.

$$\tilde{q}_0 = -2 \ln \left(\frac{\mathcal{L}(0, \hat{\boldsymbol{\theta}}_0 | \mathbf{n})}{\mathcal{L}(\hat{\mu}, \hat{\boldsymbol{\theta}} | \mathbf{n})} \right), \quad \hat{\mu} \geq 0. \quad (3.29)$$

3.5 Higgs phenomenology in theories beyond the Standard Model

The main focus of this thesis is to use the Higgs results from the LHC, presented by ATLAS and CMS using the language and techniques explained above, to help discover or constrain Beyond the Standard Model (BSM) theories. In this section I outline a framework in one can parameterise deviations (in the Higgs sector) of a broad class of BSM models.

In BSM theories with one Higgs-like particle (or at least only one Higgs-like particle with a mass close to 125 GeV), the Higgs couplings to the SM particles can be parameterised using the effective Lagrangian

$$\begin{aligned} \mathcal{L}_H = & \frac{2m_W^2 c_W}{v} HW_\mu^- W^{+\mu} + \frac{2m_Z^2 c_Z}{v} HZ_\mu Z^\mu - \sum_f \frac{m_f c_f}{v} H \bar{f} f \\ & + \frac{g_{H\gamma\gamma}}{v} H F_{\mu\nu} F^{\mu\nu} + \frac{g_{Hgg}}{v} H G_{\mu\nu}^a G^{a\mu\nu}, \end{aligned} \quad (3.30)$$

where the sum on the first line is over the SM fermions f . In the SM at tree level, the c parameters are all unity and the g parameters vanish. At one-loop level, however, effective g couplings can be deduced by calculating the partial width of the Higgs to gluons and photons. The one-loop diagrams contributing to these amplitudes are shown in Figure 3.6.

Decays to gluons proceeds at the one-loop level by a triangle loop of quarks. The diagram is proportional to the Yukawa coupling of the quark, so the top quark loop dominates. For the diphoton decay, there is also a contribution from a triangle loop of quarks with

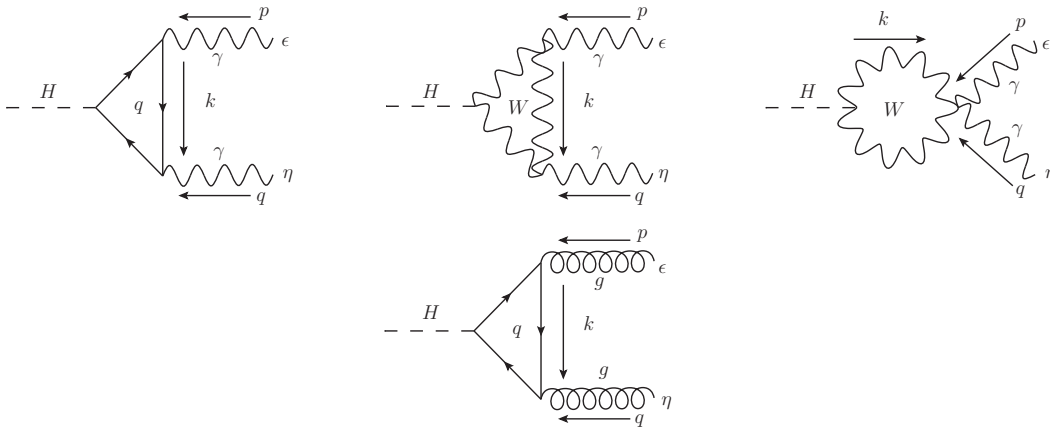


Figure 3.6: Leading order diagrams for $H \rightarrow \gamma\gamma$ and $H \rightarrow gg$ in the Standard Model, showing momentum and polarisation conventions used later in calculations. The W contributions are shown in the unitary gauge.

the top quarks dominating by the same argument.³ However, the dominant contribution to the amplitude is from loops of W bosons as we will see below, and the top quark and W interfere destructively with one another. The diagrams containing W bosons shown in Figure 3.6 are in the unitary gauge: in a general R_ξ gauge there would be additional diagrams containing Goldstone bosons and Faddeev-Popov ghosts.

The momentum and gluon and photon polarisation dependence can be factored out by writing the amplitudes in the form

$$\mathcal{A} = \tilde{\mathcal{A}}[(p \cdot q)(\epsilon \cdot \eta) - (p \cdot \eta)(q \cdot \epsilon)], \quad (3.31)$$

where the external vector particles with momenta p and q have polarisation vectors ϵ and η respectively. These polarisation and momentum conventions are shown in Figure 3.6. When calculating the width, one puts the Higgs on mass shell and requires the gluons to be transversely polarised, so the above expression simplifies to

$$\mathcal{A} = \tilde{\mathcal{A}} \left[\frac{m_H^2}{2} (\epsilon \cdot \eta) - (p \cdot \eta)(q \cdot \epsilon) \right], \quad (3.32)$$

where m_H is the Higgs mass.

If one calculates the Higgs partial width to gluons and photons from the one-loop diagrams and then matches these to the expressions obtained from using the effective

³Charged leptons can also contribute to this loop in the diphoton case, but these make very minor contributions due to their small Yukawa couplings.

vertices in Equation 3.30,

$$\Gamma_{gg} = \frac{2m_H^3}{\pi} \left| \frac{g_{Hgg}}{v} \right|^2 \quad (3.33)$$

$$\Gamma_{\gamma\gamma} = \frac{m_H^3}{4\pi} \left| \frac{g_{H\gamma\gamma}}{v} \right|^2 \quad (3.34)$$

one obtains

$$g_{Hgg}^{\text{SM}} = \frac{\alpha_s}{16\pi} \left| \sum_q F_{1/2}(\tau_q) \right| \quad (3.35a)$$

$$g_{H\gamma\gamma}^{\text{SM}} = \frac{\alpha}{8\pi} \left| F_1(\tau_W) + \sum_f N_c^f Q_f^2 F_{1/2}(\tau_f) \right|. \quad (3.35b)$$

where

$$\tau_f \equiv \frac{4m_f^2}{m_H^2}, \quad \tau_W \equiv \frac{4m_W^2}{m_H^2}. \quad (3.36)$$

The sum in the Hgg vertex is over all quark flavours q , whereas the sum in the $H\gamma\gamma$ vertex is over all quark and lepton flavours f . Here Q_f is the QED charge of the flavour f , and N_c^f is a colour multiplicity factor that is equal to 1 for leptons and 3 for quarks. The functions F_1 and $F_{1/2}$ are the results of performing a loop integral over a particle with the labelled spin. For completeness, I define the scalar loop function F_0 as well, which can appear in theories beyond the Standard Model:

$$F_{1/2}(\tau) \equiv 2\tau [1 + (1 - \tau)f(\tau)] \quad (3.37a)$$

$$F_1(\tau) \equiv -2 - 3\tau - 3\tau(2 - \tau)f(\tau) \quad (3.37b)$$

$$F_0(\tau) \equiv -\tau(1 - \tau f(\tau)) \quad (3.37c)$$

where

$$f(\tau) \equiv \begin{cases} \arcsin^2 \frac{1}{\sqrt{\tau}} & \tau \geq 1 \\ -\frac{1}{4} \left[\log \frac{1 + \sqrt{1 - \tau}}{1 - \sqrt{1 - \tau}} - i\pi \right]^2 & \tau \leq 1 \end{cases}. \quad (3.38)$$

where These functions quickly approach the asymptotic values $F_{1/2}(\tau) \rightarrow \frac{4}{3}$, $F_1(\tau) \rightarrow -7$ and $F_0(\tau) \rightarrow \frac{1}{3}$ as $\tau \rightarrow \infty$. In particular this means that the ratio of W to top quark contribution is

$$\begin{aligned} W : t &= F_1(\tau_W) : N_c^t Q_t^2 F_{1/2}(\tau_t) \\ &\approx -7 : 3 \times (2/3)^2 \times (4/3) \\ &\approx -7 : (16/9) \\ &\approx -3.9 : 1. \end{aligned} \quad (3.39)$$

For theories beyond the Standard model (BSM), other particles could flow in the loops,

including scalar particles that do not occur in the SM. The general couplings can be written as

$$g_{Hgg}^{\text{BSM}} = \frac{\alpha_s}{16\pi} \left| \sum_q F_{1/2}(\tau_q) + \sum_F C(R_F) F_{\text{spin}(F)}(\tau_F) \right| \quad (3.40a)$$

$$g_{H\gamma\gamma}^{\text{BSM}} = \frac{\alpha}{8\pi} \left| F_1(\tau_W) + \sum_f N_c^f Q_f^2 F_{1/2}(\tau_f) + \sum_F N_c^F Q_F^2 F_{\text{spin}(F)}(\tau_F) \right|. \quad (3.40b)$$

The extra terms in above equation (compared to Equation 3.35) are contributions from new flavours of particles F . The new factor in the g_{Hgg}^{BSM} expression is the normalisation of the $\text{SU}(3)_c$ generators in the representation F lives in, i.e. $\text{tr}(t_{R_F}^a t_{R_F}^b) = C(R_F) \delta^{ab}$ (see, for example [30]).

The $F_{\text{spin}(F)}$ functions above are given by Equation 3.37 provided that the new particles F have SM-like couplings to the Higgs, i.e. that their masses m_F are due purely to EWSB such that the couplings are

$$y_{HFF} = \begin{cases} \frac{m_F}{v} & (\text{fermion}) \\ \frac{2m_F^2}{v} & (\text{bosons}). \end{cases} \quad (3.41)$$

For many BSM theories, however, the new particles get their masses from other sources (e.g. supersymmetry breaking in SUSY theories; Kaluza-Klein compactification in theories with Extra Dimensions; or dynamical masses in theories involving strong dynamics). In these cases, compensating factors must be introduced.

Chapter 4

Minimal Universal Extra Dimensions

Theories with universal extra dimensions (UED) are very promising for solving puzzles in the Standard Model. Extra dimensions of space are motivated by String Theory (which requires them to be self-consistent) which itself was proposed to solve the problem of quantum gravity. It was believed that the extra dimensions in string theory would typically be compactified at scales of around the Planck mass of 10^{19} GeV. However, in [31] it was shown dimensions as large as a millimetre are compatible with String Theory. This realisation motivated the study of field theories with “large” (compared to the Planck scale).

The UED framework was proposed by Appelquist *et al* [32], following the suggestion of the existence of large (i.e. millimetre-scale) extra dimensions [33] or a warped (Planck-scale) extra dimension [34]. In UED, unlike in the preceding extra dimension models, all SM particles are postulated to propagate in a TeV^{-1} -sized bulk (normal space plus the extra compactified dimensions). Models of UED provide solutions to problems such as explaining the three fermion generations in terms of anomaly cancellation [35], and providing a mechanism for a sufficient suppression of proton decay [36]. Moreover, UED models can naturally incorporate a \mathbb{Z}_2 symmetry called KK parity, analogous to R parity in supersymmetry, leading to a well-motivated Dark Matter candidate [37, 38].

In this chapter I first introduce the minimal formalism of Universal Extra Dimensions (MUED), starting with an explanation of spatial “compactification” in the first section, explaining the necessity of manipulating the description of the extra dimension further in order to achieve chiral interactions in Section 4.2, and finally specifying the field content of the theory and building the Lagrangian in Section 4.3. I discuss the importance of residual 5D Lorentz symmetry, defining KK number and KK parity and explaining how the latter leads to a good Dark Matter candidate in Section 4.4. Then, in Section 4.5, I discuss a research project I did to produce a consistent software implementation of the

MUED model in order to facilitate rapid and accurate exploration of its phenomenology. This implementation consistently included both radiative mass corrections (which break the near-degeneracy of the mass spectrum and thus dictate the allowed particle decays and their branching ratios). I then show how I used CalcHEP to deduce the mass spectrum and decay modes, the unitary behaviour of KK WW scattering, and present the most promising discovery signature in the form of the tri-lepton final state in Sections 4.6, 4.7 and 4.8 respectively. Finally, I discuss how I used LHC Higgs search data to constrain the MUED parameter space in Section 4.9 and present my conclusions for this chapter in Section 4.10.

4.1 Compactification

In UED, there are a number of extra spatial dimensions (in addition to the usual three) in which all fields can vary. In the simplest version of the theory, known as minimal UED (MUED), there is a single extra dimension, labelled by y or x_5 . One way to explain our non-observation of this extra dimension is to posit that it is “compactified” (curled up). The simplest example of a 1D compactification is the circle, S^1 . Requiring that all fields are periodic in y means that their behaviour in the y direction can be written as a sum of KK modes. A scalar field, for example, can be parameterised as

$$\phi(x, y) = \frac{1}{\sqrt{2\pi R}} \left[\phi^0(x) + 2 \sum_{n=1}^{\infty} \left(\phi_+^{(n)}(x) \cos\left(\frac{ny}{R}\right) + \phi_-^{(n)}(x) \sin\left(\frac{ny}{R}\right) \right) \right] \quad (4.1)$$

where the Fourier coefficients are functions of the usual four non-compactified spacetime dimensions.

A Lagrangian can be formed from 5D fields in the same way as in 4D and then the action

$$S = \int d^5x \mathcal{L}_5(x, y) = \int_0^{2\pi R} dy \int d^4x \mathcal{L}(x, y) \quad (4.2)$$

is formed by integrating the 5D expression over all spacetime dimensions. Usually, one is not interested in computing correlation functions between different points along the fifth dimension so one expands the fields as in Equation 4.1 and performs the integral over y . The action can then be written as $S = \int d^4x \mathcal{L}(x)$ in terms of an effective 4D Lagrangian

$$\mathcal{L}(x) = \int_0^{2\pi R} dy \mathcal{L}_5(x, y). \quad (4.3)$$

The 4D Lagrangian is a function of the Fourier modes of the 5D fields and so these “Kaluza-Klein” (KK) modes can be considered 4D fields with associated particles. The integer n is called the KK number. Let us briefly consider the simple free, massive scalar field Lagrangian

$$\mathcal{L}_5 = \frac{1}{2} \partial_M \phi \partial^M \phi - \frac{m_0^2}{2} \phi^2. \quad (4.4)$$

The kinetic term involves derivatives in all five spacetime directions, $M = (\mu, 5)$. Upon Fourier (or “KK”) expansion, the 5D kinetic term will provide 4D kinetic terms for each KK mode as well as terms involving the derivatives with respect to y . These derivatives will not act on the zero mode $\phi^{(0)}(x)$, but will act on the sine and cosine wavefunctions that depend on y . After integrating the 5D Lagrangian, this will yield

$$\begin{aligned} \mathcal{L} = & \partial_\mu \phi^{(0)} \partial^\mu \phi^{(0)} - \frac{m_0^2}{2} \left(\phi^{(0)} \right)^2 \\ & + \sum_{n=1}^{\infty} \left(\partial_\mu \phi_+^{(n)} \partial^\mu \phi_+^{(n)} - \frac{m_n^2}{2} \left(\phi_+^{(n)} \right)^2 + \partial_\mu \phi_-^{(n)} \partial^\mu \phi_-^{(n)} - \frac{m_n^2}{2} \left(\phi_-^{(n)} \right)^2 \right), \end{aligned} \quad (4.5)$$

where

$$m_n^2 = m_0^2 + \frac{n^2}{R^2}. \quad (4.6)$$

The normalisation in Equation 4.1 was chosen to leave the KK modes canonically organised after the integration.

So, the KK modes form two “towers” of particles, $\phi_+^{(n)}$ and $\phi_-^{(n)}$, where the two particles at each KK level have the same mass. The mass receives a contribution from the zero-level mass m_0 and a KK contribution from the 5D kinetic term n/R . Physically, this can be understood as (discretised) kinetic energy from the 5D particle’s motion around the compact dimension.

If we want to use the machinery of Kaluza and Klein above to build a quantum field theory that explains reality, we must account for the existence of the infinite tower of KK particles. This can be explained by requiring the compactification scale R^{-1} to be large so that KK particles are not produced in particle collisions that routinely occur in nature and in our particle accelerators. This limits R^{-1} to be around the TeV scale or above.

4.2 Chirality from orbifolding

As we saw in Chapter 2, we know that the fermions we have observed in only interact with the weak W boson with their left-handed component. It is said that these fermions undergo “chiral” interactions, or simply that they are “chiral fermions”. Conversely, a fermion whose left- and right-handed components interacted equally with a gauge field would be called “vector-like” fermions.

Obtaining chiral interactions in 5D UED whilst trying to preserve 5D Lorentz symmetry at the local level is difficult. This issue can be traced to the fact that the 4D Lorentz group does not contain the parity operator. This means that fermions with a single chirality (e.g. left- or right-handed Weyl spinors) form a good representation of the Lorentz group. In contrast, in 5D (and indeed for any even number of spatial dimensions)

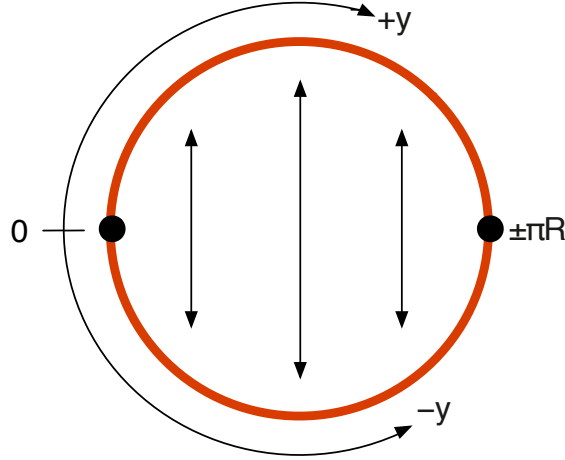


Figure 4.1: Turning a circle S^1 into an S^1/\mathbb{Z}_2 orbifold.

the parity operator is also a rotation of 180 degrees. For example, in 3D (i.e. two spatial dimensions), a spatial inversion through a point is equivalent to a rotation of 180 degrees about that point, but the same cannot be said for 4D. This means that Weyl spinors are not good representations of the 5D Lorentz group: Dirac spinors furnish the lowest dimensional representation. If one then writes down Lagrangian terms that treat left- and right-handed components differently, the result will not be invariant under Lorentz transformations.

The solution to this problem is to turn the circle (S^1) compactification into an “orbifold” compactification. Consider choosing y coordinate to be zero at some point on the circle and to range from $-\pi R$ to $+\pi R$, as shown in Figure 4.1. To produce the orbifold, we interpret the circle as a redundant parameterisation of a line segment as follows. Consider a discrete group $\mathbb{Z}_2 = (1, \mathcal{P})$, with $\mathcal{P}^2 = 1$. The \mathbb{Z}_2 inversion transformation \mathcal{P} acts on the coordinates as $y \mapsto \mathcal{P}y = -y$. We say that coordinates linked by this transformation are equivalent descriptions of the same physical point in space. This identifies the top and bottom segments of the circle with each other as shown in the figure: the physical space is actually a line segment of length πR . This space is described as an S^1/\mathbb{Z}_2 orbifold.

We can choose what representation of \mathbb{Z}_2 the fields transform under. Considering first a 5D scalar field, the simplest representation of \mathbb{Z}_2 would be (suppressing the x index) $\phi(y) \mapsto \mathcal{P}\phi(-y) = \phi(y)$. This field is described as “even” under \mathcal{P} . The simplest non-trivial transformation is would be $\phi(y) \mapsto \mathcal{P}\phi(-y) = -\phi(y)$ and such a field would be described as “odd”.

Because the two sides of the circle are both descriptions of the same physical space, $\phi(y)$ and $\phi(-y)$ should be seen as the representations of the true, geometric, value of the field

in two different coordinate systems related by \mathcal{P} , i.e.

$$\phi(-y) = \mathcal{P}\phi(y), \quad (4.7)$$

so for even (+) fields, $\phi_+(-y) = \phi_+(y)$ and for odd (-) fields, $\phi_-(-y) = -\phi_-(y)$.

The choice of even or odd transformation properties actually places boundary conditions on the fields at $y = 0, \pi R$. Concentrating on the $y = 0$ boundary, even fields must have the same value immediately either side of the boundary. This forces the y derivative of the field to vanish at $y = 0$, and similarly for $y = \pi R$, meaning the field obeys Neumann boundary conditions. For an odd field, the field values must have opposite signs either side of the boundaries and to this fixes the field *value* to vanish at $y = 0, \pi R$, imposing Dirichlet boundary conditions. The boundary conditions constrain the allowed terms in the KK expansion of the fields, so for a scalar field that can be even or odd under \mathcal{P} we have

$$\phi_+(x, y) = \frac{1}{\sqrt{\pi R}} \left[\phi^{(0)}(x) + 2 \sum_{n=1}^{\infty} \phi_+^{(n)}(x) \cos\left(\frac{ny}{R}\right) \right] \quad (4.8)$$

$$\phi_-(x, y) = \frac{2}{\sqrt{\pi R}} \sum_{n=1}^{\infty} \phi_-^{(n)}(x) \sin\left(\frac{ny}{R}\right). \quad (4.9)$$

For an odd field there is no zero mode, so all the particles are heavy.

For fields with multiple components, we can choose each of the components separately to be even or odd. For a five-vector field A_M in particular, we can choose the $M = \mu$ components to be even and the A_5 component to be odd. This means that there are four-vector zero modes $A_\mu^{(0)}$ but no spurious zero-mode 4D Lorentz scalars $A_5^{(0)}$.

We have seen that the orbifolding process “projects out” half of the degrees of freedom of the fields in the original circle compactification. We can use this to solve the problem of including chiral fermions in the 4D effective theory by choosing the 5D Dirac spinors to transform in such a way that only one of the chiralities survives at the zero-mode level. Let us consider two Dirac spinor representations of \mathbb{Z}_2 , ψ_L and ψ_R such that

$$\mathcal{P}\psi_L(-y) = -\gamma^5\psi_L(y) \quad (\text{even}) \quad (4.10)$$

$$\mathcal{P}\psi_R(-y) = +\gamma^5\psi_R(y) \quad (\text{odd}). \quad (4.11)$$

Under the L -type (hereafter also called “even”) representation, the left-handed component of the field remains unaltered and the right-handed component changes sign. The opposite holds for the R -type (“odd”) representation. This means that the KK

expansions for even and odd fermions on the orbifold are

$$\psi_L(x, y) = \frac{1}{\sqrt{\pi R}} \left[P_L \psi_L^0(x) + \sqrt{2} \sum_{n=1}^{\infty} \left(P_L \psi_L^{(n)}(x) \cos\left(\frac{ny}{R}\right) + P_R \psi_L^{(n)}(x) \sin\left(\frac{ny}{R}\right) \right) \right] \quad (4.12)$$

$$\psi_R(x, y) = \frac{1}{\sqrt{\pi R}} \left[P_R \psi_R^0(x) + \sqrt{2} \sum_{n=1}^{\infty} \left(P_R \psi_R^{(n)}(x) \cos\left(\frac{ny}{R}\right) + P_L \psi_R^{(n)}(x) \sin\left(\frac{ny}{R}\right) \right) \right], \quad (4.13)$$

where $P_{L,R}$ are the left and right projection operators defined in Equation 2.14. The notation used here is confusing, but standard. The fields $\psi_L(x, y)$ and $\psi_R(x, y)$ are full Dirac spinors: the L, R subscripts indicate which chirality survives at the zero mode level.

The prescription for building a quantum field theory from 5D fields is then fairly straightforward. We would like to reproduce the Standard Model particles and interactions (in particular the chiral interactions) with the addition of new, heavy R^{-1} -scale particles. The SM particles are identified as the zero KK modes of the 5D fields. To produce (say) a chiral 4D electron, we propose two 5D Dirac fields $e_L(x, y)$ and $e_R(x, y)$, choosing them to be part of a doublet and a singlet respectively under $SU(2)_W$. Upon compactification and orbifolding, only the left- and right-handed component of e_L and e_R respectively survive at the zero mode. So we have a left-handed 4D field $P_L e_L^{(0)}(x)$ which is part of an $SU(2)_W$ doublet and a right-handed 4D field $P_R e_R^{(0)}(x)$ that is a singlet under $SU(2)_W$. These can be interpreted as the left- and right-handed components of a single 4D Dirac field $e(x) = P_L e_L^{(0)}(x) + P_R e_R^{(0)}(x)$ which we identify with the SM electron, even though its chiral components come from different fundamental 5D fields.

Accompanying this single 4D Dirac fermion are *two* KK towers of 4D Dirac fermions. These KK fermions have vector-like weak couplings.

4.3 Field content and the Lagrangian

In MUED, the field content is chosen to be analogous to the SM, with all fields promoted to their 5D equivalents: all of the vector fields become five-vector fields and the left-(right-)handed Weyl spinors become even (odd) Dirac 5D spinors. The gauge group is $SU(3)_c \times SU(2)_W \times U(1)_Y$ and so we have eight gluons, three weak bosons and a hypercharge boson as in the SM, but in 5D. The matter content for MUED is shown in Table 4.1 (the gauge charge assignments are the same as in the SM). I have used uppercase letters to represent the 5D versions of SM fields except where I was already using uppercase (i.e. the quark and lepton doublets), in which case I have used calligraphic capitals. In addition to the matter fields and gauge fields, there is also a complex scalar

Field	\mathbb{Z}_2	$SU(3)_c$	$SU(2)_W$	$U(1)_Y$
$\mathcal{Q}_L = \begin{pmatrix} U_L \\ D_L \end{pmatrix}$	even	3	2	$\frac{1}{3}$
U_R	odd	3	1	$\frac{4}{3}$
D_R	odd	3	1	$-\frac{2}{3}$
$\mathcal{E}_L = \begin{pmatrix} N_L \\ E_L \end{pmatrix}$	even	1	2	-1
E_R	odd	1	1	-2

Table 4.1: Matter content of MUED. All of the fields are Dirac spinors.

field Φ which has hypercharge $Y = 1$ and transforms as a doublet of $SU(2)_w$, just as the Higgs field ϕ does in the SM.

The 5D MUED Lagrangian, before spontaneous symmetry breaking and gauge fixing, is

$$\begin{aligned}
\mathcal{L}_5 = & -\frac{1}{4}G_{MN}^a G^{aMN} - \frac{1}{4}W_{MN}^i W^{iMN} - \frac{1}{4}B_{MN}B^{MN} \\
& + i\bar{\mathcal{Q}}_L \Gamma^M \mathcal{D}_M \mathcal{Q}_L + i\bar{\mathcal{E}}_L \Gamma^M \mathcal{D}_M \mathcal{E}_L + i\bar{U}_R \Gamma^M \mathcal{D}_M U_R + i\bar{D}_R \Gamma^M \mathcal{D}_M D_R + i\bar{E}_R \Gamma^M \mathcal{D}_M E_R \\
& + (\mathcal{D}_M \Phi)^\dagger (\mathcal{D}^M \Phi) + \mu^2 \Phi^\dagger \Phi - \lambda^{(5)} (\Phi^\dagger \Phi)^2 \\
& - \left(y_u^{(5)} \bar{\mathcal{Q}}_L \tilde{\Phi} U_R + y_d^{(5)} \bar{\mathcal{Q}}_L \Phi D_R + y_e^{(5)} \bar{\mathcal{E}}_L \Phi E_R + \text{h.c.} \right),
\end{aligned} \tag{4.14}$$

where the covariant derivative

$$\mathcal{D}_M = \partial_M - ig_s^{(5)} G_M - ig^{(5)} W_M - ig'^{(5)} B_M \tag{4.15}$$

depends on the Lie algebra-valued gauge fields and the 5D coupling constants. Upon compactification, one sees that the latter are related to the SM couplings by the relation

$$g = \frac{g^{(5)}}{\sqrt{\pi R}} \tag{4.16}$$

in order to reproduce the conventional normalisation of the zero mode terms involving the couplings. Similarly, the 5D Yukawa terms and Quartic Higgs coupling are related to the SM values through

$$y = \frac{y^{(5)}}{\sqrt{\pi R}}, \quad \lambda = \frac{\lambda^{(5)}}{\pi R}, \tag{4.17}$$

and μ already has the correct mass dimension.

Equation 4.16 and Equation 4.17 indicate a potential problem with the theory: these 5D couplings have negative mass dimensions, which implies that the theory is not perturbatively renormalisable. This is a generic problem with theories involving extra spatial

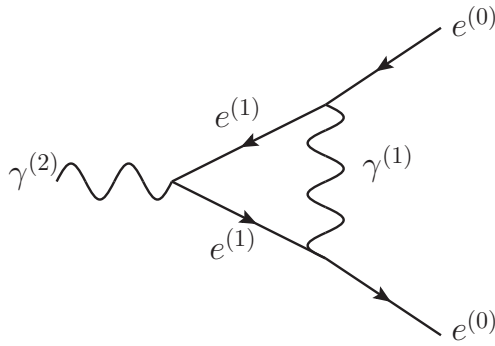


Figure 4.2: An example of a one-loop process that conserves KK number at each vertex and yet violates KK number by an even amount, globally, nevertheless preserving KK parity.

dimensions. However, the theory is still useful as an effective theory if we restrict ourselves to calculations involving energies well below some UV cutoff Λ . It is an assumption of MUED that all of the terms not shown in the Lagrangian above are zero at the cutoff scale Λ .

4.4 Lorentz symmetry, KK number and KK parity

The original circle compactification had translational invariance around the extra dimension which corresponds to momentum in that direction p_5 being conserved. The compactification discretises the allowed momenta in the fifth direction to be of the form nR^{-1} for integer KK number n . The relationship between momentum and KK number is not simply $p_5 = n/R$ when we describe the Fourier series in terms of sine and cosine wavefunctions, because n is always positive in this picture. KK number conservation should then be understood as the statement that, for any process involving particles with KK numbers l, m, n, \dots , the relation

$$\pm l \pm m \pm n \dots = 0 \quad (4.18)$$

must hold for some choice of the signs, each sign being chosen independently.

Orbifolding breaks the translational symmetry by singling out the two special boundary points so we would not expect KK number to be conserved in a general process. However, there is still translational invariance locally, everywhere except for the boundary points and so we expect KK number to be conserved locally. In practice, this means that we expect local interactions (i.e. the vertices in the Feynman rules of the theory) to obey the relation in Equation 4.18. However, non-local (i.e. loop-level) processes, such as the decay of a $n = 2$ KK photon into a SM electron-positron pair shown in Figure 4.2, can violate KK number.

The Lagrangian in Equation 4.14 is 5D Lorentz invariant, but we have seen that the dynamics it describes is clearly not. In principle we are free to add 5D Lorentz violating terms to the Lagrangian. These come in two types. There are terms that are localised by a delta function to the boundaries, e.g.

$$\delta\mathcal{L}_5 \propto \delta(y-0)\bar{E}_R\Gamma^M\mathcal{D}_ME_R, \quad (4.19)$$

known as ‘‘orbifold’’ terms. There are also terms (so-called ‘‘bulk’’ terms) that break Lorentz invariance in a non-local way; one way of building such a term is using Wilson lines. As an example, in a theory containing a 5D vector field $A_M(x,y)$, one could add a term to the 4d Lagrangian of the form

$$\delta\mathcal{L}_4 \propto \int_0^{\pi R} \int_0^{\pi R} \mathcal{D}_\mu W_{12}\mathcal{D}^\mu W_{21} dy_1 dy_2, \quad (4.20)$$

where

$$W_{12} \equiv W(x, y_1, y_2) = \exp\left(iq \int_{y_1}^{y_2} A_5(x, y) dy\right). \quad (4.21)$$

This contribution is gauge invariant but not 5D Lorentz invariant (it is, however, invariant under the 4D Lorentz group).

As stated above, in MUED we set all terms (including the above Lorentz violating terms) to zero at the cutoff scale. This imposes 5D Lorentz symmetry by hand on the Lagrangian and it is clearly not respected by the dynamics. Another way of seeing this is that, under renormalisation group (RG) running, bulk and orbifold Lorentz-violating terms are generated as we move down from the cutoff scale, despite having been initially set to zero.

There is one symmetry of the Lagrangian that *is* preserved at all loop levels (or, in the RG language, at all renormalisation scales): reflection symmetry about the centre of the line segment, i.e.

$$\mathcal{P}^{\text{KK}}_y = \begin{cases} \pi R - y & \text{if } 0 \leq y \leq \pi R \\ -\pi R - y & \text{if } -\pi R \leq y \leq 0. \end{cases} \quad (4.22)$$

Note that this is a different \mathbb{Z}_2 transformation from the one used to form the orbifold. This symmetry automatically holds if we have translational invariance. More generally, it still holds as long as the orbifold terms on each boundary are equal (which they trivially are if we set them to zero!).

The conserved quantity associated with this reflection symmetry is called KK parity

$$\text{KK parity} = (-1)^n, \quad (4.23)$$

where n is the KK number. The KK parity of an initial state must always equal that of the final state in any process. KK parities are combined multiplicatively.

The most important consequence of KK parity conservation is that the lightest $n = 1$ particle in the spectrum will be unable to decay into lighter SM particles: it will be absolutely stable. As we will see in Section 4.6, this lightest KK particle (dubbed the LKP, in homage to the LSP that is protected by R parity in Supersymmetry) can, in large regions of the parameter space, be the first KK mode of the photon. As such, it is an excellent candidate for a Dark Matter particle, satisfying the weakly-interacting massive particle (WIMP) scenario.

4.5 Implementing MUED in LanHEP and CalcHEP

We have seen that MUED is a simple extension of the SM that easily incorporates a Dark Matter particle in the form of the LKP. Extra dimensions are a feature of string theory, our best prospect for a quantum theory of gravity, and some of these could be large (i.e. TeV⁻¹-sized), so MUED is motivated from this theoretical direction too. It predicts new particles that could be observed at the LHC, and loop-level modifications of SM processes that could be observable. It is therefore important to confront MUED with existing experimental data as well as the new results coming from the LHC: to do that, we need to understand its phenomenology.

Testing a BSM theory at a collider like the LHC requires one to calculate cross-sections and decay widths for the different processes under investigation. Doing these calculations by hand can be error-prone and often prohibitively time-consuming. It is therefore extremely advantageous (and frequently imperative) to automate parts of the calculations using software tools. There are several packages commonly employed to calculate matrix elements (e.g. CalcHEP/CompHEP [39, 40] MadGraph [41]; and the Mathematica packages FeynArts [42] and FormCalc/LoopTools [43], which generate Feynman diagrams and evaluate the resulting matrix elements respectively). These packages take a list of Feynman rules, specified in some proprietary way, as their inputs. It is also always useful, and sometimes necessary, to automate the derivation of Feynman rules from a model's Lagrangian. Packages exist for this purpose too, such as LanHEP [44] and FeynRules [45] (each of which produce Feynman rules in formats suitable for several different matrix element generators and calculators).

This chapter describes work I did with others as part of the project described in [3] to produce a model of MUED¹ in LanHEP/CalcHEP in order to investigate its phenomenology. There were already existing public CalcHEP [46] and FeynRules [47] implementations, but neither had a KK Higgs sector, amongst other problems. For example, the CalcHEP model by the authors of [46] was in the unitary gauge only, and it was manually implemented directly in CalcHEP. In contrast, our model [3] (described later

¹The model is publicly available at the High Energy Model Database (HEP-MDB) in both Feynman-Hooft and unitary gauges at <https://hepmdb.soton.ac.uk/> under the name "MUED-BBMP".

in this chapter) made use of LanHEP to produce the CalcHEP model file in both the unitary and Feynman-'t Hooft gauges.

4.5.1 Loop-corrected masses

Before implementing MUED in CalcHEP, it is vital to note the importance of loop corrections on the model's phenomenology. At tree level, the masses of particles of KK number n are related to the zero mode mass m_0 by the simple relation

$$m_{\text{tree}}^2 = m_0^2 + \frac{n^2}{R^2}. \quad (4.24)$$

Perhaps surprisingly, this relation applies to fermions as well as bosons as will be shown in Section 4.5.2. The zero-mode masses come from electroweak symmetry breaking set by the scale of the vev $v = 246$ GeV, whereas the KK contributions come from the compactification scale R^{-1} , expected to be around 1 TeV. Therefore, the spectrum of the particles at a particular KK level is approximately degenerate, meaning decays would be highly kinematically suppressed. This means that loop corrections — in most theories considered to be small quantitative corrections — play a decisive role in MUED, breaking the degeneracy and setting the particle spectrum, therefore specifying the allowed decay modes of KK particles.

The radiative corrections to the masses have been calculated in [48] to one-loop order. The corrections can be split into three distinct types. First, there are the usual diagrams involving a single loop existing completely in the bulk (i.e. not passing through either of the boundaries of the extra dimension). These loops can be shrunk arbitrarily small (corresponding to integrating up to arbitrarily high momenta). They lead to 4D momentum cutoff-dependent corrections to all KK modes equally. There is also a sum over KK number n (corresponding to discretised momentum in the y direction) and if this sum is cut off at some number n_{max} , there will be linear dependence on this cutoff. These 4D and KK number cutoff dependences can be removed by renormalising the 5D kinetic term of the relevant field, i.e. performing a wavefunction renormalisation.

The second kind of radiative corrections are called “bulk corrections”. These are caused by diagrams with an internal loop passing through both of the boundary points at least once (equivalent to loops with nonzero winding number around the extra dimension, if interpreted as a circle). Such diagrams lead to finite corrections (because the loop cannot be shrunk to zero) to the gauge bosons only, and all the KK masses (but *not* the zero-mode masses) receive equal contributions. These corrections appear in both the circle and orbifold compactifications and could be absorbed by introducing non-local counter-terms into the Lagrangian such as the example in Equation 4.20.

Finally, there are so-called “orbifold corrections” which only appear in orbifold compactifications. These are diagrams with an internal loop in which a particle crosses one

of the boundaries and so these loops can be contracted to zero size, leading to divergences. Introducing cutoffs Λ and n_{\max} to regulate the divergences in the 4D momentum and KK number of the internal particle respectively, the (linear) dependence on n_{\max} can be absorbed by a wavefunction renormalisation as discussed above. The remaining corrections, not removed by this prescription, are proportional to the KK number of the external particles and logarithmically dependent on the 4D cutoff Λ . The relevant counter-terms to absorb this Λ dependence would be boundary-localised expressions such as the example in Equation 4.19.

The radiative corrections calculated in [48] are corrections to the terms quadratic in the KK modes of the fields, *before EWSB*. There are therefore no zero mode masses at this level, and the corrections

$$m_{\text{boson}}^{(n)} = \frac{n^2}{R^2} + (\delta m_{\text{boson}}^{(n)})^2 \quad (4.25)$$

$$m_{\text{fermion}}^{(n)} = \frac{n}{R} + \delta m_{\text{fermion}}^{(n)} \quad (4.26)$$

are quadratic for bosons and linear for fermions. The corrections take the form

$$(\delta m_{\text{vector}}^{(n)})^2 = a_V \frac{n^2}{R^2} + b_V, \quad (4.27)$$

$$(\delta m_{\text{scalar}}^{(n)})^2 = a_S \frac{n^2}{R^2}, \quad (4.28)$$

$$\delta m_{\text{fermion}}^{(n)} = a_F \frac{n}{R}, \quad (4.29)$$

where a_V , a_F and a_S are the 4D cutoff-dependent orbifold corrections and b_V is the cutoff-independent bulk correction; both types of coupling depend on the properties of the relevant fields. The corrections for all of the fields in MUED are given in [48]; as an example, the orbifold correction for the quark doublet \mathcal{Q} is

$$a_{\mathcal{Q}} = \frac{1}{16\pi^2} \left(3g_s^2 + \frac{27}{16}g^2 + \frac{1}{16}g'^2 \right) \ln \frac{\Lambda^2}{\mu^2}, \quad (4.30)$$

where μ is the 4D renormalisation scale at which the one-loop two-point function is evaluated; we typically set $\mu = R^{-1}$ when considering the production of $n = 1$ KK particles. As an example of the b_V coefficients, the bulk correction for the hypercharge boson B_M is

$$b_B = -\frac{39}{2} \frac{\zeta(3)g'^2}{16\pi^4} \frac{1}{R^2}, \quad (4.31)$$

where $\zeta(x)$ is the Riemann zeta function. The coupling constants in these two examples are the 4D SM values, related to the 5D couplings by Equation 4.16.

The question of how to incorporate these mass corrections into our CalcHEP model is subtle. If the masses were simply amended by hand, the theory would cease to be gauge invariant. Non-local and boundary-localised terms are impossible to include in the Lagrangian for use with LanHEP. In the end, we adopted a simple, but gauge invariant,

solution that consisted of altering the Lagrangian so that the fifth component part of the kinetic terms have a different normalisations compared to the 4D parts. Using a simple 5D real scalar field $\phi(x, y)$ as an example, the Lagrangian would be can be modified to read

$$\mathcal{L}_5 = \frac{1}{2} (\mathcal{D}_\mu \phi \mathcal{D}^\mu \phi - Z \mathcal{D}_5 \phi \mathcal{D}_5 \phi), \quad (4.32)$$

where the derivatives are gauge covariant. KK expanding the fields reveals the KK masses to be

$$(m_\phi^{(n)})^2 = Z_\phi \frac{n^2}{R^2}, \quad (4.33)$$

and so the normalisation is chosen to be

$$Z_\phi = 1 + \left(\frac{n^2}{R^2} \right)^{-1} (\delta m_\phi^{(n)})^2_{\text{orbifold}} = 1 + a_\phi, \quad (4.34)$$

where $(\delta m_\phi^{(n)})^2_{\text{orbifold}} = a_S n^2/R^2$ is the contribution to the square of the mass of ϕ due to the orbifold corrections discussed above: the Z factor is thus rendered KK number independent.

For vector bosons, the kinetic term for a gauge field A_M^a would be modified as

$$-\frac{1}{4} F_{MN}^a F^{MN a} \mapsto -\frac{1}{4} (F_{\mu\nu}^a F^{\mu\nu a} + 2Z_A F_{\mu 5}^a F^{\mu 5 a}), \quad (4.35)$$

yielding Equation 4.34 with $\phi \mapsto A$. Fermion kinetic terms are altered to be

$$i\bar{\psi}\gamma^M \mathcal{D}_M \psi \mapsto i\bar{\psi}\gamma^\mu \mathcal{D}_\mu \psi + i\bar{\psi}\gamma^5 \mathcal{D}_5 \psi \quad (4.36)$$

with

$$Z_\psi = 1 + \left(\frac{n}{R} \right)^{-1} (\delta m_\psi^{(n)})^2_{\text{orbifold}} = 1 + a_\psi. \quad (4.37)$$

This insertion of the Z normalisation clearly breaks 5D Lorentz invariance, although we expect this to be broken anyway by the compactification. Technically, the orbifold corrections would induce boundary-localised counter-terms, rather than this “wavefunction renormalisation” factor: our method can be seen as “smearing out” the boundary delta function across the entire extra dimension. Most importantly, the wavefunction renormalisation prescription does not break gauge invariance, in contrast to naively adding masses by hand. It does, however, fail to include the mass mixing of different KK levels that localised boundary terms would induce, though this mixing is small and safely neglected.

Performing this procedure for the whole MUED Lagrangian gives

$$\begin{aligned}
\mathcal{L}_5 = & -\frac{1}{4}G_{\mu\nu}^a G^{a\mu\nu} - \frac{1}{4}B_{\mu\nu}B^{\mu\nu} - \frac{1}{4}W_{\mu\nu}^i W^{i\mu\nu} \\
& + \frac{Z_G}{2}G_{\mu 5}^a G^{a\mu}_5 + \frac{Z_B}{2}B_{\mu 5}B^\mu_5 + \frac{Z_W}{2}W_{\mu 5}^i W^{i\mu}_5 \\
& + i\bar{Q}_L\gamma^\mu\mathcal{D}_\mu Q_L + i\bar{\mathcal{E}}_L\gamma^\mu\mathcal{D}_\mu\mathcal{E}_L + i\bar{U}_R\gamma^\mu\mathcal{D}_\mu U_R + i\bar{D}_R\gamma^\mu\mathcal{D}_\mu D_R + i\bar{E}_R\gamma^\mu\mathcal{D}_\mu E \\
& - Z_Q\bar{Q}_L\gamma^5\mathcal{D}_5 Q_L - Z_{\mathcal{E}}\bar{\mathcal{E}}_L\gamma^5\mathcal{D}_5\mathcal{E}_L - Z_U\bar{U}_R\gamma^5\mathcal{D}_5 U_R - Z_D\bar{D}_R\gamma^5\mathcal{D}_5 D_R - Z_E\bar{E}_R\gamma^5\mathcal{D}_5 E_R \\
& + (\mathcal{D}_\mu\Phi)^\dagger(\mathcal{D}^\mu\Phi) - Z_\Phi(\mathcal{D}_5\Phi)^\dagger(\mathcal{D}_5\Phi) + \mu^2\Phi^\dagger\Phi - \lambda^{(5)}(\Phi^\dagger\Phi)^2 \\
& - \left(y_u^{(5)}\bar{Q}_L\tilde{\Phi}U_R + y_d^{(5)}\bar{Q}_L\Phi D_R + y_e^{(5)}\bar{\mathcal{E}}_L\Phi E_R + \text{h.c.}\right),
\end{aligned} \tag{4.38}$$

where the wavefunction renormalisations are given by

$$\begin{aligned}
Z_Q &= 1 + \left(3\frac{g_s^2}{16\pi^2} + \frac{27}{16}\frac{g^2}{16\pi^2} + \frac{1}{16}\frac{g'^2}{16\pi^2}\right)\ln\frac{\Lambda^2}{\mu^2} \\
Z_U &= 1 + \left(3\frac{g_s^2}{16\pi^2} + \frac{g'^2}{16\pi^2}\right)\ln\frac{\Lambda^2}{\mu^2} \\
Z_D &= 1 + \left(3\frac{g_s^2}{16\pi^2} + \frac{1}{4}\frac{g'^2}{16\pi^2}\right)\ln\frac{\Lambda^2}{\mu^2}, \\
Z_{\mathcal{E}} &= 1 + \left(\frac{27}{16}\frac{g^2}{16\pi^2} + \frac{9}{16}\frac{g'^2}{16\pi^2}\right)\ln\frac{\Lambda^2}{\mu^2}, \\
Z_E &= 1 + \frac{9}{4}\frac{g'^2}{16\pi^2}\ln\frac{\Lambda^2}{\mu^2}, \\
Z_B &= 1 + \left(-\frac{1}{6}\right)\frac{g'^2}{16\pi^2}\ln\frac{\Lambda^2}{\mu^2}, \\
Z_W &= 1 + \frac{15}{2}\frac{g^2}{16\pi^2}\ln\frac{\Lambda^2}{\mu^2}, \\
Z_G &= 1 + \frac{23}{2}\frac{g_s^2}{16\pi^2}\ln\frac{\Lambda^2}{\mu^2}, \\
Z_\Phi &= 1 + \left(\frac{3}{2}g^2 + \frac{3}{4}g'^2 - \frac{m_H^2}{v^2}\right)\frac{1}{16\pi^2}\ln\frac{\Lambda^2}{\mu^2}.
\end{aligned} \tag{4.39}$$

The mass corrections above do not include contributions involving Yukawa couplings because these are negligible at this one-loop order, except for the large top quark Yukawa. Including this top quark Yukawa contribution leads to mass corrections for the KK modes of the third generation quark doublet and the top quark singlet, detailed in [48]. We incorporate these corrections into our model in a gauge-invariant way by writing the relevant wavefunction renormalisation factors differently compared to the other generations, i.e.,

$$-Z_{\mathcal{T}}\bar{\mathcal{T}}_L\gamma^5\mathcal{D}_5\mathcal{T}_L - Z_T\bar{T}_R\gamma^5\mathcal{D}_5 T_R - Z_D\bar{B}_R\gamma^5\mathcal{D}_5 B_R \tag{4.40}$$

where $\mathcal{T}_L = (T_L, B_L)$ is the third generation quark doublet and T_R and B_R are third generation SU(2) singlet quark fields (all fields are 5D). The B_R quark receives the

standard down-type wavefunction renormalisation.

Bulk corrections cannot be incorporated using this method because they do not depend on KK number in the correct way to render Z a constant. Fortunately, bulk corrections only affect the gauge bosons, and are given, according to [48], by

$$(\delta m_B^{(n)})^2 = -\frac{39}{2} \frac{\zeta(3) g'^2}{16\pi^4} \frac{1}{R^2} \quad (4.41)$$

$$(\delta m_W^{(n)})^2 = -\frac{5}{2} \frac{\zeta(3) g^2}{16\pi^4} \frac{1}{R^2} \quad \text{for } n \geq 1. \quad (4.42)$$

$$(\delta m_G^{(n)})^2 = -\frac{3}{2} \frac{\zeta(3) g_s^2}{16\pi^4} \frac{1}{R^2} \quad (4.43)$$

From these formulae, one can easily check that the corrections for W and G are both small numerically compared to the orbifold corrections and so can be ignored. The B bulk correction is not negligible compared to the orbifold contribution, but the weak coupling g' is so small that both bulk and brane couplings are negligible compared to the tree level mass n/R . In our CalcHEP model, we have neglected bulk corrections entirely.

4.5.2 Diagonalising the fermions

Here I outline how the fermion sector is diagonalised in MUED. Firstly, the 5D Higgs field Φ acquires a vev $v^{(5)}$. This is related to the SM vev v by $v^{(5)} = v/\sqrt{\pi R}$. Expanding Φ about its vev, and keeping only Yukawa terms quadratic in (for example) the U_L and U_R fields gives

$$\mathcal{L}_5 \supset -\frac{y_u^{(5)} v^{(5)}}{\sqrt{2}} (\bar{U}_L U_R + \bar{U}_R U_L), \quad (4.44)$$

and it worth noting again that all of the fields above are full Dirac fields: the L and R subscripts are just labels. KK expanding the fermion fields with the correct normalisation and integrating over the extra dimension y gives

$$\begin{aligned} \mathcal{L} \supset & -\frac{y_u v}{\sqrt{2}} \left\{ \bar{u}_L^{(0)} P_R u_R^{(0)} + \bar{u}_R^{(0)} P_L u_L^{(0)} \right. \\ & \left. + \sum_{n=1}^{\infty} \left[\bar{u}_L^{(n)} P_R u_R^{(n)} + \bar{u}_L^{(n)} P_L u_R^{(n)} + \bar{u}_R^{(n)} P_L u_L^{(n)} + \bar{u}_R^{(n)} P_R u_L^{(n)} \right] \right\} \end{aligned} \quad (4.45)$$

$$\supset -m_u \sqrt{2} \left\{ \bar{u} u + \sum_{n=1}^{\infty} \left(\bar{u}_L^{(n)} u_R^{(n)} + \bar{u}_R^{(n)} u_L^{(n)} \right) \right\}, \quad (4.46)$$

where the zero modes from U_L and U_R combine to form the SM up quark, given by $u = P_L u_L^{(0)} + P_R u_R^{(0)}$, with mass $m_u = y_u v/\sqrt{2}$. So the Yukawa terms do not form mass terms for the KK modes of the interaction eigenstate field: they form mass mixing terms, which means the system of fields must be diagonalised. The fifth-component parts of the kinetic terms for U_L and U_R do yield mass terms for the KK modes; the combination

of the Yukawa and KK contributions to the n th KK mode of U_L and U_R can therefore be written as a mass matrix

$$\begin{pmatrix} -Z_U \frac{n}{R} & m_u \\ m_u & Z_Q \frac{n}{R} \end{pmatrix}. \quad (4.47)$$

This matrix can be diagonalised by refining the interaction eigenstates $u_{L,R}^{(n)}$ in terms of mass eigenstates $u_{1,2}^{(n)}$ through

$$\begin{pmatrix} u_R^{(n)} \\ u_L^{(n)} \end{pmatrix} = \begin{pmatrix} -\gamma^5 \cos \alpha_u^{(n)} & \sin \alpha_u^{(n)} \\ \gamma^5 \sin \alpha_u^{(n)} & \cos \alpha_u^{(n)} \end{pmatrix} \begin{pmatrix} u_1^{(n)} \\ u_2^{(n)} \end{pmatrix} \quad (4.48)$$

where the γ^5 matrices are to ensure both masses

$$m_{u_{\{1,2\}}^{(n)}} = \frac{1}{2} \left[\frac{Z_Q + Z_U}{\cos(2\alpha_u^{(n)})} \mp (Z_Q - Z_U) \right] \frac{n}{R} \quad (4.49)$$

are positive. The mixing angle $\alpha_u^{(n)}$ is given by

$$\tan(2\alpha_u^{(n)}) = \frac{2m_u}{(Z_Q + Z_U)n/R}. \quad (4.50)$$

Similar expressions hold for the other fermions (except for neutrinos).

In the absence of loop corrections (i.e., setting the Z coefficients to unity), the mixing angle at the n th KK level simplifies to

$$\tan(2\alpha_{u,\text{tree}}^{(n)}) = \frac{m_u}{n/R}, \quad (4.51)$$

and when this is substituted into Equation 4.49, the masses of $u_{1,2}^{(n)}$ become degenerate with values

$$m_{u_{\{1,2\}}^{(n)}\text{tree}} = \sqrt{m_u^2 + \frac{n^2}{R^2}}, \quad (4.52)$$

which is the same as the bosonic combination of zero-mode mass and KK mass.

4.5.3 Diagonalising the bosons

For full details of the diagonalisation of the bosonic sector see our paper [3]. An important point to note is that the electroweak W^3 and B bosons mix due to EWSB. This is analogous to the mixing of the SM W^3 and B to form the Z boson and the photon mass eigenstates, where the mixing angle is θ_W , defined in Equation 2.29. The procedure is the same for the zero mode in MUED, but at $n \geq 1$ the mixing angle is substantially different, and so we call the mass eigenstates $P^{(n)}$ and $V^{(n)}$ (in place of A and Z respectively) to highlight that they behave differently to their SM relatives. The $P^{(n)}$ states

are almost completely made up of KK modes of the B boson, with a small admixture of W^3 : this is due to the large hierarchy between the electroweak and compactification scales. The masses for these two states are given by

$$(m_{P,V}^2)^{(n)} = \frac{1}{2} \left[\frac{v^2}{4} (g^2 + g'^2) + \frac{n^2}{R^2} (Z_B + Z_W) \right. \\ \left. \mp \sqrt{\left(\frac{v^2}{4} (g^2 - g'^2) + \frac{n^2}{R^2} (Z_W - Z_B) \right)^2 + \frac{1}{4} g'^2 g^2 v^4} \right]. \quad (4.53)$$

The charged W bosons behave comparatively simply, with the KK masses being given by

$$(m_W^{(n)})^2 = m_W^2 + Z_W^2 \left(\frac{n}{R} \right)^2. \quad (4.54)$$

The scalar sector is more complicated. Before symmetry breaking we have KK modes of the fifth components of the vector fields B_5 , W_5^\pm , W_5^3 , and the charged, neutral scalar and neutral pseudoscalar components of the Higgs field, χ^\pm , H and χ^0 , respectively (see Equation 2.24). Particles with identical electric charges mix to form a charged and neutral Goldstone boson (to be eaten by the massive vector fields), a physical charged scalar $a^\pm^{(n)}$, a neutral scalar $H^{(n)}$ (morally the KK partner of the SM Higgs) and a neutral pseudoscalar $a^0^{(n)}$. The masses of these physical mass eigenstates are

$$(m_{a^\pm}^{(n)})^2 = \frac{Z_H}{Z_W} (m_W^{(n)})^2 \quad (4.55)$$

$$(m_H^{(n)})^2 = m_H^2 + Z_H \left(\frac{n}{R} \right)^2 \quad (4.56)$$

$$(m_{a^0}^{(n)})^2 = Z_H \left[\left(\frac{n}{R} \right)^2 + \frac{v^2}{4} \left(\frac{g'^2}{Z_B} + \frac{g^2}{Z_W} \right) \right]. \quad (4.57)$$

The gluon sector avoids all of the complications of EW mixing. The KK gluons simply have the masses

$$(m_G^{(n)})^2 = Z_G \left(\frac{n}{R} \right)^2 \quad (4.58)$$

and the KK modes of G_5 are Goldstone bosons that are eaten by the related KK gluons.

4.5.4 Implementation details

Using the ‘‘wavefunction renormalisation’’ prescription of including the orbifold radiative corrections, we implemented the 5D Lagrangian in LanHEP. In LanHEP, one is able to specify the KK decomposition of the 5D fields and how the KK modes mix to form the mass eigenstates. Once this is done, LanHEP can integrate out the extra dimension and automatically derive the Feynman rules for the mass eigenstates.

In practical calculations, one must truncate the KK expansion at some finite KK number. Such a truncation breaks gauge invariance: this is because a general gauge transformation can transform a KK mode into a linear combination of infinitely many KK modes, which is not compatible with a truncation. This is analogous, for example, to the breaking of gauge symmetry that occurs when one imposes a UV cutoff in QED. This breaking of gauge invariance in MUED would manifest itself at the level of the Feynman rules as a dependence of physical amplitudes on the value of the gauge fixing parameter introduced during the Fadeev-Popov gauge fixing procedure. Such gauge fixing parameter-dependence will disappear as the KK number cutoff is raised to infinity.

This violation of gauge invariance is not as problematic as it might first appear, however. Because KK number is conserved at all tree-level vertices, and because CalcHEP only deals with Feynman diagrams at tree level, as long as the number of external particles is kept below some threshold, the amplitudes remain gauge fixing parameter-invariant. The general condition for gauge invariance is that if the highest KK number of any particle in the model is n_{\max} then the simple sum of the KK numbers of the external particles must not exceed $2n_{\max} + 1$. In the MUED model we made publicly available, $n_{\max} = 2$, so processes where the KK numbers of the external particles sum to less than or equal to 5 will have gauge invariant (tree-level) amplitudes. For instance, if one considered the collision of two SM particles, there could be four $n = 1$ particles and a Standard Model particle in the final state, without introducing gauge fixing parameter dependence. A model with $n_{\max} = 4$ is also available upon request, but the extra particle content slows the compilation of the LanHEP file significantly.

One further important detail to note is that in the previously-existing CalcHEP model of MUED by Datta, Kong and Matchev [46] (what we call the DKM model), the gluon self-interaction vertices were implemented incorrectly. CalcHEP cannot deal with four-gluon vertices directly, so one must manually “split” them into three-particles vertices involving two gluons and a vector or second-rank tensor auxiliary field. Details of this, and also the general (though, for our purposes, unnecessarily complex) method for correctly arranging the splitting using Lagrange multipliers can be found in [49]. The gluon vertex splitting for the SM gluons in the DKM model was correctly implemented, but for higher KK modes the correct four-gluon vertices are not reconstructed. The correct splitting of the KK gluon vertices can be found in our paper [3] along with details of the model implementation and numerical comparison with the DKM model. I reproduce a selection of the results in the next three sections.

4.6 Mass spectrum and decay modes

Radiative corrections are vital to determining even the qualitative structure of the particle spectrum. They also dictate which decay modes are kinematically allowed, and the

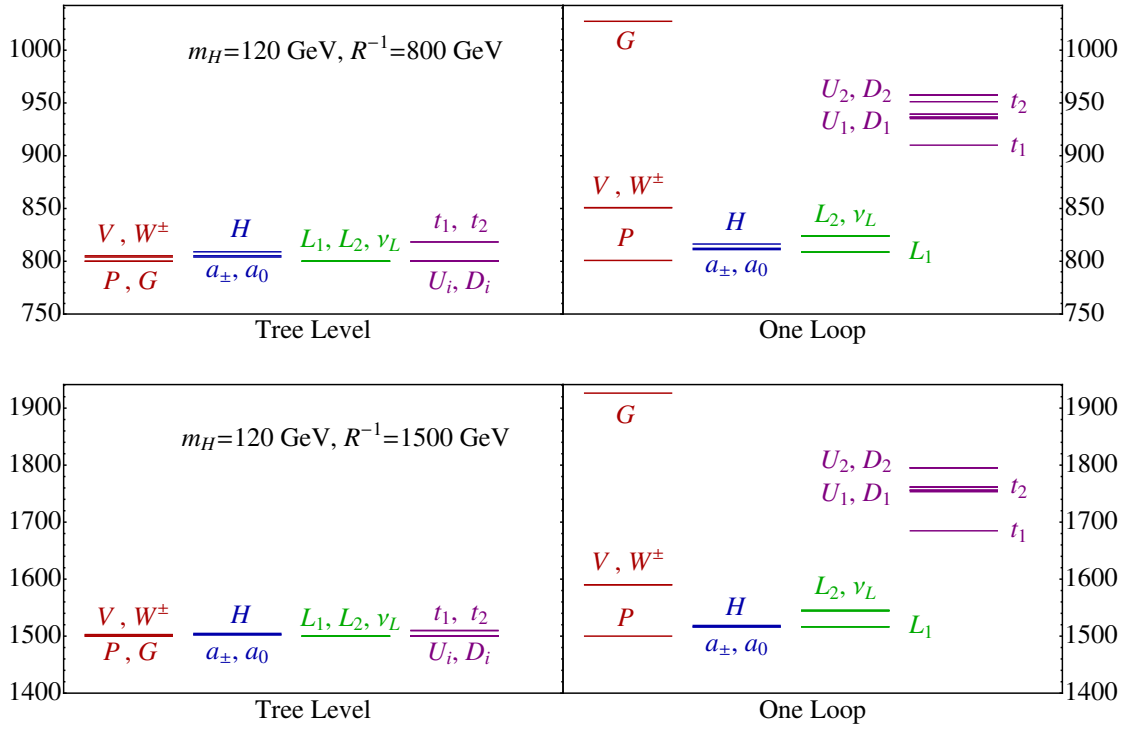


Figure 4.3: Mass spectrum of MUED at tree level (left) and one-loop level (right) for $R^{-1} = 800$ GeV (top) and $R^{-1} = 1500$ GeV (bottom). The vertical axis shows the particle masses in units of GeV.

relative branching ratios of these modes. Having MUED implemented in CalcHEP (via LanHEP) makes exploring the mass spectrum and its implications much quicker than investigating by hand.

There are two free parameters of MUED: the UV cutoff Λ and the compactification scale R^{-1} . In fact, because cutoff scale is generally taken to be significantly higher than the energy of the process being considered (otherwise, the validity of the effective field theory approach breaks down), predictions at electroweak scales are typically only weakly dependent on Λ . We set $\Lambda = 20R^{-1}$ to be compatible with the value used in other literature. When fixing R^{-1} , we choose the two benchmark values $R^{-1} = 800$ GeV and $R^{-1} = 1500$ GeV.

Figure 4.3 shows the mass spectrum of the $n = 1$ particles in MUED (suppressing the KK number on the plots). The masses are shown in units of GeV, with and without one-loop radiative mass corrections, for $R^{-1} = 800$ GeV and $R^{-1} = 1500$ GeV. We worked on this project before the discovery of the Higgs boson at 125 GeV, so the mass was set to the then best estimate of 120 GeV.

It can be seen that the degeneracy seen at tree level is dramatically lifted by the loop corrections. All corrections are positive, and the coloured particles receive the largest corrections due to the size of the strong coupling. The gluon changes from being the

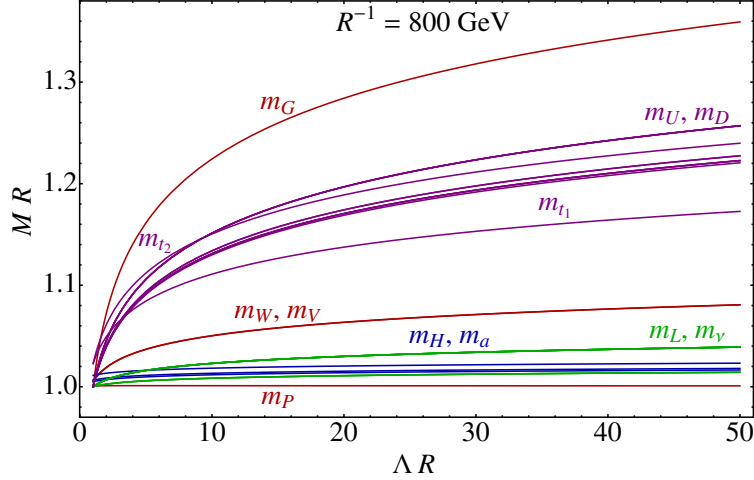


Figure 4.4: Variation of the $n = 1$ particle masses as a function of Λ , both quantities given in units of the compactification scale, fixed at $R^{-1} = 800$ GeV.

joint-lightest particle at tree level to the heaviest at one-loop level. For the benchmarks considered in these plots, it is clear that the LKP is $P^{(1)}$, an admixture of the $n = 1$ KK modes of the W^3 and the B bosons. The B contributes about 99%, due to the big difference between the electroweak and the compactification scale. For both benchmarks, the next-to-lightest KK particle (NLKP) is the lightest $n = 1$ charged lepton (an admixture of KK modes of E_L and E_R , dominated by U_R due, again, to the hierarchy of the EW and compactification scales). In the $R^{-1} = 1500$ GeV benchmark, the neutral scalar $a_0^{(n)}$ is almost degenerate with the NLKP.

With the model implementation, one can also quickly study the dependence of the masses on the cutoff scale (fixed in the previous plots at $\Lambda = 20R^{-1}$). This dependence for the $n = 1$ particles of the masses (given in units of the compactification scale) is shown in Figure 4.4 for the 800 GeV benchmark.

The orbifold corrections are proportional to the appropriate gauge couplings. Because of this, the mass of the gluon (dependent on the strong coupling g_s) varies by almost 40% over the range shown whereas the mass of the LKP (dominated by B , and therefore dependent on the g' coupling) hardly varies at all. There are some crossings in the running of the masses, meaning that there will be some values of the cutoff for which decays are forbidden and others for which they will be allowed.

The dependence of the masses $\times R$ on the compactification scale R^{-1} for a fixed ratio Λ/μ , where μ is the renormalisation scale, is shown in Figure 4.5. For large values of R^{-1} , the masses have a simple $1/R$ -dependence as per Equations (4.27), (4.28) and (4.29). This is because the (R -independent) electroweak contributions become negligible with respect to the radiative corrections. For lower values of the compactification scale, comparable to the EW scale, the departure from simple $1/R$ dependence become clearer, and some crossing in the ordering of the KK masses occurs.

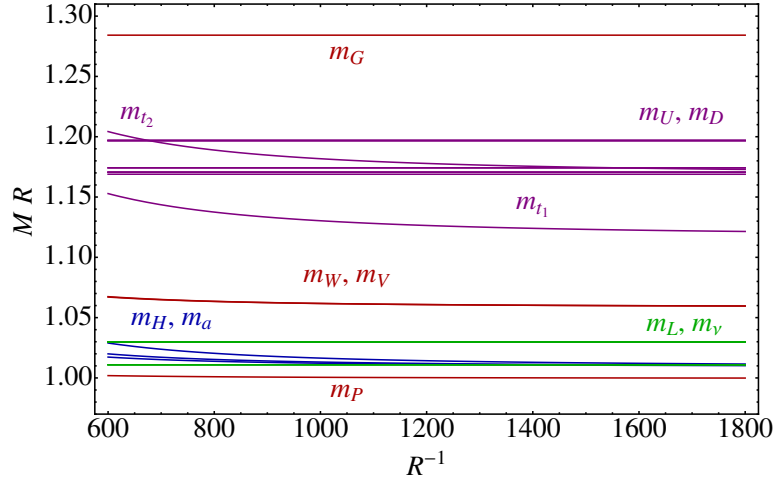


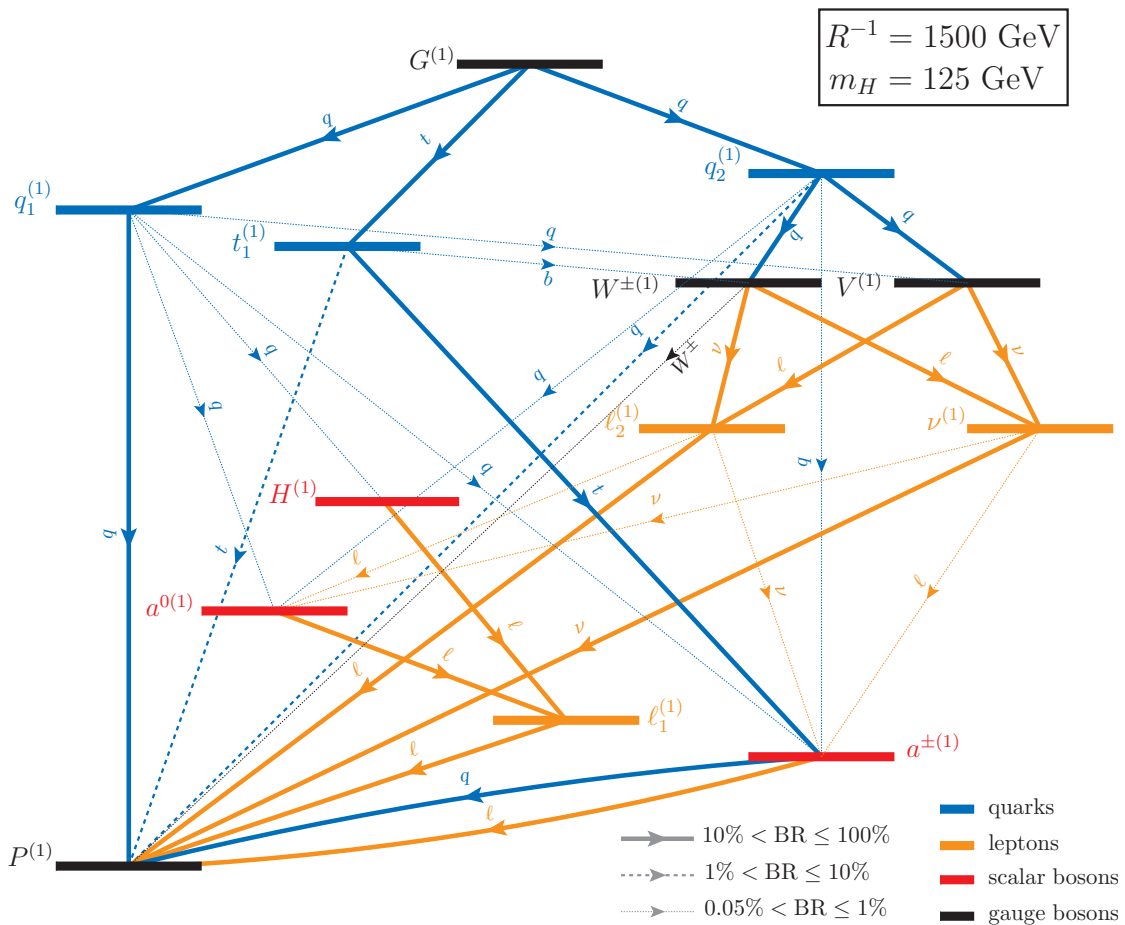
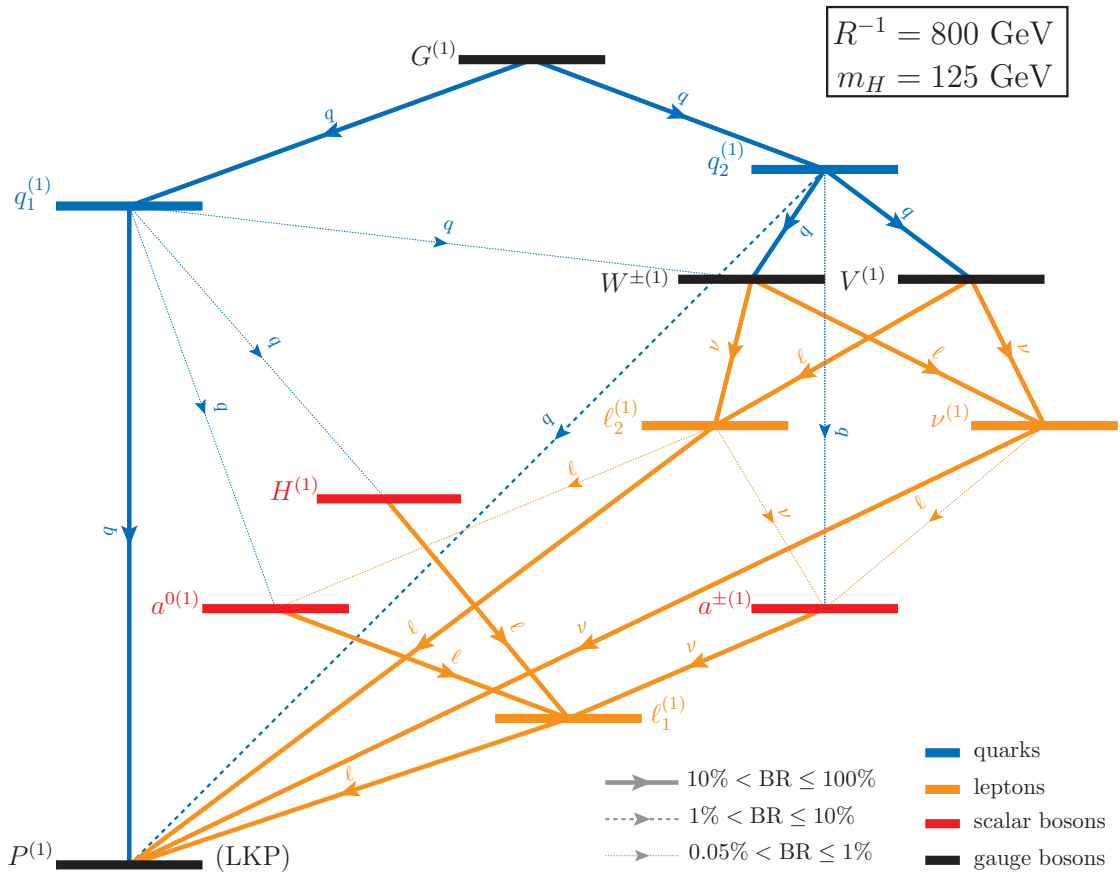
Figure 4.5: Variation of the $n = 1$ particle masses as a function of R^{-1} for $\Lambda/\mu = 20$, where μ is the renormalisation scale.

From the mass spectrum, one can determine which decays are kinematically allowed although, for an accurate calculation of the branching ratios, one requires the details of the dynamics. Again, the software implementation makes this relatively straightforward. As an example, in Figure 4.6 I plot decay chain diagrams for the $n = 1$ gluon, showing all significant decays. All the decays considered are two-body decays, where one of the decay products is an $n = 1$ particle, and the other must be a SM particle (labelled on the arrows) due to KK parity conservation. The decay chains for the two benchmark points $R^{-1} = 800$ GeV and $R^{-1} = 1500$ GeV show different behaviour. Most obviously, the large number and strength of the leptonic decays (shown by the preponderance of yellow in the plots) contrasts significantly to other BSM models, such as supersymmetry (SUSY). On reason for this dominance of lepton decays is due to mass hierarchy

$$m_{q_{1,2}^{(1)}} > m_{W^{(1)}}, m_{V^{(1)}} > m_{\ell_{1,2}^{(1)}}, m_{\nu^{(1)}} \quad (4.59)$$

that is typical in MUED. To achieve the analogous hierarchy in SUSY would require a special, non-universal mass pattern at the unification scale that is not generally realised in well-known SUSY GUT theories [50]. The decay $W^{\pm(1)} \rightarrow W^* P^{(1)}$ is also dynamically possible, and SM W would decay predominantly to quarks. However, the mass gap in MUED between $W^{(1)}$ and $P^{(1)}$ is typically small (cf. Figure 4.5) and so the SM W is off mass shell, suppressing the rate. If one increases the compactification scale to around 1.5 TeV, the real decay channel opens, but this is close to the edge of the allowed parameter space ($R^{-1} < 1.6$ TeV by Dark Matter considerations).

Another interesting feature is that then R^{-1} is increased, the decay chain $G^{(1)} \rightarrow tt_1^{(1)} \rightarrow tta^{\pm(1)} \rightarrow tt(\ell \text{ or } q)P^{(1)}$ becomes kinematically allowed. Bearing in mind that KK gluons can be pair-produced at the LHC, this would lead to a striking signature of four top quarks. Similarly, because leptonic decays are common, lepton multiplicity in the final

Figure 4.6: Decay chains for the first KK gluon for two R^{-1} benchmarks.

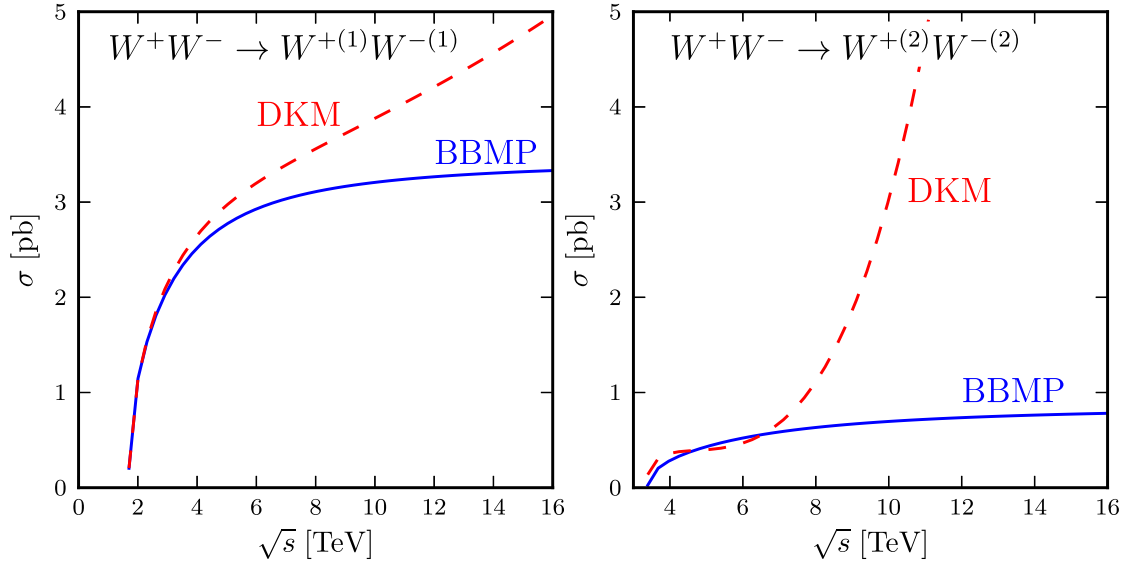


Figure 4.7: Comparison of the unitary behaviour of the cross-section for scattering of SM W bosons to KK $W^{(n)}$ bosons for $n = 1$ (left) and $n = 2$ (right) in our model (BBMP, shown with a blue solid line) and the model described in [46] (DKM, shown with a red dashed line).

states at the LHC could easily reach four, and possible *eight*, although the latter could only proceed via extremely rare decays involving the $a^{0(1)}$ scalar boson.

4.7 Unitarity of WW scattering

One important limitation of the DKM model implementation described in [46] is that it does not contain the KK Higgs spectrum. A consequence of this is that the scattering of KK W bosons would grow without limit, eventually violating unitarity. In Figure 4.7 I plot the $WW \rightarrow W^{(n)}W^{(n)}$ scattering cross-section for $n = 1$ (left) and $n = 2$ (right), comparing the behaviour predicted by our model (BBMP, shown with solid blue lines) to that predicted by the DKM model (dashed red lines). The troublesome behaviour clearly seen in the DKM model is clearly avoided in our model, as expected: the extra KK Higgs particles unitarise the cross-section in the same way at the SM Higgs unitarises SM WW scattering.

4.8 Discovering MUED at the LHC: the tri-lepton signature

With a consistent, gauge invariant CalcHEP implementation of MUED with phenomenologically important radiative mass corrections, we were able to investigate the collider

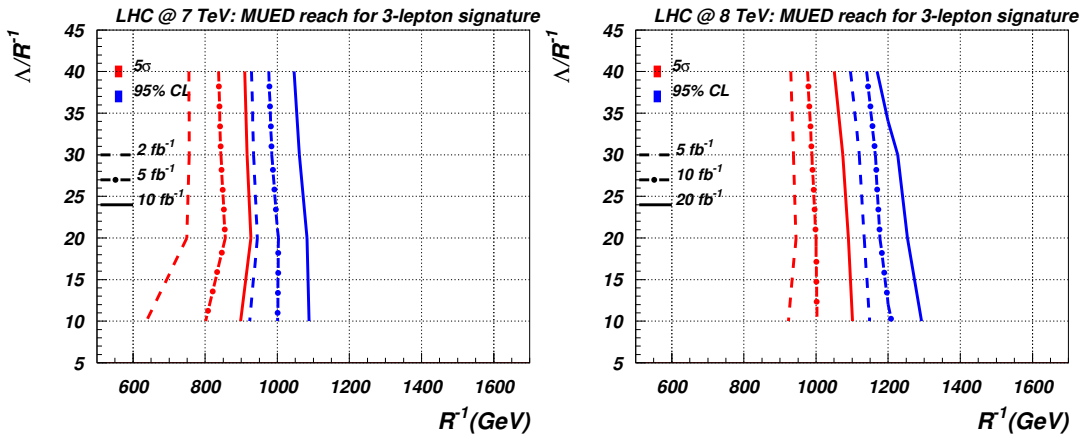


Figure 4.8: Exclusion (red) and discovery (blue) potential for MUED for different luminosities for the LHC with an energy of 7 TeV (left) and 8 TeV.

phenomenology of the model. The unusually large lepton multiplicity of typical decay events in MUED led us to investigate multi-lepton final states as possible signatures for MUED, ultimately discovering that the tri-lepton signature provided the most powerful search strategy for discovering MUED at the LHC.

The full details are presented in our paper [3] and I present the main result in Figure 4.8. In these plots, points in the parameter space to the left of the blue and red contours can be excluded at the 95% confidence level or discovered at the canonical 5σ level respectively. So with 20 fb^{-1} of data collected by the 8 TeV LHC, one could discover MUED with values of R^{-1} up to 1050 GeV and exclude the theory for $R^{-1} \lesssim 1200 \text{ GeV}$.

4.9 Constraining MUED using LHC Higgs boson searches

In this section I describe a project I worked on in collaboration with the authors listed in [2]. The goal of this project was to use the results from Higgs searches at the LHC to constrain the parameter space of MUED. To do this, I made use of a CalcHEP model of MUED developed by Mitsuru Kakizaki, and extended this model by adding effective vertices to represent the one-loop $gg \rightarrow H$ and $H \rightarrow \gamma\gamma$ amplitudes.

Around the time of our analysis, work had been done in a similar vein [51]. Our analysis went further by considering the effects of the radiative corrections to the masses of the KK particles running in the loops mentioned in the last paragraph. We also used the experimental data in a more sophisticated way, statistically combining exclusions from different channels to provide a more accurate exclusion limit on the MUED parameter space.

The first subsection below describes how we calculated the gluon fusion production and diphoton decay amplitudes in MUED, including the radiative mass corrections discussed in Section 4.5.1. Then in Section 4.9.2 I calculate the cross-section enhancement in several channels for comparison with experimental data. In Section 4.9.3 I present the statistical procedure used to constrain the parameter space using the LHC Higgs search data and I present then I present the results in Section 4.9.4.

4.9.1 Evaluation of amplitudes for Higgs production and decay in MUED

As discussed in Section 3.2, in the SM the dominant process for producing the Higgs boson at the LHC is gluon-gluon fusion, despite the leading order contribution being a one-loop process. In MUED, KK quarks can also run in the triangle loop leading to an enhancement over the SM amplitude.

For the intermediate values of the Higgs mass (around 100–200 GeV), the most powerful Higgs search channel is into two photons. Indeed the low QCD background for this process compensates for the fact that the Higgs decay width into two-photons only proceeds at the one-loop level and is thus suppressed. In the SM the dominant contribution to the two-photon width comes from loops involving W^\pm bosons. This contribution is about four times larger than the one from fermions. Furthermore, the charged fermion triangle loop (again, dominated by top quarks) interferes destructively with the W^\pm contribution.

In MUED, new contributions arise from KK W 's and KK fermions running in loops. The contributions of the KK W 's and KK fermions have the same sign as their SM counterparts, but the increase as compared to the SM contribution is larger for fermions than for W 's. First, associated with each SM fermion there are two towers of KK fermions while there is only one for W^\pm . Second, the contributions of particles from higher KK levels decrease more slowly for fermions than for W 's, as we will see in the next section. Furthermore, for KK number $n \geq 1$, there is an additional contribution from charged scalars $a^{\pm(n)}$. This latter field is a mixture of the KK modes of the 5th component of the charged vector field W_M and the charged component of the Higgs field Φ . At each KK level, the charged scalar contributes with the *same* sign as the fermion diagrams, despite the opposite statistics. The net effect is therefore to suppress the Higgs to diphoton decay rate relative to the SM prediction. The three (fermion, W^\pm and $a^{\pm(n)}$) contributions are shown in Figure 3.6. Additional diagrams involving W^\pm Goldstones and ghosts are presented in Appendix A.3.

In the following subsections I show the results of calculating the amplitude for production of a SM Higgs boson from gluon-gluon fusion, and also the amplitude for subsequent decay to two photons. The amplitudes \mathcal{A} for the $gg \rightarrow H$ and $H \rightarrow \gamma\gamma$ processes both

take the form

$$\mathcal{A} = \tilde{\mathcal{A}} [(p \cdot q)(\epsilon \cdot \eta) - (p \cdot \eta)(q \cdot \epsilon)], \quad (4.60)$$

where the Higgs is allowed to be off-shell, as previously described in Equation 3.31. To calculate the exact amplitude for $gg \rightarrow H \rightarrow \gamma\gamma$, one would combine the separate off-shell amplitudes for $gg \rightarrow H$ and $H \rightarrow \gamma\gamma$ with a Higgs propagator. However, in this analysis I use the “narrow width approximation” (valid when the Higgs boson’s width is much less than its mass, as described in Section 3.1) which allows us to write the $gg \rightarrow H \rightarrow \gamma\gamma$ cross section as the product of the cross-section for production of an on-shell Higgs boson and the branching ratio of an on-shell Higgs to two photons, i.e.

$$\sigma(gg \rightarrow H \rightarrow \gamma\gamma) \approx \sigma(gg \rightarrow H) \times \text{BR}(H \rightarrow \gamma\gamma). \quad (4.61)$$

In this approximation, we only need amplitudes involving on-shell Higgs bosons, so we can write Equation 3.31 as in Equation 3.32, reproduced here:

$$\mathcal{A} = \tilde{\mathcal{A}} \left[\frac{m_H^2}{2} (\epsilon \cdot \eta) - (p \cdot \eta)(q \cdot \epsilon) \right]. \quad (4.62)$$

These amplitudes have been calculated previously in the SM case in the $m_H/M \ll 1$ limit [52] (where M is the mass of the particle flowing in the loop) and subsequently [53] for general m_H/M .

They have also been calculated in the MUED case (without radiative mass corrections) in [54]. I performed the calculation in the general case and specialised to MUED, including radiative corrections to the KK masses. I used the ‘t Hooft-Feynman gauge and regulated the divergences that appear in intermediate steps using dimensional regularisation. The calculation made use of the well-known Passarino-Veltman functions [55] to evaluate the momentum integrals and is shown in detail with all contributing diagrams in Appendices A.2 and A.3. The results reduce to the SM result found in the literature [23] when the KK modes are removed, and agree with the result in [54] when tree-level KK masses are used in MUED.

Higgs production

The amplitude for $gg \rightarrow H$ (Figure 3.6) reads²

$$\tilde{\mathcal{A}}_{ggH} = -\frac{\alpha_s}{4\pi v} \left(F_{ggH}^{\text{SM}} + \sum_{n=1}^N F_{ggH}^{(n)} \right). \quad (4.63)$$

where $\alpha_s = g_s^2/(4\pi)$ is the strong coupling constant and $v = 2 \sin \theta_W m_W / e$ is the Higgs vacuum expectation value (θ_W is the Weinberg angle, e is the elementary electric charge and m_W is the mass of the W boson). In the SM there would be contributions from each quark flavour q in the loop, such that $F_{ggH}^{\text{SM}} = \sum_q F_{1/2}(\tau_q)$ where the standard fermion contribution is given by Equation 3.37a. Note that $F_{1/2}$ is a dimensionless function and the loop particle mass m always appears in the dimensionless combination $\tau = 4m^2/m_H^2$.

In the $\tau \rightarrow \infty$ (i.e. $m \gg m_H$) limit, the above expressions reduce to $f(\tau) = \frac{1}{\tau} + \frac{1}{3\tau^2} + \mathcal{O}(1/\tau^3)$ and

$$F_{1/2}(\tau) \approx \frac{4}{3} + \frac{2}{3\tau} + \mathcal{O}(1/\tau^2) \rightarrow 4/3. \quad (4.64)$$

Thus the amplitude tends to a constant in the heavy quark limit. This is however not the case when KK quarks are included in the loop: the heavy KK quarks “decouple”. The reason for this is that in contrast with SM fermions, while a KK particle’s mass increases with KK number, there is *no* corresponding increase in its Yukawa couplings and so decoupling does occur because of suppression from the propagators. This decoupling behaviour is shown explicitly below.

In MUED, the contribution from KK quarks at the n th KK level (there are two KK quarks at each level for each SM quark q) is

$$F_{ggH}^{(n)} = \sum_q \sin(2\alpha_q^{(n)}) \left(\frac{m_q}{m_{q,1}^{(n)}} F_{1/2}(\tau_{q,1}^{(n)}) + \frac{m_q}{m_{q,2}^{(n)}} F_{1/2}(\tau_{q,2}^{(n)}) \right). \quad (4.65)$$

where $m_{q,1}^{(n)}$ and $m_{q,2}^{(n)}$ denote the KK quark masses, $\alpha_q^{(n)}$ denote the mixing angles required to diagonalise the KK quark mass matrices, and $\tau_{q,i}^{(n)} \equiv (2m_{q,i}^{(n)}/m_H)^2$. As an example, in the case where $q = u$, the masses are given in Equation 4.49), and the mixing angle in Equation 4.47. At tree level, all KK quark masses are nearly degenerate,

$$m_{q,\text{tree}}^{(n)} = \sqrt{m_q^2 + \frac{n^2}{R^2}}, \quad (4.66)$$

²It should be noted that higher loop corrections to the $gg \rightarrow H$ amplitude can be substantial, reaching as much as 90% of the one-loop amplitude [56]. However, these large corrections are dominated by SM contributions (KK contributions are suppressed by powers of the compactification scale R^{-1}). The SM QCD corrections depend only on spin of the particle in the large mass limit and therefore they are universal for SM and MUED. For our purposes, all that is important is the ratio of MUED and SM rates, and so the QCD corrections cancel to a good approximation and therefore the results are valid for higher order QCD corrections.

where m_q is the zero mode mass, and the mixing angles are

$$\alpha_{q,\text{tree}}^{(n)} = \frac{1}{2} \arctan \left(\frac{m_q R}{n} \right) \quad (4.67)$$

(so $\sin(2\alpha_{q,\text{tree}}^{(n)}) = m_q/m_{q,\text{tree}}^{(n)}$).

In the full analysis presented shortly, one-loop corrected expressions for all masses and mixings are used, but it is illustrative to neglect loop corrections and study the behaviour (just considering the top-quark contribution, which is dominant) for that case that $m_{t,\text{tree}}^{(n)} > m_t > m_H$:

$$F_{ggH}^{(n)} \approx 2 \left(\frac{m_t}{m_{t,\text{tree}}^{(n)}} \right)^2 F_{1/2}(\tau_{t,\text{tree}}^{(n)}) \approx 2 \left(\frac{m_t}{m_{t,\text{tree}}^{(n)}} \right)^2 \times \frac{4}{3}, \quad (4.68)$$

throwing away terms in m_H/m_t and $m_t R$ of order 3 or higher. This demonstrates the fact, mentioned above, that (in contrast to SM quarks) heavy KK quarks decouple from the process.

Taking the mass of the n th KK quark to be approximately n/R and considering just the top quark, the total KK contribution to the amplitude is approximately

$$F_{ggH}^{\text{KK}} \equiv \sum_{n=1}^N F_{ggH}^{(n)} \approx 2 \times \frac{4}{3} m_t^2 R^2 \sum_{n=1}^N \frac{1}{n^2}. \quad (4.69)$$

The sum is convergent as $N \rightarrow \infty$, thanks to the decoupling of the heavy KK particles. In this limit, $F_{ggH}^{\text{KK}} \rightarrow 4(\pi m_t R)^2/9$. So the momentum cutoff uncertainty is quite mild if one chooses a reasonably large value for it.

The sum over KK modes n is taken up to a cutoff N , corresponding to a momentum cutoff in the extra dimension of NR^{-1} . Mild cutoff-dependence is expected in perturbatively nonrenormalisable theories such as MUED. In our quantitative analysis we chose $N = 20$ and included only t and b in the sum over quark flavours q , which is an excellent approximation due to the size of their Yukawa couplings compared to those of the lighter quarks. One should note that for large N the rest of the sum is proportional to $1/N$. Therefore, for $N = 20$ our result is given with about 5% accuracy as compared to the full sum.

Higgs decay to two photons

The $H \rightarrow \gamma\gamma$ amplitude is given by

$$\tilde{\mathcal{A}}_{H\gamma\gamma} = -\frac{\alpha}{2\pi v} F_{H\gamma\gamma}, \quad (4.70)$$

where $\alpha = e^2/(4\pi)$ is the fine structure constant, v is the Higgs vacuum expectation value (defined just below Equation 4.63), and

$$F_{H\gamma\gamma} = F_{H\gamma\gamma}^{\text{SM}} + \sum_{n=1}^N F_{H\gamma\gamma}^{(n)} \quad (4.71)$$

The SM part consists of a contribution from the W^\pm vector bosons and fermions:

$$F_{H\gamma\gamma}^{\text{SM}} = F_1(\tau_W) + \sum_f n_c Q_f^2 F_{1/2}(\tau_f). \quad (4.72)$$

The sum is taken over all SM fermions f , each with charge $Q_f e$, setting n_c to 3 for quarks and 1 for leptons. The fermion loop function $F_{1/2}$ is the same as for the $gg \rightarrow H$ case, given in Equation 3.37a, and the vector function F_1 (representing the W^\pm and related Goldstone and ghost contributions) was given by Equation 3.37b. In the $\tau \rightarrow \infty$ large loop mass limit, this tends to a constant

$$F_1(\tau) \approx -7 - \frac{2}{\tau} + \mathcal{O}(1/\tau^2) \rightarrow -7, \quad (4.73)$$

showing that particles whose masses are proportional to their Yukawa couplings do not decouple from the process, just as we saw in Equation 4.64 for the production amplitude.

At the n th KK level, the amplitude receives contributions from KK charged fermions (two KK partners for each SM fermion) and the KK W_n^\pm vector boson. There is also a contribution from the charged scalar $a^{\pm(n)}$ that is not present at the SM level, so

$$F_{H\gamma\gamma}^{(n)} = F_{1/2}^{(n)} + F_1^{(n)} + F_0^{(n)}. \quad (4.74)$$

The fermion contribution is the same as the quark contribution Equation 4.65 was for the Higgs production amplitude, up to colour and charge factors:

$$F_{1/2}^{(n)} = \sum_f n_c Q_f^2 \sin(2\alpha_f^{(n)}) \left(\frac{m_f}{m_{f,1}^{(n)}} F_{1/2}(\tau_{f,1}^{(n)}) + \frac{m_f}{m_{f,2}^{(n)}} F_{1/2}(\tau_{f,2}^{(n)}) \right). \quad (4.75)$$

and so has a similar asymptotic behaviour to the one shown in Equation 4.68. The sum over KK modes is therefore convergent as well.

The vector contribution is given in terms of the SM expression as follows and also decouples as $m_{W,n} \rightarrow \infty$, in contrast to the SM case:

$$F_1^{(n)} = \left(\frac{m_W}{m_W^{(n)}} \right)^2 F_1(\tau_W^{(n)}) \approx -7 \left(\frac{m_W}{m_W^{(n)}} \right)^2 + \mathcal{O} \left(m_W/m_W^{(n)} \right)^4 \rightarrow 0. \quad (4.76)$$

The scalar contribution is given by

$$F_0^{(n)}(m_a^{(n)}, m_W^{(n)}) = \left[2 \left(\frac{m_W}{m_a^{(n)}} \right)^2 \left(1 - \left(\frac{2m_a^{(n)}}{m_H} \right)^2 \right) - 2 \right] \left[1 - \left(\frac{2m_a^{(n)}}{m_H} \right)^2 f(\tau_a^{(n)}) \right]. \quad (4.77)$$

At tree-level, $m_a^{(n)} = m_W^{(n)}$ so, keeping m_W and m_H constant, as we increase the KK scalar's mass,

$$F_0^{(n)} \approx \left(\frac{m_W}{m_a^{(n)}} \right)^2 \left(\frac{1}{3} + \frac{m_H^2}{6m_W^2} \right) + \mathcal{O}(m_W/m_a^{(n)})^4 \rightarrow 0, \quad (4.78)$$

again demonstrating decoupling behaviour in the large KK mass limit.

In the SM case we can use the limits when the mass of the particle flowing in the loop is large compared to the Higgs mass to estimate the relative contributions from fermions and vectors, noting that they have opposite signs. Including the charge and colour factors for the fermion case and considering only the top quark, the ratio is $|F_1|/|N_c Q_t^2 F_{1/2}| \approx 7/\frac{16}{9} \approx 3.9$. Following the same procedure for contributions from level n KK particles (taking their masses to be approximately n/R) we find this ratio to be smaller, recognising that there are *two* KK top quarks: $|F_1^{(n)}|/|F_{1/2}^{(n)}| \approx 3.9(m_W^2/2m_t^2) \approx 0.42$, i.e. less than 1. This suggests that the KK particles interfere with the SM contribution destructively, reducing the overall amplitude. In addition, there is the charged scalar contribution which has the same sign as the fermion contribution, reducing the amplitude further. This indication of amplitude suppression is confirmed by the full calculation.

The dependence of the two amplitudes Equation 4.63 and Equation 4.70 on the two free parameters of MUED – m_H and the inverse compactification radius R^{-1} – is shown in Figure 4.9. This clearly indicates that for a light Higgs the ggH coupling is enhanced while $H\gamma\gamma$ is suppressed as argued above. The R^{-1} dependence enters through the KK masses and mixing angles. I calculated the amplitudes using tree-level KK masses (dashed lines) and loop-corrected values (solid lines).

4.9.2 Calculating the MUED cross-section enhancement

In order to constrain MUED using SM Higgs boson searches at the LHC, we first need to calculate the enhancement of cross-sections of Higgs production and subsequent decay in different channels. Here we consider the three most important channels in the low Higgs mass range: $gg \rightarrow H \rightarrow \gamma\gamma$, $gg \rightarrow H \rightarrow W^+W^- \rightarrow \bar{\ell}\nu\ell\bar{\nu}$ and $gg \rightarrow H \rightarrow ZZ \rightarrow 2\bar{\ell}2\ell$. We can work in the narrow width approximation $\Gamma_H \ll m_H$, assuming that the Higgs is produced approximately on-shell and subsequently decays with some branching ratio

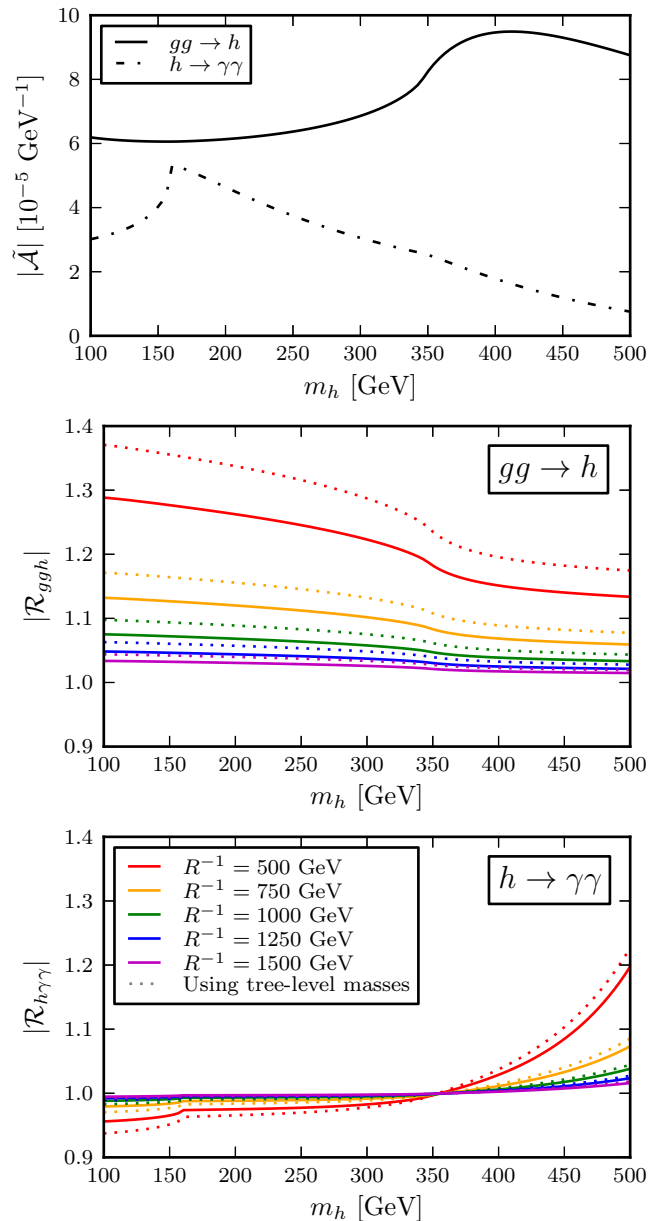


Figure 4.9: Behaviour of the SM amplitudes and the relative sizes of the corresponding MUED amplitudes for several values of R^{-1} . The top figure shows the behaviour of the absolute values of the SM amplitudes for Higgs production and decay to two photons respectively. The bottom figures show the enhancement of these amplitudes in MUED relative to the SM, where $\mathcal{R} = \mathcal{A}_{\text{UED}}/\mathcal{A}_{\text{SM}}$. For the MUED plots, from top to bottom on the RHS of each plot: $R^{-1} = 500, 750, 1000, 1250$ and 1500 GeV. Solid lines show the results when using loop-corrected KK masses and dashed lines show tree-level results.

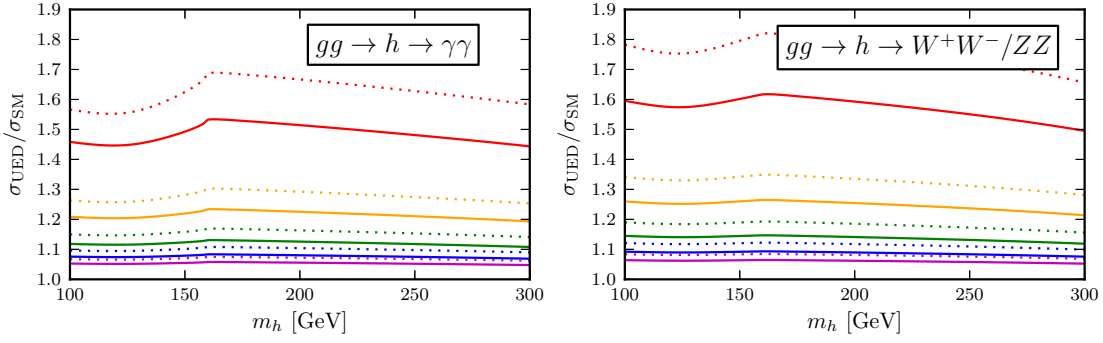


Figure 4.10: Enhancement of MUED cross-sections in $\gamma\gamma$ (left) and W^+W^-/ZZ (right) channels relative to the SM. The graphs show variation with m_H for the following values of R^{-1} : from top to bottom on the RHS of each plot, $R^{-1} = 500, 750, 1000, 1250$ and 1500 GeV. Solid lines show results when using loop-corrected masses in the loops, while dashed lines correspond to tree-level masses.

BR, so that

$$\sigma(xx \rightarrow H \rightarrow yy) = \sigma(xx \rightarrow H) \times \text{BR}(H \rightarrow yy). \quad (4.79)$$

In fact, since we need only the enhancement of each signal cross-section relative to the SM, knowledge of the full hadronic cross-section is not required because the integrals of parton density functions would be the same in MUED and the SM and would cancel in the ratio. The ratio can then be written simply in terms of total and partial Higgs widths as

$$\mu_{\gamma\gamma} \equiv \frac{\sigma_{\text{MUED}}(gg \rightarrow H \rightarrow \gamma\gamma)}{\sigma_{\text{SM}}(gg \rightarrow H \rightarrow \gamma\gamma)} \approx \frac{\Gamma_{\text{MUED}}(H \rightarrow gg) \times \text{BR}_{\text{MUED}}(H \rightarrow \gamma\gamma)}{\Gamma_{\text{SM}}(H \rightarrow gg) \times \text{BR}_{\text{SM}}(H \rightarrow \gamma\gamma)} \quad (4.80)$$

for the diphoton channel and

$$\begin{aligned} \mu_{WW/ZZ} &\equiv \frac{\sigma_{\text{MUED}}(gg \rightarrow H \rightarrow WW)}{\sigma_{\text{SM}}(gg \rightarrow H \rightarrow WW)} \approx \frac{\Gamma_{\text{MUED}}(H \rightarrow gg) \times \text{BR}_{\text{MUED}}(H \rightarrow WW)}{\Gamma_{\text{SM}}(H \rightarrow gg) \times \text{BR}_{\text{SM}}(H \rightarrow WW)} \\ &\approx \frac{\Gamma_{\text{MUED}}(H \rightarrow gg) \times \Gamma_{\text{SM}}(H \rightarrow \text{all})}{\Gamma_{\text{SM}}(H \rightarrow gg) \times \Gamma_{\text{MUED}}(H \rightarrow \text{all})} \end{aligned} \quad (4.81)$$

for the W^+W^- and ZZ channels. Note that the MUED and SM expressions for the partial Higgs width to two vector bosons are the same, to leading order.

These two enhancement factors are plotted for various values of m_H and R^{-1} in Figure 4.10, also showing the effect of including loop corrected masses in the loop diagrams.

4.9.3 Constraining the parameter space

4.9.3.1 Using one channel

At the time of this project, the Higgs had yet to be discovered. Higgs searches were being performed in earnest and results were usually presented by ATLAS and CMS using combined “Brazil band” exclusion limit plots as described in Section 3.3.2. These plots can be applied to family of models related to the SM in the following way. As discussed, the pattern of fully-exclusive Higgs signal cross-sections ($\sigma(xx \rightarrow H \rightarrow yy)$) is the same as the Standard Model’s except that each of them is scaled by some uniform factor, often denoted by μ . The exclusion plots showed the value of this enhancement factor that is excluded at the 95% confidence level for each value of the Higgs mass. This quantity was normally written as $\mu^{95\%}$. When $\mu^{95\%}$ drops below unity, the SM is excluded at the 95% confidence level.

Although $\mu^{95\%}$ can be used to exclude models that have the same pattern of cross-sections as the SM, for models (such as MUED) where different channels receive different corrections from new physics, this combined $\mu^{95\%}$ is not a useful quantity. Fortunately, the collaborations also provided exclusion plots for separate channels. It is then a simple matter to compare the value of, say, $\mu_{\gamma\gamma}$ to the excluded value $\mu_{\gamma\gamma}^{95\%}$. The exclusions from each channel and each experiment can then be overlapped in a simple way to constrain the model. This has been done previously for MUED [51, 1]. However more accurate constraints on the model’s parameter space can be obtained with a more sophisticated method of combining the exclusions from different channels in a statistically rigorous way. Such a method is discussed in the next section.

4.9.3.2 Statistical combination

We want to reproduce as closely as possible the analysis used by the experimental collaborations to calculate $\mu^{95\%}$ for the SM Higgs, but within the framework of MUED. Let us start completely analogously by imagining a family of models, each exactly the same as MUED except that the Higgs signal cross-sections in each channel are all scaled by a common factor μ . So, for example, if MUED (for certain values of m_H and R^{-1}) predicts a $gg \rightarrow H \rightarrow \gamma\gamma$ cross-section of $\sigma_{\gamma\gamma}^{\text{MUED}}$, a $gg \rightarrow H \rightarrow WW \rightarrow \bar{\ell}\ell\nu\nu$ cross-section of $\sigma_{WW}^{\text{MUED}}$, and a $gg \rightarrow H \rightarrow ZZ \rightarrow \bar{2}\ell 2\ell$ cross-section of $\sigma_{ZZ}^{\text{MUED}}$, we imagine a family of related models predicting $\{\mu\sigma_{\gamma\gamma}^{\text{MUED}}, \mu\sigma_{WW}^{\text{MUED}}, \mu\sigma_{ZZ}^{\text{MUED}}\} = \{\mu\mu_{\gamma\gamma}\sigma_{\gamma\gamma}^{\text{SM}}, \mu\mu_{WW}\sigma_{WW}^{\text{SM}}, \mu\mu_{ZZ}\sigma_{ZZ}^{\text{SM}}\}$, writing the cross-sections in terms of the MUED enhancement factors defined in (4.80) and (4.81).

We then construct functions giving the probability of observing a particular numbers of events in each channel (the “individual likelihoods”, $p_i \equiv p(n_i^{\text{obs}}|\mu, \mu_i)$). These will

depend on the expected number of events in each channel i , given by

$$n_i = s_i + b_i = \mathcal{L}\varepsilon_i\mu\mu_i\sigma_i^{\text{SM}} + b_i.$$

Here, s_i and b_i denote the total number of signal and background events in channel i expected to be observed in the model defined by (m_H, R^{-1}, μ) . The integrated luminosity is given by \mathcal{L} and the signal cross-section can be written as $\mu\mu_i\sigma_i^{\text{SM}}$. Finally, it should be noted that the number of events one is able to see differs from the number of events that occur because of detector inefficiencies, particle misidentification and kinematical cuts. This is taken into account by the “efficiency” factor ε_i .

Once the individual likelihoods $p_i = p(n_i^{\text{obs}}|\mu, \mu_i)$ are known, the total joint likelihood $P(\{n_i^{\text{obs}}\}|\mu, \{\mu_i\}) = \prod_i p_i$ can be easily formed and then $\mu^{95\%}$ can be calculated.

The difficulty comes in reconstructing the likelihoods. At the time of this project, the experimental collaborations did not routinely make available the efficiency factors, exact number of observed events after cuts, or expected number of background events after cuts. What they *did* make available is the value of $\mu_i^{95\%}$ for many of the channels, and also the “expected” $\mu_{i,\text{expected}}^{95\%}$, which is the probability that the number of observed events might fluctuate down to the background-only expectation.

Azatov *et al* proposed [57] a method for approximately reconstructing the individual channel likelihoods from the data provided by the experimental collaborations and we followed their method, which I outline here.

It is possible to write the likelihood approximately as

$$p_i \propto \exp\left[-\frac{(n_i^{\text{obs}} - n_i)^2}{2n_i^{\text{obs}}}\right] \propto \exp\left[-\frac{(\mu\mu_i - \beta_i)^2}{2\alpha_i^2}\right],$$

when $n_i^{\text{obs}} \gg 1$ (in fact $n_i^{\text{obs}} > 10$ is a good approximation). Here I have introduced the following quantities:

$$\alpha_i \equiv \frac{\sqrt{n_i^{\text{obs}}}}{s_i^{\text{SM}}} \quad \text{and} \quad \beta_i \equiv \frac{n_i^{\text{obs}} - b_i}{s_i^{\text{SM}}}, \quad \text{where} \quad s_i^{\text{SM}} = \mathcal{L}\varepsilon_i\sigma_i^{\text{SM}}.$$

The important point to realise is that we have managed to write the three unknown quantities n_i^{obs} , b_i and ε_i in just two independent combinations, α_i and β_i .

Making the further reasonable approximation that $(n_i^{\text{obs}} - b_i)/b_i \ll 1$ we can deduce, as shown in eq. 3.24 in [57], that

$$\alpha_i \approx \frac{\sqrt{b_i}}{s_i^{\text{SM}}} = \frac{\mu_{i,\text{expected}}^{95\%}}{1.96}$$

if we interpret exclusion limits in the Bayesian sense. With this knowledge we can then infer the value of β_i from the *observed* $\mu_i^{95\%}$, provided by the experimental collaborations, by solving the following equation (eq. 3.22 in [57]) numerically:

$$0.95 \approx \frac{\text{Erf}\left(\frac{\mu_i^{95\%} - \beta_i}{\sqrt{2}\alpha_i}\right) + \text{Erf}\left(\frac{\beta_i}{\sqrt{2}\alpha_i}\right)}{1 + \text{Erf}\left(\frac{\beta_i}{\sqrt{2}\alpha_i}\right)},$$

where the error function $\text{Erf}(x) = \frac{2}{\sqrt{\pi}} \int_0^x e^{-t^2} dt$.

With the individual likelihoods approximately reconstructed in this way we can form the joint likelihood and calculate the combined $\mu^{95\%}$ (again, working in the Bayesian picture), finding it to be

$$\mu^{95\%} = \beta_{\text{comb}} + \sqrt{2}\alpha_{\text{comb}} \times \text{Erf}^{-1}\left[0.95 - 0.05 \times \text{Erf}\left(\frac{\beta_{\text{comb}}}{\sqrt{2}\alpha_{\text{comb}}}\right)\right],$$

where

$$\alpha_{\text{comb}} \equiv \left(\sum_i \frac{\mu_i^2}{\alpha_i^2}\right)^{-\frac{1}{2}}$$

and

$$\beta_{\text{comb}} = \alpha_{\text{comb}}^2 \times \sum_i \frac{\mu_i \beta_i}{\alpha_i^2}.$$

Using the procedure outlined above, I performed a scan over the MUED parameter space, calculating $\mu^{95\%}$ for each point (m_H, R^{-1}) . I used the $gg \rightarrow H \rightarrow \gamma\gamma$, $gg \rightarrow H \rightarrow W^+W^- \rightarrow \bar{\ell}\ell\nu\nu$ and $gg \rightarrow H \rightarrow ZZ \rightarrow 2\bar{\ell}2\ell$ channels from ATLAS and CMS Higgs boson searches. I scanned m_h in 2-GeV steps, R^{-1} in 12.5-GeV steps. There are also additional constraints on the parameter space. The Higgs mass range is bound from below by LEP limits and from above by the requirement that the dark matter candidate be neutral – see [58]. The inverse radius must be greater than around 600 GeV so as not to conflict with electroweak precision tests [59, 60], and less than 1600 GeV so that the dark matter candidate is not too heavy [58].

4.9.4 Results

Using our model's predictions of Higgs production enhancement for different values of m_H and R^{-1} together with experimental limits on Higgs boson production, we can exclude regions of the (m_h, R^{-1}) plane where $\mu^{95\%} < 1$. Initially, I statistically combined the CMS data from Fig. 6 (top) of [61] and the ATLAS data from Fig. 3 of [62] in each of the $\gamma\gamma$, W^+W^- and ZZ channels. Note that these data are from the old 7 TeV dataset, before the Higgs boson discovery.

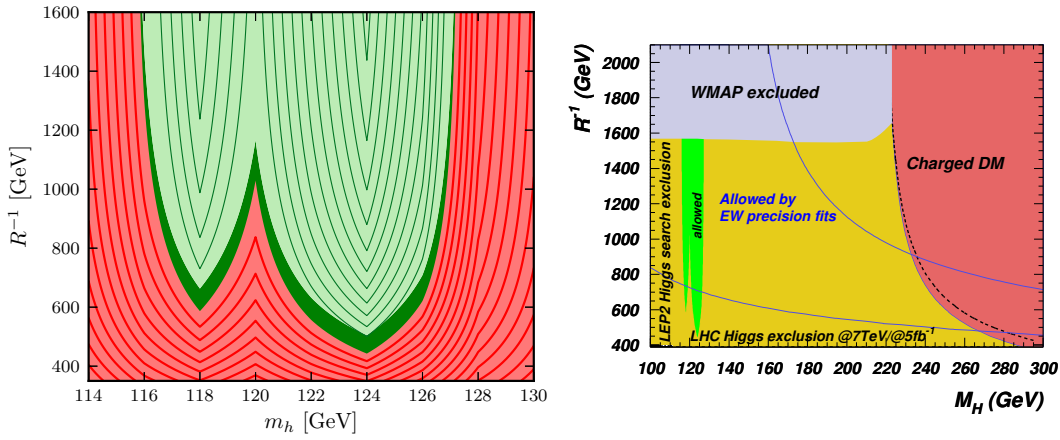


Figure 4.11: Left: exclusion of MUED (m_H, R^{-1}) parameter space at 95% CL from Higgs boson search using combined ATLAS and CMS limits in $\gamma\gamma$, W^+W^- and ZZ channels, based on the 7 TeV data. The allowed region is in light green and the excluded region is in light red. Dark green shows the additional allowed region when loop corrected KK masses are used instead of tree-level masses. Contours of constant $\mu_{\text{comb}}^{95\%}$ are shown in steps of 0.05. Right: Combination of limits on the MUED parameter space from: the Higgs constraints considered in this paper; EW precision tests (95% CL); and DM relic density limits for $\Lambda = 40R^{-1}$ (solid line) and $\Lambda = 20R^{-1}$ (dashed line) cases.

The resulting limits on MUED from the 7 TeV dataset are shown in Figure 4.11 (left). These constraints are combined with other constraints from DM relic density [58] as well as EW precision tests [59] in Figure 4.11 (right).

We can see that Higgs searches powerfully constrain MUED, in which Higgs production is enhanced. Compared to previous studies [51] we have included mass corrections for the particles in the loops, providing more realistic predictions of MUED cross sections, and have accurately combined non-universal enhancement for $\gamma\gamma$ and W^+W^-/ZZ signatures.

This new approach allows us to find accurate limits on the MUED (m_H, R^{-1}) parameter space. After combination of ATLAS and CMS limits for each individual channel ($\gamma\gamma$, W^+W^- and ZZ) in gluon-gluon fusion, we can see that $R^{-1} < 500$ GeV is excluded at 95%CL. For $500 \text{ GeV} < R^{-1} < 600$ GeV only a very narrow ($\pm 1 - 3$ GeV) mass window around $m_H = 125$ GeV is left. This is the region where the excess of the events in the Higgs search channels is reported by the ATLAS and CMS collaborations and where the exclusion limit is weaker. For even larger values of R^{-1} another narrow mass range around $m_H = 118$ GeV is allowed.

For a Higgs mass $m_H = 125$ GeV, Figure 4.12 displays the variation of the enhancement factor in the $gg \rightarrow H \rightarrow \gamma\gamma$ (top) and $gg \rightarrow H \rightarrow W^+W^-/ZZ$ (middle) channels as a function of R^{-1} together with the suppression factor in the $W^+W^-/ZZ \rightarrow H \rightarrow \gamma\gamma$ (bottom). The latter is relevant for the Higgs search in the $pp \rightarrow jj\gamma\gamma$. These plots can

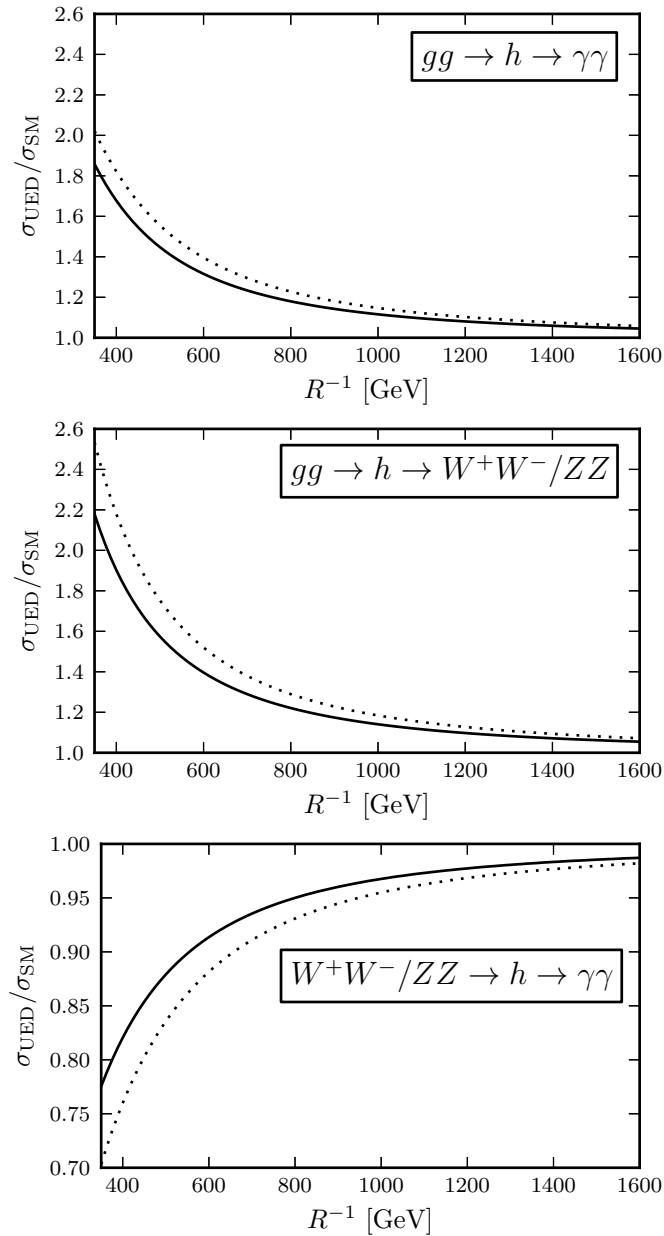


Figure 4.12: The variation with respect to R^{-1} of the MUED cross-sections for $gg \rightarrow H \rightarrow \gamma\gamma$ (top), $gg \rightarrow H \rightarrow W^+W^-/ZZ$ (middle) and $W^+W^-/ZZ \rightarrow H \rightarrow \gamma\gamma$ (bottom) channels relative to the SM for $m_H = 125$ GeV. Solid lines show results when using loop-corrected masses in the loops, while dashed lines correspond to tree-level masses.

be used to ascertain how a measurement of each channel's cross-section can be used to constrain the scale R^{-1} . For example, an enhancement in both the $gg \rightarrow H \rightarrow \gamma\gamma$ and the $gg \rightarrow H \rightarrow W^+W^-$ channel would favour the MUED model around the TeV scale while a large enhancement in $pp \rightarrow jj\gamma\gamma$ would disfavour the model.

After we performed the above analysis, new limits (calculated from the first tranche of 8 TeV data) were released by CMS [63] and ATLAS [64]. The data are strong enough

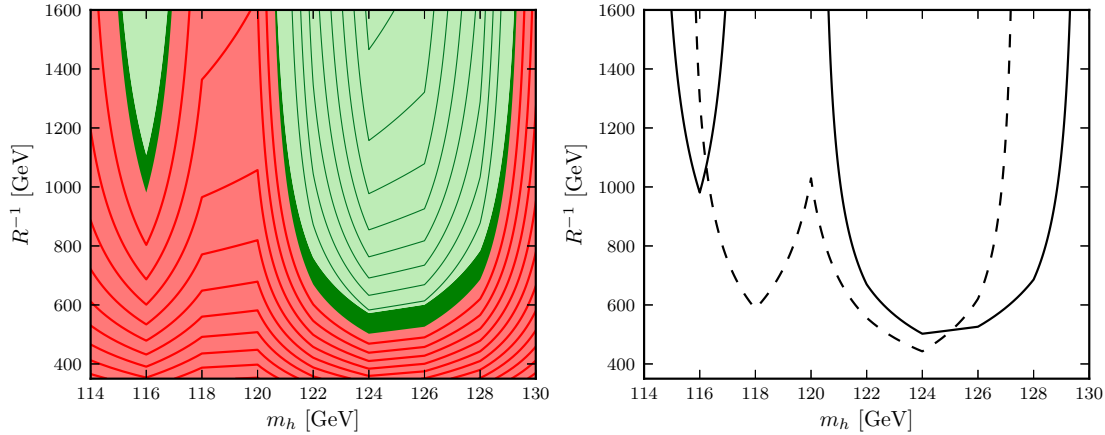


Figure 4.13: Left: limits on MUED parameter space from newer 7 TeV and 8 TeV ATLAS and CMS Higgs search data using the same conventions as in Figure 4.11 (left). Right: comparison of allowed regions for the combined 7 TeV and 8 TeV LHC data (solid) and 7 TeV data (dashed) using loop masses.

for each experiment to claim discovery of a Higgs-like particle with a mass of around 125 GeV, confirming the hints evident in earlier analyses. These newer ATLAS limits are shown for all channels in Fig. 16a of the supplementary figures associated with [64].³ CMS make their latest limits for $\gamma\gamma$ available in Fig. 4a of [65] and their limits for WW in Fig. 4 (right) of [63]. The CMS limits for the $H \rightarrow ZZ \rightarrow 4\ell$ channel can be found in the supplementary figures for [66].⁴

I calculated the constraints on the MUED parameter space in light of these new experimental data and the result is shown in Figure 4.13 (left). I also show a comparison of the allowed regions for the old and new data in Figure 4.13 (right).

The allowed region shrinks overall with the extra data, but the high and low m_H limits *relax*. This is actually to be expected: in the 2011 data, the W^+W^- channel surprisingly showed no excess of events around 125 GeV even though such an excess was observed in the other channels, including ZZ . In the new data, there is an excess in W^+W^- , bringing this channel in line with the others and thus *weakening* the limit on the MUED parameter space slightly at the edges of the allowed region where the diphoton channel is less restrictive. However, the improvement in limiting power of the diphoton channel causes the region $117 \text{ GeV} \lesssim m_H \lesssim 121 \text{ GeV}$ to become forbidden.

With the newer data then, all values of $R^{-1} < 500 \text{ GeV}$ are forbidden, leaving a small region of allowed parameter space 2–8 GeV wide around $m_H = 125 \text{ GeV}$ and another allowed island up to 2 GeV wide around 116 GeV for $R^{-1} > 1000 \text{ GeV}$.

³These can be found at <https://atlas.web.cern.ch/Atlas/GROUPS/PHYSICS/PAPERS/HIGG-2012-27/>

⁴<https://twiki.cern.ch/twiki/bin/view/CMSPublic/Hig12016TWiki>

4.10 Conclusions

We have seen that MUED is a relatively simple extension of the Standard Model involving just a single new parameter, the compactification scale R^{-1} (as well as weak dependence on the cutoff of the theory Λ). It has a good candidate for a Dark Matter particle in the lightest KK particle (the KK “photon” $P^{(1)}$ for most of the parameter space). We implemented the model consistently into the CalcHEP software package, incorporating the phenomenologically-vital radiative mass orbifold corrections in a gauge invariant way that is compatible with EWSB. Our CalcHEP model demonstrates unitary behaviour of KK W scattering because of its complete implementation of the KK Higgs sector.

With this powerful software tool we investigated possible discovery signatures for MUED, ultimately finding that the tri-lepton signature would allow one to exclude MUED up to $R^{-1} \approx 1200$ GeV with 20 fb^{-1} of data collected by the 8 TeV LHC. It seems likely that a similar analysis performed for the 14 TeV LHC would allow us to exclude the theory for compactification scales right up to the Dark Matter limit of 1.6 TeV.

In Section 4.9 we saw that LHC searches for the SM Higgs provide a powerful limit on the MUED model, where Higgs production is enhanced. I evaluated all one-loop diagrams for Higgs production $gg \rightarrow H$ and decay $H \rightarrow \gamma\gamma$ within MUED and independently confirmed previous results [54]. Based on these results, enhancement factors for Higgs boson production and decay were derived in the MUED parameter space. Then, using these factors I produced the first limits on the MUED parameter space that combine both limits from ATLAS and CMS collaborations for 7 TeV and 8 TeV LHC data and take into account statistical combination of several Higgs boson search channels properly. As for other extensions of the SM, the correct statistical combination of several Higgs boson search channels is important for MUED since these channels are not universally enhanced: the $gg \rightarrow H \rightarrow \gamma\gamma$ process is not enhanced as strongly as the $gg \rightarrow H \rightarrow WW$ or $gg \rightarrow H \rightarrow ZZ$ processes due to the fact that the decay $H \rightarrow \gamma\gamma$ is actually suppressed as compared to the Standard Model. Overall enhancement for $gg \rightarrow H \rightarrow \gamma\gamma$ nevertheless takes place because the enhancement of $gg \rightarrow H$ overcomes the suppression in the $H \rightarrow \gamma\gamma$ decay.

In contrast to previous studies [51], here the mass corrections for the KK-particles in the loop were included. The comparison between the computations with tree-level and radiatively corrected masses provides information about the theoretical uncertainties in the enhancement of the Higgs boson production and decay within the MUED model. Also, we think that including these mass corrections gives more precise result and allows one to take into account some part of the higher order corrections. This is because one-loop corrected masses give a better approximation to pole masses and because the coupling constants that couple the gluon (or photon) to the KK quarks are protected (by gauge invariance) from receiving radiative corrections.

As a result I have found an accurate limit on MUED in the (m_H, R^{-1}) parameter space. After combination of ATLAS and CMS limits for each individual channel ($\gamma\gamma$, WW^* and ZZ^*) for the late 2012 7 TeV and 8 TeV Higgs data, we can see that $R^{-1} < 500$ GeV is excluded at 95%CL, while for larger R^{-1} only a very narrow ($\pm 1 - 4$ GeV) mass window around $m_H = 125$ GeV (the mass of the recently observed Higgs-like particle), and another smaller window around 118 GeV (for $R^{-1} > 1000$ GeV) remain allowed.

Since the above analysis was performed, further data has been made available by the experimental collaborations. Also, I have developed software implementations of more sophisticated statistical techniques, explained Section 6.5, that could be used to constrain the MUED model further, perhaps pushing R^{-1} above the TeV scale. MUED deserves to be examined again in this new context to either pin down the most likely compactification scale, or else exclude the model completely.

With detailed information on individual Higgs boson production and decay processes provided by CMS and ATLAS experiments, one can understand much better the nature of the Higgs boson and interpret it within MUED or other BSM theories.

Chapter 5

The 4D Composite Higgs Model

In this chapter I start in Section 5.1 by explaining the hierarchy problem of the SM, which was mentioned in the Introduction. I go on in Section 5.2 to describe a class of models, called “composite Higgs” models, that aim to solve the problem by postulating that the Higgs boson is a Goldstone boson. I then discuss work that I performed as part of a collaboration and which is published in [4] where we focussed on a particular type of composite Higgs model called the 4D Composite Higgs Model (4DCHM), whose particle content and couplings I outline in Section 5.3. In our project we examined the parameter space of the 4DCHM in view of the discovery of the Higgs boson. In Section 5.4 I explain how we calculated the Higgs signal enhancement factors before outlining the statistical procedure we adopted to compare the predictions with LHC Higgs data in Section 5.5. In Section 5.6 I present the results of a scan over the parameter space, investigating the possible variations in Higgs couplings that can occur in some detail and demonstrating that the model is a good fit to LHC data (once other constraints have been applied). Finally, I present some conclusions in Section 5.7.

5.1 The hierarchy problem

As mentioned in Chapter 1, there is a problem with the SM called the hierarchy problem. This problem can be understood as a fine-tuning problem as follows. Consider the Higgs sector of the SM Lagrangian shown in Equation 2.23. The mass of the Higgs is $\sqrt{2}\mu$, so this implies that $\mu = 125/\sqrt{2}$ GeV ≈ 90 GeV. If we write the physical coupling in terms of the bare coupling μ_0 as $\mu \approx \mu_0 + \delta\mu$, we can consider the one-loop contribution to $\delta\mu$ due to a Higgs boson running in a loop. This loop is proportional to the Higgs quartic coupling λ , and diverges quadratically with the loop momenta. As is typical with renormalisable theories, μ_0 must be tuned to have just the right cutoff dependence to cancel the divergence of the loop diagram and yield the correct Higgs mass. This is

just the same as in QED, where the bare electron mass must be tuned to cancel the (logarithmic) divergence in the electron self-energy loop diagram.

If the SM is seen as a complete, renormalisable quantum field theory (and it is believed to be self-consistent to assume this), there is no problem with the above argument. However, the strangeness of the Higgs boson corrections, when compared to all other corrections such as the QED mass correction, can be seen if the SM is assumed to be an effective low energy theory of a more complete theory that becomes important at scales above some cutoff, Λ . The loop momentum integrals involved in calculating the mass corrections should then be evaluated up to this cutoff (rather than infinity) and so, we have (schematically), for the Higgs and electron mass corrections respectively,

$$\mu^2 \sim \mu_0^2 - C\lambda\Lambda^2 \quad (5.1)$$

$$m_e \sim m_{e,0} - C'm_{e,0} \ln \Lambda. \quad (5.2)$$

It is not known at what scale new physics must become important, but it must almost certainly occur before the Planck scale Λ_{Pl} at which gravitational interactions become strongly-interacting. It is estimated that $\Lambda_{\text{Pl}} \approx 10^{19}$ GeV. Using $\Lambda = \Lambda_{\text{Pl}}$ in Equation 5.2 gives (very roughly)

$$\mu^2 \sim \mu_0^2 - 10^{38} \text{ GeV}^2 \quad (5.3)$$

$$m_e \sim (1 - 19)m_{e,0}, \quad (5.4)$$

(assuming the λ coupling is of order unity). The tuning of $m_{e,0}$ is reasonably natural, whereas μ_0^2 must be very finely tuned to a few parts in 10^{38} in order reproduce the desired Higgs mass around 125 GeV.

The huge fine tuning is because of the large hierarchy between the New Physics scale (assumed here to be $\Lambda_{\text{Pl}} = 10^{19}$ GeV) and the electroweak symmetry breaking scale $v = 246$ GeV, related to the Higgs mass via $m_H = \sqrt{2\lambda}v$). One way of rendering the SM “natural” is to postulate that New Physics becomes important at a much lower scale than Λ_{Pl} , e.g. $\Lambda_{\text{NP}} = 1$ TeV. This would mean that we should be observing the effects of the New Physics at energies being probed by the LHC, however, and so far we have seen nothing.

Another possible solution to the problem is hinted at by the QED mass corrections. The hierarchy of scales is even worse between Λ_{Pl} and m_e , and yet there is no fine tuning in QED. An explanation of this is that the electron mass is “protected” by a symmetry. This means that, if the electron mass is set to zero, the symmetry group of the Lagrangian is enlarged to include “chiral symmetry”: the independent flavour mixing of left- and right-handed fermions. This is associated with logarithmic corrections; note also that the radiative corrections are *multiplicative*: they are proportional to the mass,

and so go to zero as the mass is sent to zero. In the Higgs theory, there is no symmetry enlargement as $\mu \rightarrow 0$ and we see that the corrections are quadratic and additive.

5.2 Composite Higgs models

The idea that the Higgs can be light if its mass is protected by some symmetry is motivation for a class of theories known as composite Higgs models. These models postulate that the Higgs is a pseudo-Nambu-Goldstone boson (PNGB) of some broken global symmetry. This symmetry is in fact only approximate in that it is broken explicitly in the Lagrangian, meaning that the Higgs is not massless, but acquires a mass of the order of the explicit symmetry breaking. However, because setting the mass to zero is associated with a restoration (in the Lagrangian, but not the vacuum) of the global symmetry, the Higgs mass is protected from fine tuning as described above, and so the theory is natural.

As an explicit example, consider the Minimal Composite Higgs model (MCHM) introduced in [67]. This postulates the existence of a new fermionic sector, interacting strongly through some gauge interaction and also obeying a global $SO(5)$ symmetry. The interactions are so strong that at some high scale, confinement occurs and one should describe physics in terms of bound states of the new particles. It is further postulated that, upon confinement, some condensate forms that spontaneously breaks the $SO(5)$ symmetry down to $SO(4)$. There are therefore four broken generators and, by Goldstone's theorem, each is associated with a massless "Goldstone boson". By careful assignment of EW quantum numbers to the new fermions, one can arrange for the four Goldstone bosons to transform under the SM gauge group identically to the SM Higgs doublet. This "weak gauging" also *explicitly* breaks the global symmetry, giving the Goldstone bosons mass naturally around the EW scale v . This model is minimal in the sense that it provides just enough Goldstone bosons to furnish a Higgs doublet.

Generally, composite Higgs theories are analysed using holographic techniques whereby a weakly coupled 5D theory with some compactified (and possibly warped) extra dimension is deduced to be dual to the 4D strongly coupled composite theory. Once this duality has been established, the terms in the 4D low energy Lagrangian (i.e. the Lagrangian below composite scale) can be calculated perturbatively in the 5D theory. In fact, the MCHM is defined in 5D and "deconstructed" (effectively put on a lattice along the fifth dimension) to form the 4D theory. Deconstructing with more lattice points ("sites") reproduces more resonances in the 4D theory.

	Particle	$SU(3)_c$	$U(1)_{EM}$
Neutral gauge bosons	Z_1, Z_2, \dots, Z_5	1	0
Charged gauge bosons	$W_1^\pm, W_2^\pm, W_3^\pm$	1	± 1
SM-like quarks	T_1, T_2, \dots, T_8	3	$2/3$
	B_1, B_2, \dots, B_8	3	$-1/3$
Exotic quarks	\tilde{T}_1, \tilde{T}_2	3	$5/3$
	\tilde{B}_1, \tilde{B}_2	3	$-4/3$

Table 5.1: Particle content of the 4DCHM, showing the EM and colour charges.

f	Composite scale
g^*	Common gauge coupling of $SO(5) \times U(1)_X$
m_*	Mass parameter for new fermionic resonances
$\Delta_{tL}, \Delta_{tR}, \Delta_{bL}, \Delta_{bR}$	Mixing parameters between elementary and composite sectors
$Y_T, Y_B, M_{Y_T}, M_{Y_B}$	Yukawa couplings of the composite sector

Table 5.2: Parameters in the 4DCHM

5.3 The 4D composite Higgs model: particle content and parameter space

In the project described in this chapter, I worked with collaborators on exploring a particular composite Higgs model known as the 4D composite Higgs model (4DCHM). We focussed on the Higgs phenomenology of the model, comparing predictions to the LHC Higgs data. The list of my collaborators and the work itself can be found in [4].

A detailed explanation of the 4DCHM and its Lagrangian can be found [68] and the model itself was proposed and detailed in [69]. I describe the particle content here in Table 5.1 and the parameters of the 4DCHM are given in Table 5.2.

The Standard Model is embedded within the 4DCHM and, as such, the SM parameters are calculable functions of the 4DCHM parameters. The SM parameters have been heavily constrained by data, so we can use these constraints to constrain the 4DCHM parameter space. Throughout our analysis, we fixed the composite scale f and the common composite gauge coupling g_* to benchmark values and scanned over the other parameters. For each parameter choice, we used our own Fortran routine, linked to the CalcHEP model described in [68]¹ to diagonalise the 4DCHM Lagrangian and partially invert the parameters so that the values of e , m_Z and G_F (Fermi’s constant of beta decay) were input parameters, set to the values given by the Particle Data Group [70]. For each point in our scans, we calculated the SM quantities m_t , m_b and m_H . Throughout the analysis, we only kept points where these masses fell in the ranges $165 \text{ GeV} \leq m_t \leq$

¹This model is publicly available at the High Energy Model Database (HEPMDB) at <http://hepmdb.soton.ac.uk/hepmdb:1212.0120> under the name “4DCHM”

175 GeV, $2 \text{ GeV} \leq m_b \leq 6 \text{ GeV}$ and $124 \text{ GeV} \leq m_H \leq 126 \text{ GeV}$. The large ranges on the masses are to account for the theoretical uncertainty introduced when running down the common 4DCHM prediction of m_* from the composite scale. Furthermore, we took bounds from the electroweak precision tests (EWPTs) performed at LEP2 into account by requiring that the mass of the new gauge bosons exceeded 2 TeV, as well as constraints based on the values of the $W^- t\bar{b}$, $Zt\bar{t}$ and $Zb\bar{b}$ couplings, as discussed in [68]. We made the simplifying assumption throughout this analysis that the new composite quark resonances only mix with the SM top and bottom quarks but in a more general model involving all SM generations, flavour physics constraints would have to be taken into account (see, for example, [71]).

The extra quarks in the theory must be heavy enough that they have avoided direct detection so far at the LHC. Because of their SM-like charges and strong couplings, the T_i and B_i quarks have production cross-sections that differ from the SM only due to the mass of the quarks. This means that these new quarks could possibly be detected in direct t' and b' searches at the LHC. CMS have performed searches for such quarks, each in two decay channels. For the t' 's, they considered [72] 5 fb^{-1} of integrated luminosity in the W^+b final state and also 1.14 fb^{-1} of data [73] in the Zt final state. For b' they conducted a search in W^-t using 4.9 fb^{-1} of integrated luminosity [74] and also in Zb using 4.9 fb^{-1} [75]. They make available, in each case, the upper limits on $\sigma(pp \rightarrow q'q') \times Br(q' \rightarrow XY)^2$, where XY final state considered by the particular search, as a function of q' mass. These limits are plotted in are plotted in Figure 5.1 in red, where the dotted lines are our linear extrapolations of the experimental data. CMS quotes mass limits on the t' and b' by calculating the predicted value of the cross-section, assuming 100% branching to the final state considered. We used an online program [76] to calculated the production cross-section with QCD effects included, shown using black lines. The mass limit is found by observing the value of mass for which the cross-section prediction exceeds the limit. This mass limit is not directly applicable to out T_i and B_j because these do not decay 100% to any particular final state, and so we have to test each point in scan of the 4DCHM parameter space with the experimental limit. The purple circles are found by multiplying this figure (for the particular mass) by the relevant branching ratio squared, which is a function of the model parameters, and so the points always lie below the black line.

There searches were from the 7 TeV run of the LHC, but later results do not change our conclusions. We have ignored correlations between the masses of T_1 and B_1 that are due to their dependence on the common mass parameter m_* , although we believe this will not make a significant difference.

When scans over parameters are performed later in this section, any points falling above the red limit lines in the Figure 5.1 are rejected. The illustrative points shown in Figure 5.1 are from a random scan over all parameters with the composite scale and

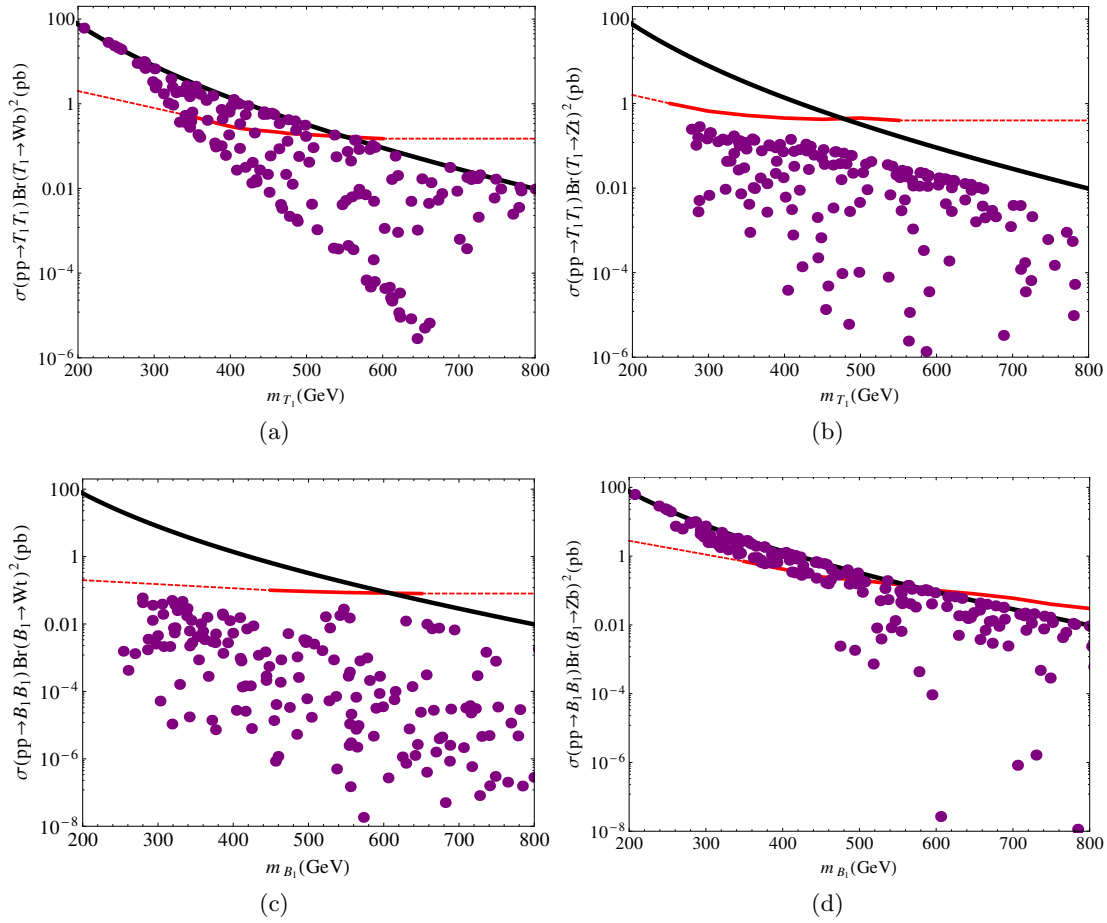


Figure 5.1: Limits on the masses and production cross-sections of T_1 ((a) and (b)) and B_1 ((c) and (d)) from CMS direct t' and b' searches. The purple circles show the points in our parameter scan for fixed $f = 1$ TeV and $g_* = 2$ that survive the SM parameter constraints. The red lines show the experimental limits (with our extrapolations shown with dots). The black lines show the predicted cross-sections in the 4DCHM for a generic heavy quark, assuming 100% branching to the state shown in the y-axes labels.

common gauge coupling fixed to $f = 1$ TeV and $g_* = 2$, having already rejected points that fail to match the SM masses as described above.

We should also constrain the masses of \tilde{T}_i and \tilde{B}_i in light of this experimental data. This is, in fact, a simpler proposition because these quarks do decay very near 100% of the time into particular final states because of their exotic charges. For example, the \tilde{T}_1 decays almost always into W^+t and so one can use the b' search [74] into that channel to constrain the \tilde{T}_1 mass. The quoted mass limit of 650 GeV can be applied directly without requiring one to calculate branching ratios.

5.4 Signal enhancement factors from the Lagrangian

In MUED, the Higgs phenomenology of which I described in Section 4.9, all Higgs couplings to SM particles were the same as the SM predictions except for the effective one-loop couplings to gluons and photons due to new KK particles running in the loops. In the 4DCHM, the composite Higgs couplings to all SM particles are in general complicated functions of the fundamental model parameters listed in Table 5.2. All of the tree-level couplings can be calculated using our CalcHEP implementation.

However, just as in the Standard Model, there are no Hgg and $H\gamma\gamma$ couplings at tree level: these occur at one loop, to leading order. We calculated the effective coupling of an on-shell Higgs to gluons and photons at one loop, including contributions from the SM particles as shown in Equation 3.35, in addition to contributions from the new q' quarks and W' and Z' effective bosons, all listed in Table 5.1. The new exotically-charged quarks do not couple to the composite Higgs. It should be noted that the couplings of the new particles to the composite Higgs are not proportional to the particles' masses, so the standard formulae in Equation 3.40 cannot be used directly. Once the quantities were calculated by hand, they were added manually as new vertices to our CalcHEP model.

Armed with expressions for all of the composite Higgs couplings, let us turn to the experimentally-observable quantities. Let X denote the process (e.g. gluon-gluon fusion) by which a Higgs boson is produced, and Y denote its on-shell decay products. To a good approximation the number of events for the XY process in a particular event category c is

$$N_{XY}^c \equiv \sigma_X \times \text{BR}_Y \times \varepsilon_{XY}^c \times L, \quad (5.5)$$

where σ_X is the $pp \rightarrow H$ production cross-section via the production process X , BR_Y is the branching ratio of $H \rightarrow Y$, and L is the integrated luminosity. The efficiency factor ε_{XY}^c (technically combining the cut acceptance and efficiency) gives the fraction of the total XY events that are selected in event category c . Currently there are 43 event categories between ATLAS and CMS, an example of which would be the ATLAS diphoton *unconverted, central, low- p_T* category.

If the cuts performed in event category c were completely efficient at isolating one of the production processes (i.e. so that all efficiency factors were zero except for one choice of XY) then one could usefully define a “signal enhancement” factor as the ratio between N_{XY}^c and the corresponding SM prediction. This would give

$$\mu_{XY} = \tilde{\sigma}_X \times \frac{\tilde{\Gamma}_Y}{\tilde{\Gamma}_{\text{tot}}}, \quad (5.6)$$

where a tilde denotes a (dimensionless) quantity expressed in SM units, e.g. $\tilde{\sigma} \equiv \sigma/\sigma^{\text{SM}}$. In reality, no cut can be 100% pure, and a category that is designed to isolate one

particular method of Higgs production will invariably be contaminated by events from another production process. Therefore, what is measured experimentally is the number of events inclusive of all production processes X . The signal enhancement factor is then

$$\mu_Y^c = \sum_X \tilde{\sigma}_X R_{XY}^{c, \text{SM}} \times \frac{\tilde{\Gamma}_Y}{\tilde{\Gamma}_{\text{tot}}}, \quad (5.7)$$

where

$$R_{XY}^{c, \text{SM}} \equiv \frac{\sigma_X^{\text{SM}} \varepsilon_{XY}^c}{\sum_{X'} \sigma_{X'}^{\text{SM}} \varepsilon_{X'Y}^c} \quad (5.8)$$

gives the fraction of Higgs bosons produced through the process X , in the SM, with acceptances and efficiencies for the final state Y and event category c included. As an example, if we consider again the ATLAS diphoton *unconverted, central, low- p_T* category, the fraction of the observed Higgs boson events produced through the gluon-gluon fusion process would be 93.7% [77], assuming the SM.

5.5 Statistical procedure

In contrast to the MUED project detailed in Section 4.9, we started the 4DCHM project after the discovery of the Higgs boson. This meant that we could make use of the best-fit values of the Higgs couplings to SM particles that the experimental collaborations released after the discovery, rather than having to infer these quantities from the Brazil band exclusion plots, as detailed previously.

We used these best-fit signal enhancement factors in each available final state Y and cut category c , and followed the procedure as has been done previously, for example, in [78, 79, 57, 80, 81, 82, 83, 84, 85, 86]. In this method, a χ^2 test statistic

$$\chi^2(\boldsymbol{\mu}) = \sum_{i,c,Y} \frac{(\mu_Y^{c,i} - \hat{\mu}_Y^{c,i})^2}{\Delta(\mu_Y^{c,i})^2} \quad (5.9)$$

is formed, using the experimental collaborations' best-fit values of the enhancement factors ($\hat{\mu}$) and the given 1σ uncertainties $\Delta(\mu)$. The sum is taken over all final states Y , cut categories c and experimental collaborations $i \in \{\text{ATLAS, CMS}\}$. One assumes this statistic follows a χ^2 distribution with a number of degrees of freedom equal to the number of terms in the sum, and uses this to deduce the p -value for a particular hypothesis.

The difficulty with this method is in computing μ_Y^c in a particular model. One must evaluate the expression in Equation 5.7, but the experimental collaborations only make the efficiency factors (or, equivalently the ratios defined in Equation 5.8 available in the diphoton and $\tau^+\tau^-$ channels, so assumptions must be made for the other channels.

We proceeded in this project (although see Chapter 6 for a more sophisticated approach) by assuming that, in each category, a particular production process X dominated over all others. Under this assumption, in Equation 5.7 and Equation 5.8, only one term in the sums over the production modes is significant, and so the efficiency factors cancel in the ratio. Equation 5.7 thus becomes

$$\mu_Y^c \approx \tilde{\sigma}_X \times \frac{\tilde{\Gamma}_Y}{\tilde{\Gamma}_{\text{tot}}}. \quad (5.10)$$

Rather than using specific, exclusive cut categories (such as the ATLAS diphoton *unconverted, central, low- p_T* category mentioned previously), we made use of the inclusive results for each final state Y , meaning we can drop the index c from the above expressions. For the final states $Y = \gamma\gamma, WW, ZZ$, we assumed that the gluon-gluon fusion production process dominates. For the $b\bar{b}$ final state, however, ATLAS and CMS chose cuts to remove as much QCD background as possible, which effectively means that the cuts attempt to isolate Higgs events produced in association with a weak vector boson (also known as Higgs-strahlung). Our predictions for the signal enhancement factors therefore take the simple forms

$$\mu_{\gamma\gamma} = \tilde{\sigma}_{\text{ggF}} \times \tilde{\Gamma}_{\gamma\gamma} \times \tilde{\Gamma}_{\text{tot}}^{-1} \quad (5.11)$$

$$\mu_{WW} = \tilde{\sigma}_{\text{ggF}} \times \tilde{\Gamma}_{WW} \times \tilde{\Gamma}_{\text{tot}}^{-1} \quad (5.12)$$

$$\mu_{ZZ} = \tilde{\sigma}_{\text{ggF}} \times \tilde{\Gamma}_{ZZ} \times \tilde{\Gamma}_{\text{tot}}^{-1} \quad (5.13)$$

$$\mu_{b\bar{b}} = \tilde{\sigma}_{\text{VH}} \times \tilde{\Gamma}_{b\bar{b}} \times \tilde{\Gamma}_{\text{tot}}^{-1}. \quad (5.14)$$

The cross-sections and partial widths in these equations were calculated for each point in the parameter scan using CalcHEP. In fact, the decays to WW and ZZ were further cascaded to the primary final states used by ATLAS and CMS in these channels: $2\ell 2\nu$ and 4ℓ respectively. Our calculation took into account the (albeit small) interference from the W 's and Z 's as well.

We compared these predictions with the most up-to-date experimental best-fit values available at the time, summarised in Table 5.3, using the χ^2 test statistic shown in Equation 5.9. For the asymmetric CMS uncertainties, we took an average to use for the Δ 's in Equation 5.9.

5.6 Results

The results from the LHC suggests a broadly SM-like Higgs and so we should first see how SM-like the signal enhancement factors predicted by the 4DCHM tend to be. For this purpose, we fixed $f = 1$ TeV and $g_* = 2$ and randomly scanned over the remaining parameters, rejecting points which did not match SM mass predictions and which were incompatible with direct searches for heavy quarks as described above.

	ATLAS	CMS
$\hat{\mu}_{\gamma\gamma}$	1.8 ± 0.4	$1.564^{+0.460}_{-0.419}$
$\hat{\mu}_{ZZ}$	1.0 ± 0.4	$0.807^{+0.349}_{-0.280}$
$\hat{\mu}_{WW}$	1.5 ± 0.6	$0.699^{+0.245}_{-0.232}$
$\hat{\mu}_{bb}$	-0.4 ± 1.0	$1.075^{+0.593}_{-0.566}$

Table 5.3: Summary of the LHC measurements of some μ parameters from ATLAS [87] and CMS [88] data. (The CMS paper only presents the data in a box-plot, though the numerical values can be found in the CMS Higgs TWiki, <https://twiki.cern.ch/twiki/bin/view/CMSPublic/Hig12045TWiki>).

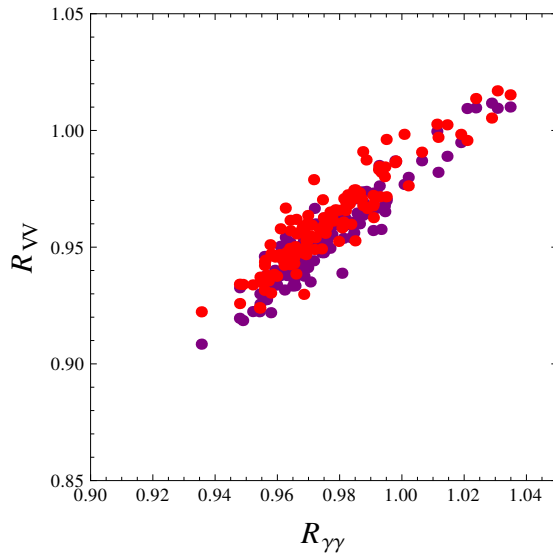


Figure 5.2: Correlation between $\mu_{\gamma\gamma}$ and μ_{VV} ($R \equiv \mu$), where $VV = WW$ (red) and ZZ (purple), from Equation 5.10 in the 4DCHM for the benchmark point $f = 1$ TeV and $g_* = 2$. All points generated here are compliant with direct searches for t' 's, b' 's and exotic quarks with charge $5/3$.

For each point in the scan, we calculated the signal enhancement factors μ_γ . The enhancement factors for the bosons are shown in Figure 5.2 (taken from our paper [4], where we used R in place of μ). There is clearly a correlation between the diphoton enhancement and the WW and ZZ enhancements, implying a common link in the modification of the diphoton and VV rates relative to the SM. Also, there is a strong preference for suppression of both rates relative to the SM (the majority of points have an enhancement of less than one in each channel, with the diphoton suppression being the least).

It is informative to investigate the behaviour of the ingredients, as seen in Equation 5.10, that went in to calculating the signal enhancement factors. Using the notation suggested by the LHC Higgs Cross-Section Working Group [89], let us define

$$\kappa_X^2 = \tilde{\Gamma}_{XX} \equiv \Gamma_{XX}/\Gamma_{XX}^{\text{SM}}, \quad (5.15)$$

where κ_X is effectively the enhancement of the coupling of the Higgs to a pair of particles XX at the Lagrangian level. In this same notation the ratio of the total widths is defined to be

$$\kappa_H^2 = \tilde{\Gamma}_{\text{tot}} \equiv \Gamma_{\text{tot}}/\Gamma_{\text{tot}}^{\text{SM}}. \quad (5.16)$$

First, let us examine κ_H for our scan. Of all the parameters that originate in the 4DCHM, the total width depends most strongly on the masses of the lightest new quarks, T_1 and B_1 . In Figure 5.3 we plot κ_H^2 and the masses of T_1 (left) and B_1 (right) for each scan point. In this figure we *kept* points in the scan that failed the heavy quark searches in order to demonstrate the very strong dependence of width on the heavy quark masses as low values of mass: one can see that points in the parameter space leading to small masses can cause κ_H^2 to drop to as low as 0.3, although the effect is still large, even with the direct search limits are applied (giving reductions of as much as 0.2).

When the T_1 and B_1 masses are taken to large values, the effects of the new particles, both via mixing and by direct running in loop diagrams, decouple. In this limit, the fact that $\kappa_H^2 < 1$ is due to the Higgs being a PNCB: its tree level couplings to vectors and fermions (divided by the corresponding Standard Model values), respectively

$$\kappa_V = \sqrt{1 - \xi} \quad (5.17)$$

$$\kappa_f = \frac{1 - 2\xi}{\sqrt{1 - \xi}}, \quad (5.18)$$

decrease, where $\xi = v^2/f^2$ (see, for example, [90]). The vector relationship is generic for $\text{SO}(5) \rightarrow \text{SO}(4)$ theories and the fermion expression holds for fermions that transform in the fundamental of $\text{SO}(5)$. This effect means that the $H \rightarrow b\bar{b}$ width is reduced with respect to the SM and, since this decay channel dominates the total Higgs width in the 4DCHM as it does in the SM, κ_H will receive an overall reduction.

As the masses of T_1 and B_1 are reduced, the effects of the heavy quarks become significant. The main effect on the width is $b - b'$ mixing that reduces the coupling of the SM b to Higgs still further. This explains the decrease in κ_H^2 as the heavy quark masses are decreased (a decrease in the mass of T_1 will correlate with a decrease in B_1).

This suppression of the total width, in isolation, would act to *increase* the signal enhancement factor in any channel (except $b\bar{b}$), in contradiction to what we observe in Figure 5.2. We should therefore look at the production rate, which is dominated by gluon-gluon fusion in all but the $b\bar{b}$ channel: the behaviour of κ_g^2 is plotted as a function of the T_1 and B_1 masses in Figure 5.4. From this we see that the coupling is indeed also suppressed, compensating for the suppression of the width. The mechanism for this is the same: at high heavy quark masses there is a generic suppression in the coupling of the Higgs to fermions and so the gluon fusion production process, dominated by a loop of top quarks, is reduced due to the suppressed top Yukawa. As the heavy quark masses decrease, $t - t'$ and $b - b'$ mixing reduces the coupling of the Higgs to the SM top and

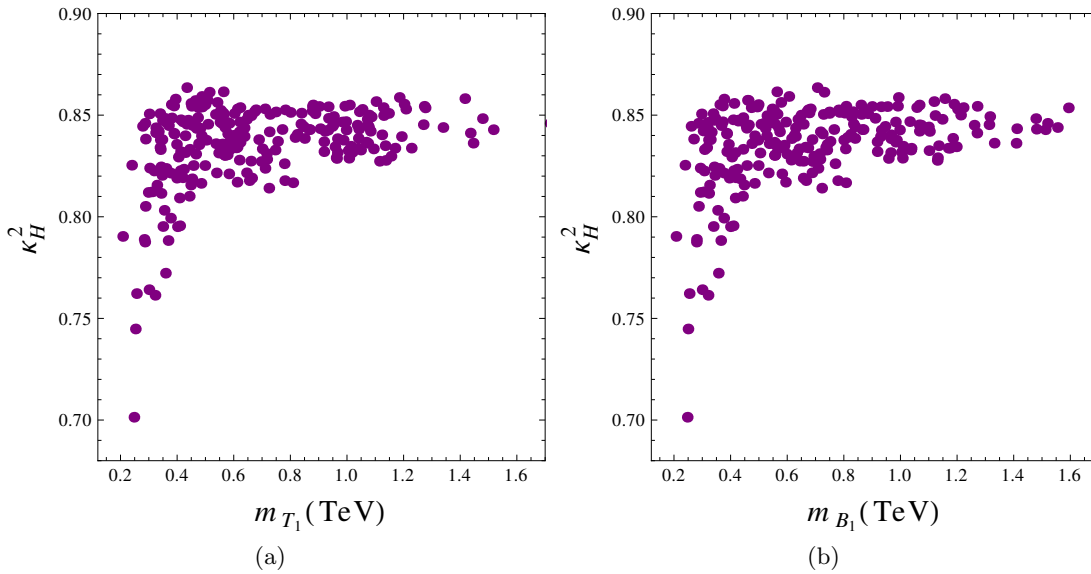


Figure 5.3: The distributions of κ_H values entering Equation 5.10 as a function of (a) m_{T_1} and (b) m_{B_1} in the 4DCHM for the benchmark point $f = 1$ TeV and $g_* = 2$.

bottom quarks still further, increasing suppression as we see in the figure. Ultimately, there is cancellation between the suppression of κ_g and κ_H .

Finally, let us investigate the $pp \rightarrow H \rightarrow \gamma\gamma$ decay modification. In Figure 5.5 the photon-photon-Higgs coupling squared (κ_γ^2) is plotted as a function of the T_1 and B_1 masses. The same arguments follow, although one must now take into account that $H \rightarrow \gamma\gamma$ receives interfering contributions from a (mainly top) quark loop and a loop of W bosons (in addition to loops of new particles, although these effects are sub-leading). The HW and Htt couplings are smaller than the SM expectation by virtue of Equations 5.17 and 5.18, although the overall suppression comes out to be of order 6% compared to the roughly 10% suppression seen in κ_g . With lighter heavy quark masses, the $t - t'$ mixing becomes significant and tends to suppress the top loop contribution to κ_γ . The W contribution is also suppressed, but not by as much. The overall effect is for κ_γ to *increase* due to the reduced destructive interference from the top loop. There is also an effect from the new SM-like heavy quarks running in the loop, but the effect from W 's is small due to their greater mass.

In Figure 5.6 I plot the values of the signal enhancement factors in each of the major decay channels studied at the LHC. Six benchmark values for f and g_* are shown, and for each benchmark the remaining parameters were scanned over. The results are shown as histograms, with the heights of the bars showing how many of the points in the scan had a value of μ in the range spanned by the bar. Also plotted are the best-fit measurements of the signal enhancements in each experiment (listed in Table 5.3). One can see clearly here that the majority of scan points (having rejected points that give

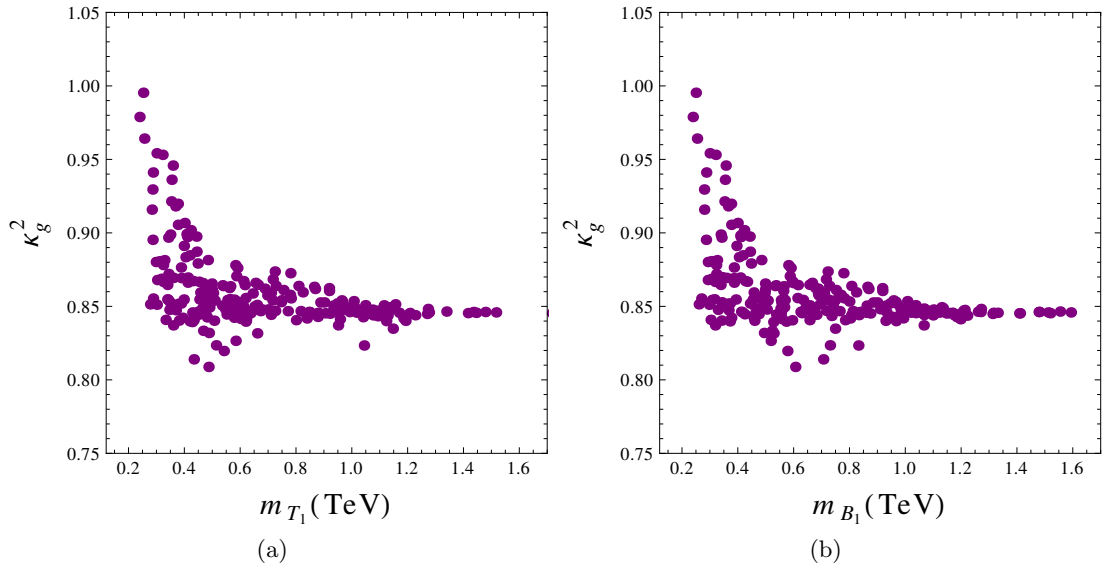


Figure 5.4: The distributions of κ_g values entering Equation 5.10 as a function of (a) m_{T_1} and (b) m_{B_1} in the 4DCHM for the benchmark point $f = 1$ TeV and $g_* = 2$.

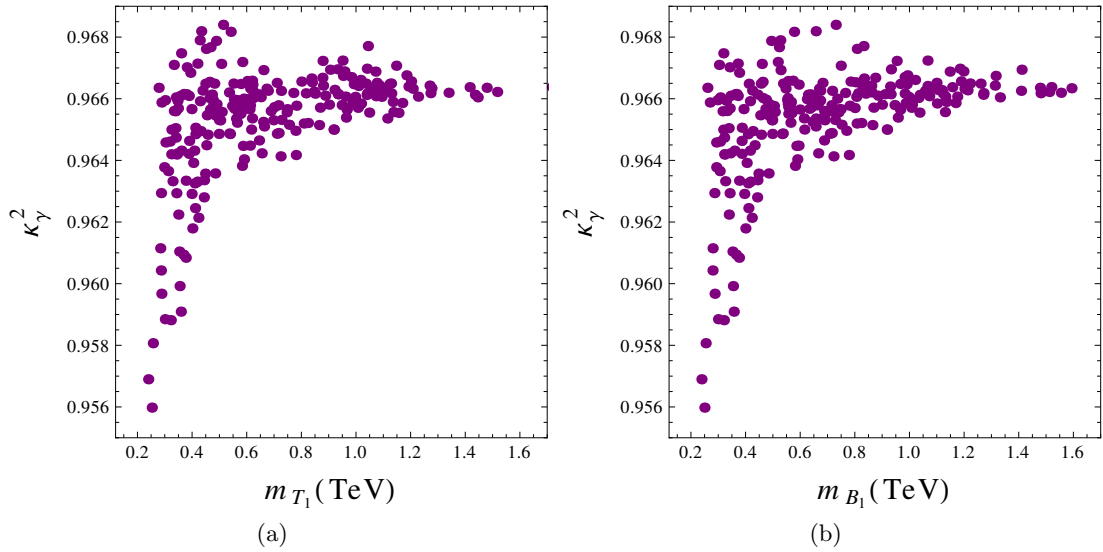


Figure 5.5: The distributions of $\kappa_{\gamma\gamma}$ values entering Equation 5.10 as a function of (a) m_{T_1} and (b) m_{B_1} in the 4DCHM for the benchmark point $f = 1$ TeV and $g_* = 2$.

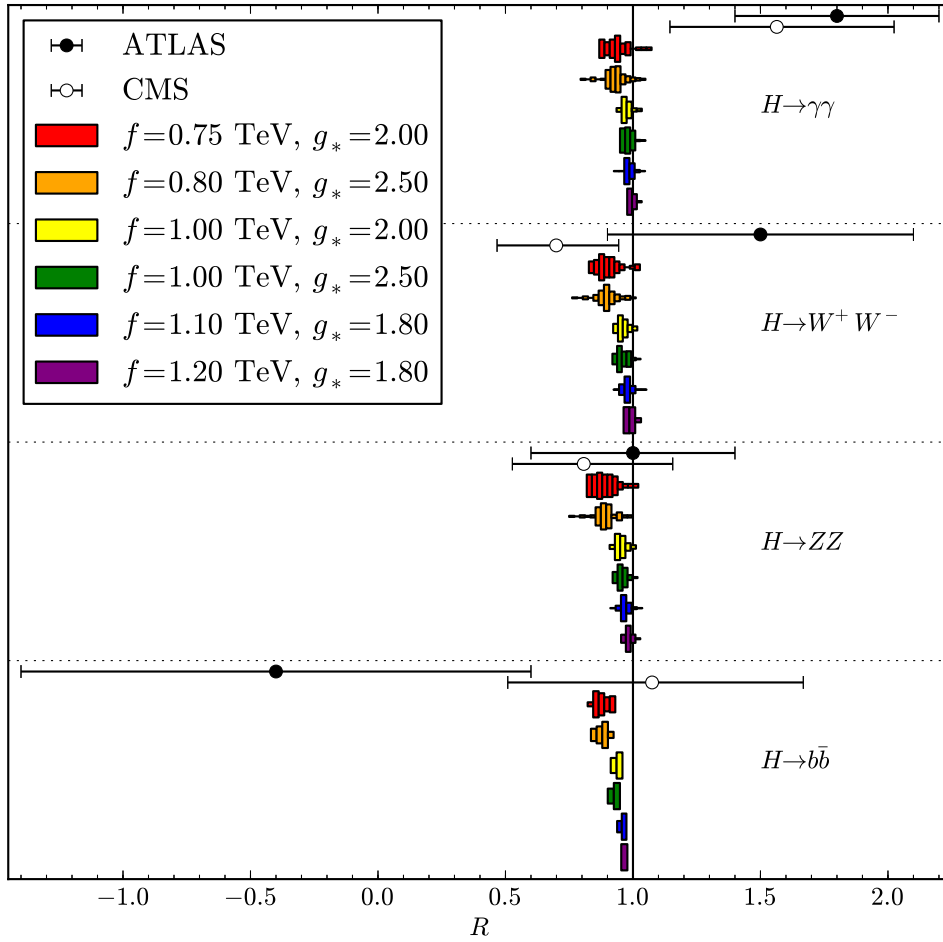


Figure 5.6: Comparison of the μ 's from Equation 5.10 with the measured experimental values by ATLAS [87] and CMS [88] (see Table 5.2) in the 4DCHM for all benchmark points in f and g_* . All points generated here are compliant with direct searches for t' 's, b' 's and exotic states with charge $5/3$.

the incorrect SM masses or fail direct t' and b' tests) are suppressed with respect to the SM expectation (shown by the vertical black line).

Using the same scan points, I plot a histogram in Figure 5.7 that shows the χ^2 value, calculated using Equation 5.9. As for Figure 5.6, the results are presented a histogram, indicating the number of scan points that fell into each binned range of χ^2 values. There are eight degrees of freedom (four channels each from ATLAS and CMS) and the χ^2 value of the SM is shown in comparison using a horizontal black line. One can see from this plot that for benchmarks with higher values of the compositeness scale f , the points in the parameter scan were mostly a better fit to data than the SM.

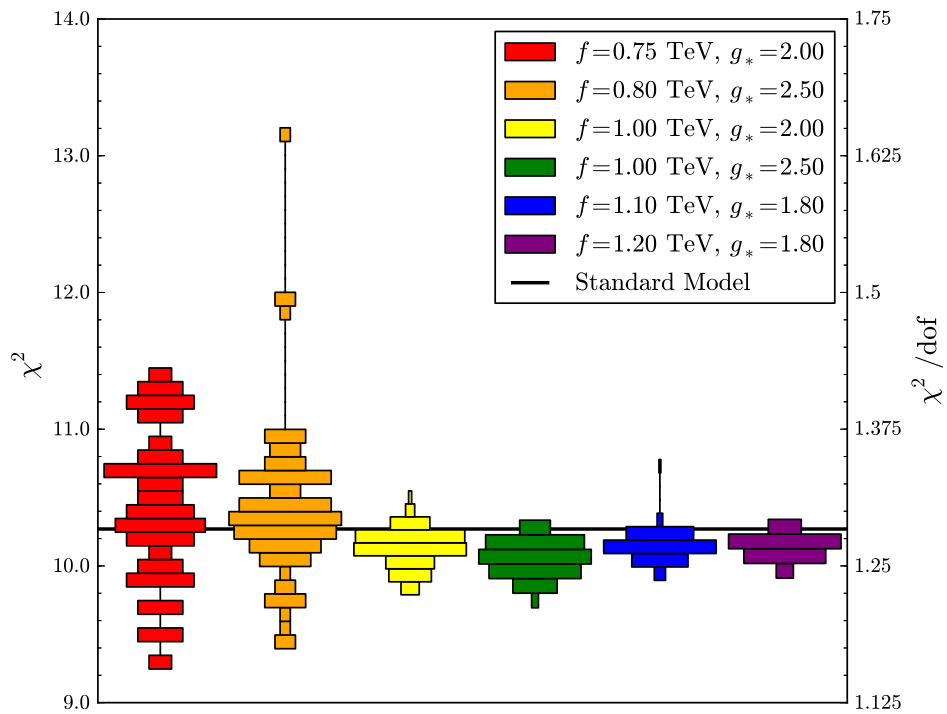


Figure 5.7: The χ^2 fit (as described in the text) in the 4DCHM for all benchmark points in f and g_* . All points generated here are compliant with direct searches for t' s, b' s and exotic states with charge $5/3$.

5.7 Conclusions

In this chapter we have seen that the hierarchy problem can be solved by requiring the Higgs boson to be a pseudo-Nambu-Goldstone boson of a global symmetry spontaneously broken by the strong dynamics of a new fermionic sector. Concentrating on a particular variant of this class of models, the 4DCHM, I showed how we constrained the model's parameter space using direct heavy quark search data. With the troublesome points excluded, we saw that the Higgs couplings were generally very SM-like for a broad scan over the parameter space of a wide range of benchmarks. Indeed, we saw in Figure 5.7 that most points in our scan (particularly for points with a higher compositeness scale f) fitted the LHC data better than the SM hypothesis.

Chapter 6

Technicolor

As discussed in Section 5.1, one of the main motivating factors for searching for physics beyond the Standard Model is the hierarchy problem. This is the unnaturally sensitive (quadratic) dependence of the self-coupling of the Higgs boson to the scale of new physics, which forces one to “fine tune” apparently independent Lagrangian parameters to an extraordinary degree of precision in order to lead to phenomenologically reasonable predictions for physical quantities such as the W mass.

The most well-known solution to this problem is supersymmetry (SUSY), where the Poincaré symmetry of the SM Lagrangian is enlarged, requiring the introduction of a new set of particles. These new “super particles” run in loops in such a way as to cancel the cutoff dependence in the SM that necessitated the fine-tuning.

Another solution, called “Technicolor” (TC), was proposed by Weinberg [91] and Susskind [92] in the 1970s, and it is inspired by spontaneous symmetry breaking that is known to occur in QCD. In this chapter I describe a project I conducted with collaborators (published in [5]) in which we investigated a selection of Technicolor theories to determine how well they account for the recent discovery of the Higgs. Sections 6.1 and 6.2 below describe how Technicolor theories can explain the masses of gauge bosons and fermions and Section 6.3 discussed how the Higgs scalar observed at the LHC can be accommodated. Section 6.4 discusses the effective Lagrangian framework used to parameterise the various TC models considered, whilst Section 6.5 details the statistical procedure used to obtain the exclusion plots in Section 6.5.1. Finally, conclusions for this project are given in Section 6.7.

6.1 Electroweak gauge boson masses through strong dynamics

It is an intriguing fact that even without the Higgs boson, the weak vector bosons would acquire mass through QCD effects. Consider, first, just the QCD Lagrangian with two quark flavours u and d and no quark mass terms. In addition to the $SU(3)_c$ gauge symmetry, the Lagrangian has (in addition to other global symmetries) a global $SU(2)_L \times SU(2)_R$ “chiral symmetry” that acts on the left- and right-handed components of the quarks as

$$\begin{pmatrix} u'_L \\ d'_L \end{pmatrix} = U_L \begin{pmatrix} u_L \\ d_L \end{pmatrix}, \quad \begin{pmatrix} u'_R \\ d'_R \end{pmatrix} = U_R \begin{pmatrix} u_R \\ d_R \end{pmatrix}, \quad (6.1)$$

where U_L and U_R are independent $SU(2)$ matrices. This symmetry is certainly not manifest in the interaction of free quarks and gluons at high energies. It is not evident at low energies either, although in this regime the picture is more complicated. Because the QCD coupling constant α_s *increases* at lower and lower energies, at a scale (known as Λ_{QCD}) the coupling becomes greater than unity. Below this scale, the quarks and gluons are tightly bound into “hadrons” (in a phenomenon known as infrared slavery). It becomes useless to describe the physics in terms of quarks and gluons and so one makes use of a low-energy effective theory involving the composite hadronic fields such as the pions and the nucleons; Λ_{QCD} furnishes the cutoff of this effective theory.

If the symmetry is not manifest in free quark or hadron interactions then it is either explicitly broken, i.e. adding chiral symmetry-breaking terms to the Lagrangian or it is spontaneously broken. This breaking could be provided by the Higgs field and its spontaneous acquisition of a vev, inducing chiral symmetry-breaking Dirac mass terms. However, this cannot be the only source of chiral symmetry breaking or the proton would have a mass of approximately $3m_u$, where m_u is the quark mass as dictated by the u -type Yukawa coupling. In reality, the proton is much heavier than this.

The resolution to this problem is the hypothesis (inspired by the BCS theory of superconductivity) that the strong interactions between quarks somehow arrange that the composite field $\bar{q}_L q_R$ has a non-zero vacuum expectation value. This condensate $\langle \bar{q}_L q \rangle$ breaks the chiral symmetry, leaving an unbroken $SU(2)_V$ subgroup of $SU(3)_L \times SU(2)_R$. There are three broken symmetry generators and so, by Goldstone’s theorem, there are three independent massless excitations of the (u, d, g) system of fields (g is the gluon field): these “Goldstone bosons” correspond to three massless pions: bound states with same quantum numbers as a quark-antiquark pair.

If we now enlarge the Lagrangian to include the electroweak gauge interactions, we see that the global part of the $SU(2)_W \times U(1)_Y$ gauge group is a subgroup of the global $SU(2)_L \times SU(2)_R$. We know the EW gauge group must be broken by the vacuum, leaving a remnant $U(1)_{\text{EM}}$ group, and the global part of this is also a subgroup of the unbroken

$SU(2)_V$ part of the chiral symmetry. Therefore, each pion corresponds to a gauge degree of freedom that can be eaten by the EW gauge bosons to give them their longitudinal degrees of freedom.

It seems that QCD then provides a mechanism for EWSB without ever needing to introduce a Higgs boson. The problem is that the mass of the weak bosons that would result from this mechanism alone would be around 2000 times too small.

If we have another source of EWSB at a higher scale (such as the Higgs field acquiring a vev), there are two “pions” corresponding to each broken generator: one being a bound state of the strongly-interacting quarks and the other being (for example) a component of the scalar Higgs field. These “pions” mix, one linear combination being eaten by the weak bosons and the other being the physical pion. In reality, because of the large difference between the QCD scale and the EW scale, the mixing is small with the physical pion being formed almost completely by the QCD bound state and the eaten Goldstone bosons being from the (in this example) Higgs field.

As we can see, the reason that QCD fails to be a good mechanism for EWSB is because the scale at which it becomes strongly coupled (the confining scale) is too low. It is very important to note that this scale is not put in by hand, but rather is a result of the running of the strong coupling α_s which is due to the dynamics of the theory. The confining scale can be raised by increasing the strength of the strong coupling.

Technicolor, then, postulates that there exists a new sector of quarks (“techniquarks”) that have a new technigauge symmetry. The techniquarks strongly interact via the technigluons associated with the technigauge group. The strength of this new Technicolor interaction is postulated to be stronger than QCD such that the theory becomes confining and breaks the chiral symmetry breaking in the techniquark sector at around the EW scale $v = 246$ GeV. The chiral symmetry breaking produces a ‘technipion’ Goldstone boson for each broken generator. Some or all of the techniquarks are gauged under the EW group and so, when chiral symmetry is broken, the corresponding Goldstone bosons are “eaten” by the weak bosons, giving the latter mass.

6.2 Fermion masses and Extended Technicolor

We have seen in the previous section how the electroweak gauge bosons can be given mass through EWSB by strong dynamics. The question remains: how do we give mass to the SM fermions? One solution is Extended Technicolor (ETC) in which the technigauge group is extended so the TC gauge group G_{TC} is a subgroup of the ETC gauge group G_{ETC} . The gauge bosons associated with this group consist of the technigluons, plus additional vector bosons. It is imagined that the ETC charge assignments are such that elements of G_{ETC} transform SM fermions into techniquarks and vice versa. One further

postulates that the ETC group spontaneously breaks to G_{TC} and that the resultant Goldstone bosons are eaten by some of the ETC gauge bosons, giving them mass. The scale Λ_{ETC} associated with this symmetry breaking (the mechanism of which we left unspecified in our analysis described below) and therefore the mass M_{ETC} of the ETC gauge bosons, is assumed to be considerably larger than Λ_{TC} . As Λ_{TC} is approached from above, interactions of two SM fermions with two technifermions via a massive ETC gauge boson can be approximated by four fermion interactions with couplings proportional to $1/M_{ETC}$, in the spirit of Fermi's theory of beta decay being a low-energy approximation to interactions involving heavy W bosons. As the energy scale drops further, the techniquarks become tightly bound around Λ_{TC} . The four-fermion vertices then consist at low energies of two SM fermions coupled to a condensate, inducing mass terms for the SM fermions.

When trying to find a suitable ETC gauge group and choice of representations of the SM fermions and techniquarks, one generically finds that flavour-changing neutral currents (FCNCs) can be induced by the massive ETC gauge bosons. We know from experiment that FCNCs are very rare, which implies that M_{ETC} must be very large (as high as 1000 TeV) in order to evade experimental bounds from, for example, kaon mixing. On the other hand, M_{ETC} must be approximately 15 TeV in order to give the SM the correct masses, so there is a severe tension.

The prediction for M_{ETC} coming from the SM fermion mass requirement makes the assumption that the TC coupling constant α_{TC} is weak between Λ_{TC} and Λ_{ETC} . This is motivated by QCD, where it is observed that the coupling quickly runs to become weak not far above Λ_{QCD} . A solution to the tension in the value of Λ_{ETC} is to arrange for the running of α_{TC} to be very small between Λ_{TC} and Λ_{ETC} so that α_{TC} remains large. Such near-conformal running is called “walking” dynamics. Walking Technicolor theories then allow for Λ_{ETC} to be large enough to evade FCNC constraints whilst still providing the observed SM fermion masses.

There is the question then of how to arrange the walking dynamics. This is done by judicious choice of the technigauge group and the action of the latter on the techniquarks. It is known that the beta function for a coupling receives opposite-sign contributions from gluon loops and quark loops. In confining theories, the “anti-screening” gluon contributions dominate over the screening quark contributions. One can then increase the running by increasing N_{TC} (assuming the technigauge group is $SU(N_{TC})$). Conversely, if the techniquarks transform under the fundamental representation of G_{TC} then one can reduce the running, hopefully to a “walk”, by increasing the number of techniflavours.

The problem with this approach is that a large number of techniflavours leads (at least in a naive calculation) to a large value of the EW Peskin-Takeuchi S parameter, in contradiction with EW precision tests performed at LEP and elsewhere. There are possible solutions to this problem such as “minimal” walking Technicolor models where

the techniquarks transform under higher representations of G_{TC} , effectively increasing the screening contribution to beta function without the corresponding increase in the S parameter. Other solutions also exist, and some are examined in more detail later in this chapter.

6.3 The Technicolor Higgs

We have seen that Technicolor is a natural theory of EWSB (natural because it does not include fundamental scalars) that can give masses to the EW gauge bosons and (via ETC) SM fermions. However, there is no “left-over” scalar degree of freedom in contrast to the SM Higgs model. This is why Technicolor models are often described as “Higgsless”. The recent discovery of a (most probably) scalar resonance with couplings consistent with the SM Higgs would seem to pose an experimental problem for Technicolor.

A way out can be seen by looking again at QCD. Although there are no fundamental scalars, one can have scalar *resonances* of quark-antiquark bound states (mesons). The lightest such state (other than the pions, which play special roles as Goldstone bosons) is the σ meson, also known as $f_0(500)$ whose mass is known to be around 500 MeV. In QCD-like TC theories, the mass of the corresponding Higgs-candidate technimeson can be estimated from the QCD σ mass by scaling arguments. Unfortunately, these would predict $m_H \sim 1$ TeV which is too heavy to explain the observed 125 GeV resonance.

There are ways to accommodate a light Higgs-like particle (a techni-Higgs) in Technicolor theories. Walking Technicolor provides one possible solution in that the approximately conformal dynamics must be accompanied by a light pseudo-Nambu-Goldstone boson which could be the Higgs [93, 94, 95, 96]. One could also explain the lightness of the Higgs using a see-saw mechanism [97].

In the project described in the sections below, we assumed the existence of a suitably light techni-Higgs and we were able to show that the couplings with SM particles could be expected to be SM-Higgs-like and consistent with the latest LHC Higgs search data.

6.4 The effective Lagrangian and the loop couplings

As for the 4DCHM, it is possible to parameterise the couplings of the (composite) techni-Higgs with the effective Lagrangian given in Equation 3.30. We only considered TC theories possessing custodial symmetry, ensuring a SM-like ρ parameter. This means that the modifications of the W and Z couplings must be equal, i.e., in Equation 3.30,

$$c_W = c_Z \equiv c_{II}, \quad (6.2)$$

where the variable c_Π is chosen to be reminiscent of the coupling of pions to the σ boson in QCD. By arguing in analogy to QCD, as described in [5], it is possible to estimate the value of c_Π , and it is found to be around $c_\Pi = 1$. Nevertheless, in this analysis we left c_Π as a free parameter to account for deviations from QCD-like behaviour. The values of the fermion coupling modifications c_f depend on the model of Extended Technicolor (ETC) that is chosen, to give fermions mass. Again, it is possible to argue that one should expect $c_f \approx 1$, but we leave the parameters free. In fact, because the current Higgs data are only sensitive to c_t (through the top quark triangle loop in gluon-gluon fusion), and c_b and c_τ through the $H \rightarrow b\bar{b}$ and $H \rightarrow \tau^+\tau^-$ channels respectively, we set the other fermion couplings to zero. With these conditions, Equation 3.30 becomes

$$\begin{aligned} \mathcal{L}_H = & \frac{2m_W^2}{v} c_\Pi HW_\mu^- W^{+\mu} + \frac{2m_Z^2}{v} c_\Pi HZ_\mu Z^\mu - \sum_{f=t,b,\tau} \frac{m_f c_f}{v} H \bar{f} f \\ & + \frac{g_{Hgg}}{v} HG_{\mu\nu}^a G^{a\mu\nu} + \frac{g_{H\gamma\gamma}}{v} HF_{\mu\nu} F^{\mu\nu}, \end{aligned} \quad (6.3)$$

We estimated the loop couplings g_{Hgg} and $g_{H\gamma\gamma}$ by adding a term

$$\mathcal{L}_{HFF} = - \sum_F \frac{m_F}{v} H \bar{F} F \quad (6.4)$$

to Equation 6.3, where the sum is over each of the new technifermions F in the particular TC model under study. This new extended Lagrangian $\mathcal{L}_H + \mathcal{L}_{HFF}$ is a ‘‘hybrid’’ model, in that it contains both the composite techni-Higgs, a bound state of technifermions and technigluons, and also the constituent technifermions F themselves. Such hybrid models have been considered before [98, 99, 100, 101] in the context of QCD. The coupling is proportional to the dynamical mass of the technifermion, and so it is SM-like. The dynamical technifermion mass can be estimated using the Pagels-Stokar relation

$$v^2 = \frac{d(R_{\text{TC}})N_{\text{TD}}}{4\pi^2} m_F^2 \log \frac{\Lambda^2}{m_F^2}, \quad (6.5)$$

with $\Lambda \sim 4\pi F_\Pi = 4\pi v/\sqrt{N_{\text{TD}}}$, where N_{TD} is the number of electroweak doublets of technifermions in the model and $d(R_{\text{TC}})$ is the dimension of the representation R_{TC} of the Technicolor gauge group under which the technifermions transform. When the coefficient $d(R_{\text{TC}})N_{\text{TD}}$ is not too large, the solution for m_F is typically of the order of hundreds of GeV.

The calculation of g_{Hgg} and $g_{H\gamma\gamma}$ can be organised into an expansion in $1/d(R_{\text{TC}})$. The leading order (‘‘Hartree-Fock’’) contribution to g_{Hgg} by the TC sector is a triangle loop of techniquarks, exactly analogous to the SM top quark loop. There is a similar diagram contributing to $g_{H\gamma\gamma}$, which will also involve TC-neutral, yet electromagnetically-charged, new leptonic particles appearing in some TC models.

Higher order corrections in $1/d(R_{\text{TC}})$ would involve diagrams with loops of technipions and other bound Technicolor states in addition to the constituent techniquarks. These corrections depend on how the inherently non-perturbative TC dynamics is modelled in the hybrid theory and so we accounted for these subdominant contributions by multiplying the Hartree-Fock estimates for g_{Hgg} and $g_{H\gamma\gamma}$ by form factors a_{Hgg} and $a_{H\gamma\gamma}$ respectively.

There is an important subtlety when computing the usual W contribution to $g_{H\gamma\gamma}$. The standard expression for this contains contributions from the transverse and longitudinal components of the W . In TC theories, the longitudinal components are in fact the eaten technipions and their contribution has already been computed in the hybrid model (incorporated in our form factor $a_{H\gamma\gamma}$). As such we must be careful not to double count this contribution. In the Landau gauge, the Goldstone bosons correspond to the longitudinal W 's. Computing the Goldstone contribution on its own and comparing it to the complete expression [102] reveals that one must subtract 2 from $F_1(\tau_W)$ (given by Equation 3.37b) to remove the double-counting.

Using Equation 3.40, the gluon and photon couplings can then be found in this picture to be

$$g_{Hgg} = \frac{\alpha_s}{16\pi} \left| \sum_q c_q^{\text{TC}} F_{1/2}(\tau_q) + a_{Hgg} d(R_{\text{TC}}) \sum_{F \in \text{QCD}} F_{1/2}(\tau_F) \right|, \quad (6.6a)$$

$$g_{H\gamma\gamma} = \frac{\alpha}{8\pi} \left| c_{\text{H}} [F_1(\tau_W) - 2] + \sum_f c_f N_c^f Q_f^2 F_{1/2}(\tau_f) + a_{H\gamma\gamma} d(R_{\text{TC}}) \sum_F N_c^F Q_F^2 F_{1/2}(\tau_F) \right|, \quad (6.6b)$$

where N_c^f and N_c^F are colour multiplicity factors for the flavour f and the techniflavour F , respectively, and the second sum in Eq. (6.6a) is over coloured techniflavours only. Logically, the dimension of the representation F , $d(R_{\text{TC}})$, should be inside the sums over F , because different techniflavours could conceivably belong to different representations. However, in all the TC scenarios considered below, the technifermions all transform under a single TC gauge group representation and so it is safe to take the factor $d(R_{\text{TC}})$ out of the sum.

It is possible to estimate the $a_{H\gamma\gamma}$ form factor by comparing with QCD. This analogous decay in QCD would be $\sigma \rightarrow \gamma\gamma$. In the hybrid model, this width would be given by

$$\Gamma_{\sigma \rightarrow \gamma\gamma} = \frac{\alpha^2 (\text{Re}(m_\sigma))^3 a_{\sigma\gamma\gamma}^2}{256\pi^3 f_\pi^2} \left| 3 \left(\frac{2}{3} \right)^2 F_{1/2} \left(\frac{4m_u^2}{(\text{Re}(m_\sigma))^2} \right) + 3 \left(-\frac{1}{3} \right)^2 F_{1/2} \left(\frac{4m_d^2}{(\text{Re}(m_\sigma))^2} \right) \right|^2, \quad (6.7)$$

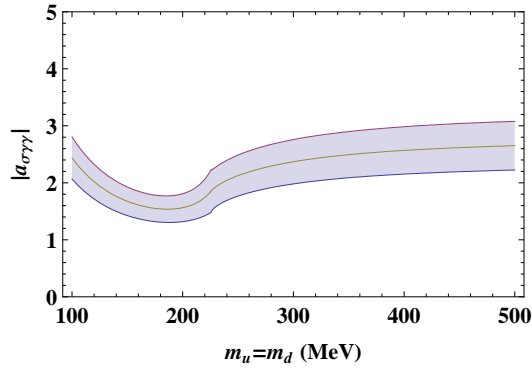


Figure 6.1: Estimate of $|a_{\sigma\gamma\gamma}|$ ($\pm 1\sigma$) from the $\Gamma_{\sigma\rightarrow\gamma\gamma}$ partial width, as a function of the constituent u and d quark masses.

where f_π is the QCD pion decay constant (the QCD equivalent of $F_\Pi = v$ in Technicolor theories) and where m_u and m_d are the *constituent* quark masses. The leading order contribution in $1/N_c$ is shown, with the higher order corrections being encoded in the form factor $a_{\sigma\gamma\gamma}$. We can compare this expression with the experimentally-measured partial decay width. The Particle Data Group [103] reports the global average of $\Gamma_{\sigma\rightarrow\gamma\gamma}$ to be 2.79 ± 0.86 keV and also gives $\text{Re}(m_\sigma) = 451.7 \pm 13.4$ MeV. Our expression for $\Gamma_{\sigma\rightarrow\gamma\gamma}$ is a function of the constituent quark masses. Setting these equal to each other and tuning $a_{\sigma\gamma\gamma}$ to fit the experimental value for $\Gamma_{\sigma\rightarrow\gamma\gamma}$ yields Figure 6.1. For a sensible value of $m_u = m_d = 300$ MeV,

$$|a_{\sigma\gamma\gamma}| = 2.37 \pm 0.39. \quad (6.8)$$

This result is only for QCD, but it provides an estimate of $a_{H\gamma\gamma}$ in Technicolor theories with similar dynamics.

6.5 Statistical Procedure

As described in Section 5.5, the normal method for confronting a beyond-the-Standard-Model theory with Higgs data is to make use of the best-fit values for the signal enhancement factors in each available final state Y and cut category c . When one forms the χ^2 test statistic

$$\chi^2(\boldsymbol{\mu}) = \sum_{i,c,Y} \frac{(\mu_Y^{c,i} - \hat{\mu}_Y^{c,i})^2}{\Delta(\mu_Y^{c,i})^2} \quad (6.9)$$

using the experimental collaborations' best-fit values of the enhancement factors ($\hat{\mu}$) and the given 1σ uncertainties $\Delta(\mu)$, one has the problem of how to calculate the predictions

for the signal enhancements within the model under test. In terms of the model cross-sections, these are given by Equation 5.7, i.e.

$$\mu_Y^c = \sum_X \tilde{\sigma}_X R_{XY}^{c, \text{SM}} \times \frac{\tilde{\Gamma}_Y}{\tilde{\Gamma}_{\text{tot}}}, \quad (5.7)$$

where the cross-section for gluon-gluon fusion, vector boson fusion, associated W and Z production and associated $t\bar{t}$ production, in SM units, are given in terms of the effective Lagrangian parameters defined in Equation 6.3 by, respectively,

$$\tilde{\sigma}_{\text{ggF}} = (g_{Hgg}/g_{Hgg}^{\text{SM}})^2, \quad (6.10a)$$

$$\tilde{\sigma}_{\text{VBF}} = \tilde{\sigma}_{WH} = \tilde{\sigma}_{ZH} = c_{\text{II}}^2, \quad (6.10b)$$

$$\tilde{\sigma}_{t\bar{t}H} = c_t^2. \quad (6.10c)$$

Note that the VBF cross-section enhancement take a particularly simple form due to the equality of the W and Z enhancements. The partial widths in SM units are

$$\tilde{\Gamma}_{bb} = c_b^2, \quad (6.11a)$$

$$\tilde{\Gamma}_{\tau\tau} = c_\tau^2, \quad (6.11b)$$

$$\tilde{\Gamma}_{cc} = c_c^2, \quad (6.11c)$$

$$\tilde{\Gamma}_{ZZ} = \tilde{\Gamma}_{WW} = c_{\text{II}}^2, \quad (6.11d)$$

$$\tilde{\Gamma}_{gg} = (g_{Hgg}/g_{Hgg}^{\text{SM}})^2, \quad (6.11e)$$

$$\tilde{\Gamma}_{\gamma\gamma} = (g_{H\gamma\gamma}/g_{H\gamma\gamma}^{\text{SM}})^2, \quad (6.11f)$$

and the total width enhancement is given by

$$\tilde{\Gamma}_{\text{tot}} = \sum_{f=b,c,\tau} \tilde{\Gamma}_{ff} \text{BR}_{ff}^{\text{SM}} + \sum_{V=W,Z,\gamma,g} \tilde{\Gamma}_{VV} \text{BR}_{VV}^{\text{SM}} + \tilde{\Gamma}_{\text{else}} \text{BR}_{\text{else}}^{\text{SM}}, \quad (6.12)$$

where $\text{BR}_{\text{else}}^{\text{SM}} \simeq 0.132\%$. Since the latter is a small fraction, instead of computing all remaining two- and multi-body decay channels, we shall simply take $\tilde{\Gamma}_{\text{else}} = 1$ and allow for little uncertainty in the final result.

A problem is that one does not generally know the efficiencies of experimental cuts, and so the $R_{XY}^{c, \text{SM}}$ ratios in given in Equation 5.8 are unknown. Another drawback of the procedure is that it neglects correlations between the systematic errors.

To alleviate the first problem, and ameliorate the second, I adopted a method, used for example in Refs. [81, 78], that makes use of the *two-parameter* fits ATLAS and CMS have performed for each Higgs decay mode. These are presented in Figure 2 of [21] and Figure 4 of [22] as 68% (and also 95% in the case of ATLAS) confidence level regions in the two-dimensional parameter space. I reproduce the contours as the solid lines in Figure 6.2 here for reference. The sharp cutoff in the $H \rightarrow ZZ^* \rightarrow 4\ell$ contour for

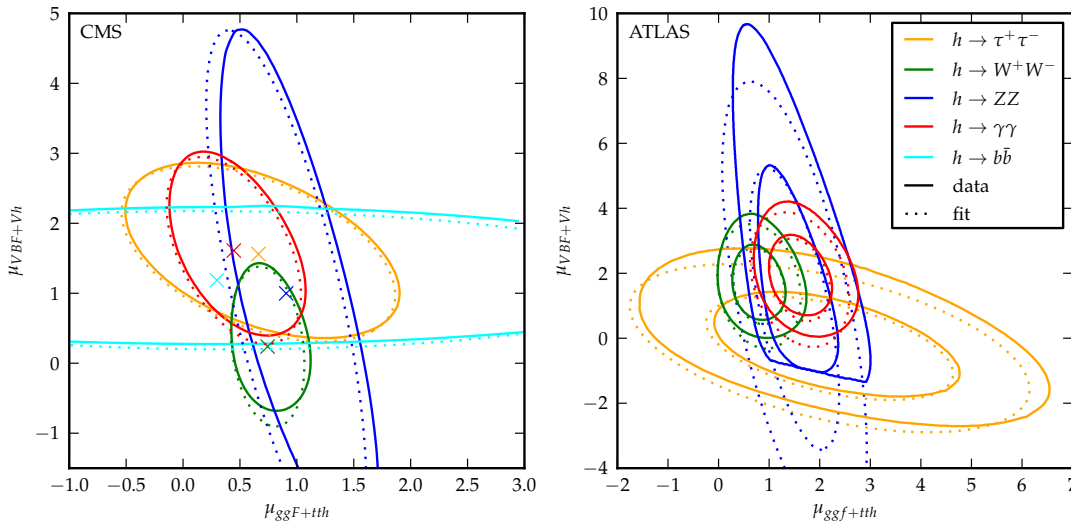


Figure 6.2: 68% CL (and 95% CL in the ATLAS case) contours, comparing our fit (dotted lines) to official ATLAS and CMS fits.

the ATLAS data is due to the restriction that the likelihood must be zero anywhere in the parameter space where the total number of expected signal+background events is negative.

The collaborations perform the two-parameter fits in the following way. For a particular decay channel Y , they postulate a model identical to the SM except for factors enhancing the production cross-sections. One factor, μ_{Yg} enhances both the gluon fusion (ggH) and associated top production (ttH) mechanisms uniformly and the other, μ_{YV} , enhances the vector boson fusion (VBF) and associated vector boson (VH) production. Assuming identical enhancements of ggH and ttH processes may be justified by the comparatively small SM ttH cross-section,¹ while equating the VBH and VH enhancements is reasonable because custodial symmetry is preserved to good accuracy.²

The next step is to form the likelihood function described in Section 3.4.5: $\mathcal{L}(\boldsymbol{\mu}_Y, \boldsymbol{\theta})$, i.e. a probability density function for observing a particular set of data, given a particular value of $\boldsymbol{\mu}_Y = (\mu_{Yg}, \mu_{YV})$, and the various nuisance parameters $\boldsymbol{\theta}$ that account for the systematic errors. From this, the profiled log likelihood ratio test statistic

$$q_{\boldsymbol{\mu}_Y} = -2 \ln \left(\frac{\mathcal{L}(\boldsymbol{\mu}_Y, \hat{\boldsymbol{\theta}}_{\boldsymbol{\mu}_Y})}{\mathcal{L}(\hat{\boldsymbol{\mu}}_Y, \hat{\boldsymbol{\theta}})} \right) \quad (6.13)$$

is formed, where $\hat{\boldsymbol{\theta}}_{\boldsymbol{\mu}_Y}$ is the value of $\boldsymbol{\theta}$ that maximises the likelihood for a particular fixed $\boldsymbol{\mu}_Y$, and $\hat{\boldsymbol{\theta}}$ and $\hat{\boldsymbol{\mu}}_Y$ are global maximum-likelihood values.

¹Although in e.g. the OFTC model, new coloured fermions enhance the ggH production cross-section while not affecting the ttH cross-section.

²The presence of resonances could change this picture due to the different kinematics in the channels.

If we assume that the two-dimensional parameterisation above is true for some point in the parameter space, Wilks's theorem [104], as discussed in [105], can be used to show that q_{μ_Y} is distributed as a χ^2 distribution with two degrees of freedom. If the probability density function for this distribution is denoted by $f_{\chi^2_2}(q_{\mu_Y})$ (where the subscript 2 signifies the number of degrees of freedom) then the p -value for a particular choice of μ_Y is then given by

$$p = \int_{q_{\mu_Y}^{\text{obs}}}^{\infty} f_{\chi^2_2}(q_{\mu_Y}) dq_{\mu_Y}. \quad (6.14)$$

The contour plots presented by ATLAS and CMS are effectively plots of $q_{\mu_Y}^{\text{obs}}$ as a function of μ_Y . The best-fit point has $q_{\mu_Y}^{\text{obs}} = 0$ and the points on the 68% CL contour (corresponding to $p = 0.32$) have $q_{\mu_Y}^{\text{obs}} \approx 2.3$.

If the data upon which the fit are based are distributed as a multivariate Gaussian (and this is a good approximation for numbers of events greater than around 10) then the test statistic takes the familiar ‘‘chi square’’ form, allowing for correlations in the errors:

$$q_{\mu_Y} \approx (\mu_Y - \hat{\mu}_Y)^T \sigma_Y^{-1} (\mu_Y - \hat{\mu}_Y). \quad (6.15)$$

Suppressing the Y index, the covariance matrix is conventionally parameterised as

$$\sigma = \begin{pmatrix} \Delta_g^2 & \rho \Delta_g \Delta_V \\ \rho \Delta_g \Delta_V & \Delta_V^2 \end{pmatrix}, \quad (6.16)$$

where Δ_g and Δ_V are the standard deviations in the μ^g and μ^V parameters and ρ is the correlation coefficient.

Let us assume this bivariate Gaussian form and tune the covariance matrix to fit the 68% CL contours in Figure 6.2. The reproductions of the 68% CL (and, for ATLAS, 95% CL) contours, shown with dashed lines, are in good agreement with the official contours. We can combine the likelihood functions by simply multiplying, which corresponds to adding the test statistics. This gives

$$q_{\mu} = \sum_{i,Y} (\mu_Y^i - \hat{\mu}_Y^i)^T \sigma_{Y,i}^{-1} (\mu_Y^i - \hat{\mu}_Y^i), \quad (6.17)$$

where again the index $i \in \{\text{ATLAS, CMS}\}$. For ATLAS, $Y \in \{\gamma\gamma, W^-W^+, ZZ, \tau^-\tau^+\}$ and for CMS, $Y \in \{\gamma\gamma, W^-W^+, ZZ, \tau^-\tau^+, b\bar{b}\}$. Each channel contributes two degrees of freedom, μ_{Yg} and μ_{YV} , to the test statistic and, with four channels from ATLAS and five from CMS, q_{μ} will obey a χ^2 distribution with $N_{\text{DOF}} = 18$ degrees of freedom.

We now have all the information to calculate the p -value for a particular choice of μ : the probability density function for q_{μ} is a χ^2 distribution for 18 degrees of freedom and the value of q_{μ}^{obs} as a function of μ is found by fitting the contours in Figure 6.2.

All of the Technicolor models considered here obey custodial symmetry and so are contained within the 18-parameter model described above. A particular point in a model's parameter space can be compared with experiment by calculating the 18 μ parameters. Unless the models explicitly incorporate details about the experimental apparatus, it will predict the same enhancement factors in a particular channel for both ATLAS and CMS. The enhancement factors in the two-parameter fit scenario are defined simply as

$$\mu_{Yg} \equiv \tilde{\sigma}_{\text{ggF}} \times \tilde{\Gamma}_{YY} \times \tilde{\Gamma}_{\text{tot}}^{-1} \quad (6.18)$$

$$\mu_{YV} \equiv \tilde{\sigma}_{\text{VBF}} \times \tilde{\Gamma}_{YY} \times \tilde{\Gamma}_{\text{tot}}^{-1} \quad (6.19)$$

and in terms of the parameters defined in Equation 6.3, these evaluate to

$$\mu_Y^g = \left(\frac{g_{Hgg}}{g_{Hgg}^{\text{SM}}} \right)^2 \times c_Y^2 \times \tilde{\Gamma}_{\text{tot}}^{-1} \quad (6.20)$$

$$\mu_Y^V = c_{\text{II}}^2 \times c_Y^2 \times \tilde{\Gamma}_{\text{tot}}^{-1} \quad (6.21)$$

for $Y \in \{W^+W^-, ZZ, b\bar{b}, \tau^+\tau^-\}$ and

$$\mu_{\gamma\gamma}^g = \left(\frac{g_{Hgg}}{g_{Hgg}^{\text{SM}}} \right)^2 \times \left(\frac{g_{H\gamma\gamma}}{g_{H\gamma\gamma}^{\text{SM}}} \right)^2 \times \tilde{\Gamma}_{\text{tot}}^{-1} \quad (6.22)$$

$$\mu_{\gamma\gamma}^V = c_{\text{II}}^2 \times \left(\frac{g_{H\gamma\gamma}}{g_{H\gamma\gamma}^{\text{SM}}} \right)^2 \times \tilde{\Gamma}_{\text{tot}}^{-1} \quad (6.23)$$

for the diphoton channel ($Y = \gamma\gamma$). The loop-level gluon and photon couplings $g_{H\gamma\gamma}$ and g_{Hgg} are defined in Equation 6.6 and the total width in SM units $\tilde{\Gamma}_{\text{tot}}$ is defined in (6.12).

With the quantities in Equations 6.20–6.23 calculated, q_{μ} can be found using Equation 6.17; if the value exceeds 28.8 (corresponding to a p -value of 0.05) then the point μ can be excluded at the 95% confidence level.

6.5.1 Assumptions and approximations

Here I briefly bring together and reiterate the various assumptions and approximations made in the above section. The method used relies on the two-parameter fit being a good parameterisation of the true physics. It certainly has enough flexibility to fit the existing data well, and most candidate models of new physics respect custodial symmetry, motivating identical VBF and VH enhancements as discussed above. This assumption, i.e. that the “two parameters per channel, per experiment” parameterisation is good, is required for Wilks's theorem to be applicable, and so any conclusions derived from this method should be interpreted in this way.

Advantageously, this method requires no assumptions about efficiency factors because, in the two-parameter fits, the collaborations make available purely theoretical variables with the experimental details unfolded. However, the assumption *is* being made that the cut *acceptances* for the BSM signals are identical to the SM values: this corresponds to the assumption that the differential cross-sections predicted by the new physics models have the same shape as in the SM – note that this is not true if e.g. a resonance is present in VH production [106, 107]. Another advantage of the method is that it includes correlations between systematic errors when combining the gluon fusion and vector production processes in the test statistic. However, correlations are necessarily neglected when summing over the final state channels Y .

Once the LHC resumes taking data, statistical uncertainties will be reduced and so systematic errors and their correlations will become more important. It will become increasingly useful, to theorists performing statistical tests of physics beyond the Standard Model, for the experimental collaborations to release more details, such as full likelihood functions in electronic format [108].

6.6 Results

Using the effective Lagrangian described in Equation 6.3, together with the definitions of the loop-suppressed Hgg and $H\gamma\gamma$ couplings defined in Equation 6.6, we see that a TC theory will have the six free parameters c_{Π} , c_t , c_b , c_{τ} , a_{Hgg} and $a_{H\gamma\gamma}$.³

Using the method described in the previous section, I wrote a Python program capable of calculating q_{μ} (using Equation 6.17) for a given set of model parameters. For TC models not involving QCD-coloured techniquarks, there is no sensitivity to a_{Hgg} and so the parameter space is five-dimensional; indeed, the only theory considered here with coloured techniquarks is one-family Technicolor (OFTC).

We considered several different TC models, the particle contents of which are shown in Table 6.1, and all of these models are contained within the five- (or six-, in the case of OFTC) parameter framework outlined above. Additionally, in Table 6.2, the approximate sizes of the TC contributions to the $H\gamma\gamma$ coupling are shown, together with estimates for the TC contribution to the Peskin-Takeuchi S parameter. These estimates are “naive” in the sense that they are calculated from the one-loop contribution to the appropriate vacuum polarisation diagram, using heavy technifermions F with masses much greater than the Z boson mass.

³There will also be a dependence on the dynamical masses m_F of the new TC fermions, but since this dependence is only manifest through the loop function $F_{1/2}(4m_F^2/m_H^2)$, and since the TC mass scale is significantly larger than m_H according to Equation 6.5, the loop function sits very close to its asymptotic value of $4/3$ and so the m_F dependence is weak.

TC theory	F	R_{TC}	Q	N_c^F
$SU(2)_F$ MWT (UMT)	U	2	1/2	1
	D	2	-1/2	1
$SU(2)_{\text{Adj}}$ MWT	U	3	$(y+1)/2$	1
	D	3	$(y-1)/2$	1
	N	1	$(-3y+1)/2$	1
	E	1	$(-3y-1)/2$	1
$SU(3)_{2S}$ MWT (NMWT)	U	6	1/2	1
	D	6	-1/2	1
$SU(3)_{\text{Adj}}$ MWT	U	8	1/2	1
	D	8	-1/2	1
WSTC (1D)/PGTC	U_i	\mathbf{N}_{TC}	1/2	1
	D_i	\mathbf{N}_{TC}	-1/2	1
WSTC (2D)	U	\mathbf{N}_{TC}	$(y+1)/2$	1
	D	\mathbf{N}_{TC}	$(y-1)/2$	1
	C	\mathbf{N}_{TC}	$-(y-1)/2$	1
	S	\mathbf{N}_{TC}	$-(y+1)/2$	1
OFTC	U	\mathbf{N}_{TC}	$(y+1)/2$	3
	D	\mathbf{N}_{TC}	$(y-1)/2$	3
	N	\mathbf{N}_{TC}	$(-3y+1)/2$	1
	E	\mathbf{N}_{TC}	$(-3y-1)/2$	1

Table 6.1: Extra particle content of TC theories under consideration, showing techniflavours (second column); the representation of the TC gauge group under which the techniflavours transform (third column); electric charges (fourth column); and QCD colour multiplicity (fifth column). Note that among these theories, only the OFTC model has new fermions carrying QCD colour charge.

Before choosing a particular model, it is possible to scan over the parameter space and find best-fit values of some of the parameters, i.e. values that minimise q_μ . These values are

$$\begin{aligned}
|c_\Pi| &= 1.05030, \quad |c_b| = 1.08747, \quad |c_\tau| = 1.03835, \\
|g_{H\gamma\gamma}/g_{H\gamma\gamma}^{\text{SM}}| &= 1.17921, \quad |g_{Hgg}/g_{Hgg}^{\text{SM}}| = 0.92234.
\end{aligned}
\tag{6.24}$$

Once a model is chosen, it is possible to infer the best-fit values of c_t and the form factors a_{Hgg} and $a_{H\gamma\gamma}$ from the above. For all theories considered here except OFTC, a_{Hgg} is relevant (there are no coloured technifermions). In this case, the best-fit value of c_t can be determined from $g_{Hgg}/g_{Hgg}^{\text{SM}}$. The remaining parameter $a_{H\gamma\gamma}$ is then tuned to give the correct value for $g_{H\gamma\gamma}/g_{H\gamma\gamma}^{\text{SM}}$.

For OFTC, the model is under-constrained by the current data: there are three remaining parameters, c_t , a_{Hgg} and $a_{H\gamma\gamma}$ constrained by only two quantities, $g_{Hgg}/g_{Hgg}^{\text{SM}}$ and

$g_{H\gamma\gamma}/g_{H\gamma\gamma}^{\text{SM}}$. To break this degeneracy, I set $c_t = 1$ and then determined a_{Hgg} from $g_{Hgg}/g_{Hgg}^{\text{SM}}$ and $a_{H\gamma\gamma}$ from $g_{H\gamma\gamma}/g_{H\gamma\gamma}^{\text{SM}}$.

In the subsections below I briefly describe each of the theories in Table 6.1 and show 95% CL exclusion contours in different planes of the parameter space, taking cross-sections through the best values of the parameters that are not plotted.

6.6.1 Minimal Walking Technicolor

Minimal models of Walking Technicolor (MWT) have a single weak doublet of technifermions (U, D). There are then choices to be made about the TC gauge group and the representations of the weak technidoublet under this group, as well as the weak hypercharge assignment for the electroweak doublet.

We considered three MWT models here, all of which use $SU(N_{\text{TC}})$ as the technigauge group, for differing numbers of technicolours, N_{TC} . The technifermion content of these models is shown in Table 6.1. Two of these MWT theories are from [94] and we call them $SU(2)_{\text{Adj}}$ MWT and $SU(3)_{2\text{S}}$ MWT. In $SU(2)_{\text{Adj}}$ MWT, the technigauge group is $SU(2)$ and the technidoublet transforms under the adjoint representation. This theory contains a topological Witten anomaly [109] that can be cured by adding a chiral lepton doublet transforming as a singlet under the technigauge group. The weak hypercharge assignment y for the techniquark doublet is unconstrained by anomaly cancellation as long as the technilepton doublet is has $Y = -3y$. The hypercharge constraints for all theories considered here are listed in Table 6.2.

The $SU(3)_{2\text{S}}$ MWT model (sometimes referred to as “next-to-minimal waking Technicolor” or NMWT) has the technidoublet transforming under a two-index, symmetric representation of the $SU(3)$ technigauge group. There is no Witten anomaly in this theory, but the technidoublet must be assigned a hypercharge of zero to ensure no gauge anomalies.

The third MWT theory we considered (called $SU(3)_{\text{Adj}}$ MWT) has the technidoublet transforming under the adjoint representation of the $SU(3)$ technigauge group. The hypercharge must also be zero.

For each of these models, I plot 2σ exclusion plots in the $(c_t, a_{H\gamma\gamma})$ plane, setting all of the other parameters to their best-fit values. $SU(3)_{2\text{S}}$ MWT (NMWT) is plotted in Figure 6.3, and $SU(2)_{\text{Adj}}$ MWT and $SU(3)_{\text{Adj}}$ MWT are plotted in Figure 6.4.

Let us look at the $SU(3)_{2\text{S}}$ MWT model in some more detail. Recalling Equation 6.6b, we can see that the contribution of the technifermions to the $H\gamma\gamma$ coupling is

$$d(R_{\text{TC}}) \sum_F N_c^F Q_F^2 F_{1/2}(\tau_F) \quad (6.25)$$

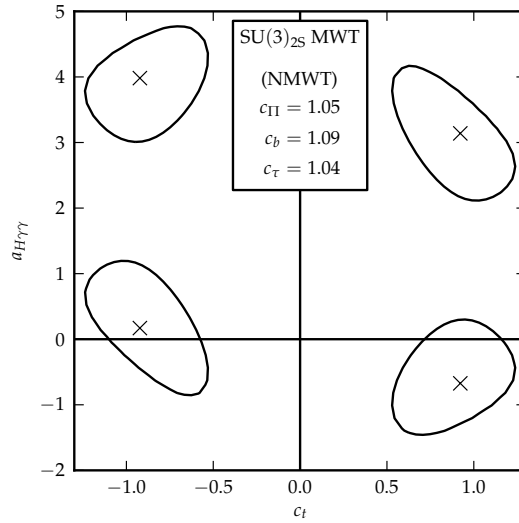


Figure 6.3: 2σ exclusion contours for the $SU(3)_{2S}$ MWT model (NMWT) in the $(c_t, a_{H\gamma\gamma})$ plane. The other parameters are fixed at their best-fit values, shown in the legend.

(which is then multiplied by the $a_{H\gamma\gamma}$ form factor). The approximate values for this factor for each of the TC models under study here are shown in Table 6.2. For $SU(3)_{2S}$ MWT, this factor is 4, and so (setting $c_{\Pi} \approx 1$) the $g_{H\gamma\gamma}$ coupling is

$$g_{H\gamma\gamma} \simeq \frac{\alpha}{8\pi} \left| 6 - \frac{16}{9}c_t - 4a_{H\gamma\gamma} \right|, \quad g_{H\gamma\gamma}^{\text{SM}} \simeq \frac{\alpha}{8\pi} \left| 8 - \frac{16}{9} \right| \simeq \frac{\alpha}{8\pi} 6. \quad (6.26)$$

Note the approximate value $F_1(\tau_W) \approx -8$ has been used (with 2 subtracted to account for the longitudinal modes) because, for the relatively small value of τ_W , the asymptotic value of $F_1(\tau) \rightarrow -7$ is not a good approximation. Let us take $|c_t| \approx 1$ as well and ask what value of $a_{H\gamma\gamma}$ would be required to render $g_{H\gamma\gamma} = a_{H\gamma\gamma}^{\text{SM}}$. For $c_t = 1$, the answer is $a_{H\gamma\gamma} \approx -0.5, 2.5$ (the two solutions are due to the modulus signs) and for $c_t = -1$, $a_{H\gamma\gamma} \approx 0.4, 3.5$. The $a_{H\gamma\gamma} \approx 2.5$ solution is reassuringly consistent with the expectation from QCD in Equation 6.8. This is plausible because $SU(3)_{2S}$ MWT has the same global symmetry as two-flavour QCD.

In comparison to $SU(3)_{2S}$ MWT, the $SU(3)_{\text{Adj}}$ MWT model (Figure 6.4, right) effectively has more technifermions running in the loop, due to the larger (by a factor of 4/3) representation, and we indeed see that the best-fit value of the form factor $a_{H\gamma\gamma}$ is reduced to compensate. In contrast, the $SU(2)_{\text{Adj}}$ MWT model (Figure 6.4, left) has half the number of effective techniquarks as $SU(2)_{2S}$, and the same charge assignments (shown in Table 6.2) as long as we set $y = 0$. There is an extra lepton doublet but there is still a corresponding increase in $a_{H\gamma\gamma}$. However, we can see that increasing the hypercharge y of the techniquark doublet increases the contribution of the technifermions, reducing the value of $a_{H\gamma\gamma}$, shown by the dotted and dashed contours.

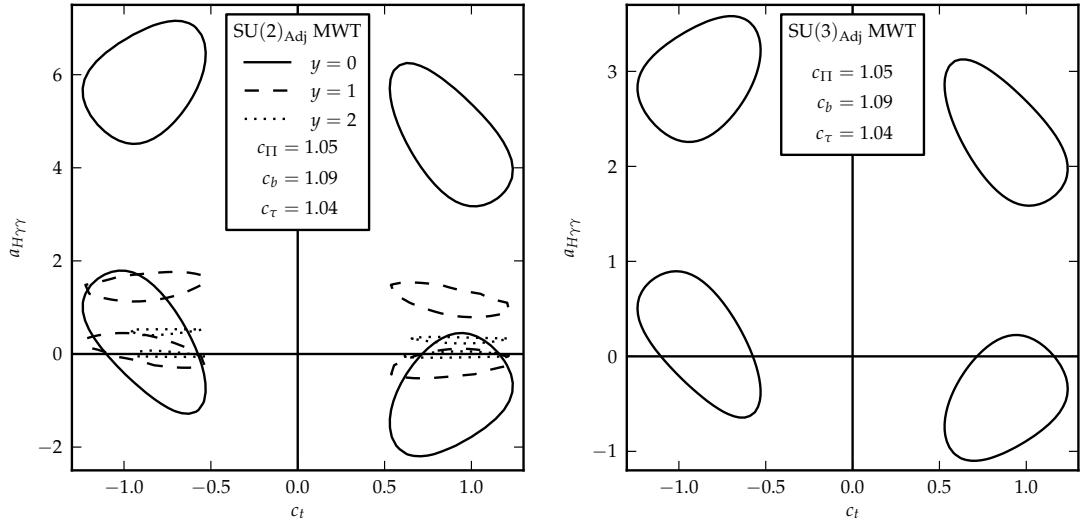


Figure 6.4: 2σ exclusion contours for the $SU(2)_{\text{Adj}}$ MWT model (left) and $SU(3)_{\text{Adj}}$ MWT model (right). For the $SU(2)_{\text{Adj}}$ MWT model we show three different hypercharge assignments: $y = 0$ (solid), $y = 1$ (dashed) and $y = 2$ (dotted). All other parameters are fixed at their best-fit values shown in the legend.

TC theory	$\sum_F N_c^F Q_F^2 F_{1/2}(\tau_F)$	S_{naive}
$SU(2)_F$ MWT (UMT)	$\simeq \frac{4}{3}$	$\frac{1}{3\pi}$
$SU(2)_{\text{Adj}}$ MWT	$\simeq 4 + 20y^2$	$\frac{1}{2\pi}$
$SU(3)_{2S}$ MWT (NMWT)	$\simeq 4$	$\frac{1}{\pi}$
$SU(3)_{\text{Adj}}$ MWT	$\simeq \frac{16}{3}$	$\frac{4}{3\pi}$
WSTC (1D)/PGTC	$\simeq \frac{2}{3}N_{TC}$	$\frac{N_{TC}}{6\pi}$
WSTC (2D)	$\simeq \frac{4}{3}N_{TC}(1 + y^2)$	$\frac{N_{TC}}{3\pi}$
OFTC	$\simeq \frac{8}{3}N_{TC}(1 + 3y^2)$	$\frac{2N_{TC}}{3\pi}$

Table 6.2: Loop factors for the TC contribution to $g_{H\gamma\gamma}$ and the value of the “naive” S parameter for the TC theories under consideration here.

6.6.2 Weinberg-Susskind, partially-gauged and two-scale Technicolor

In the original Weinberg-Susskind Technicolor, techniquarks were chosen to transform under the fundamental representation of the technigauge group $SU(N_{TC})$ and also the weak group $SU(2)_W$. In order to achieve walking dynamics, one would need the number of technidoublets N_D to be high. This could lead to an unacceptably-large value of the S (depending on the contributions from the extended Technicolor sector). One solution to this, “partially-gauged Technicolor” (PGTC) [110, 111, 112] has only one of the technidoublets possessing EW quantum numbers. Another solution is two-scale Technicolor

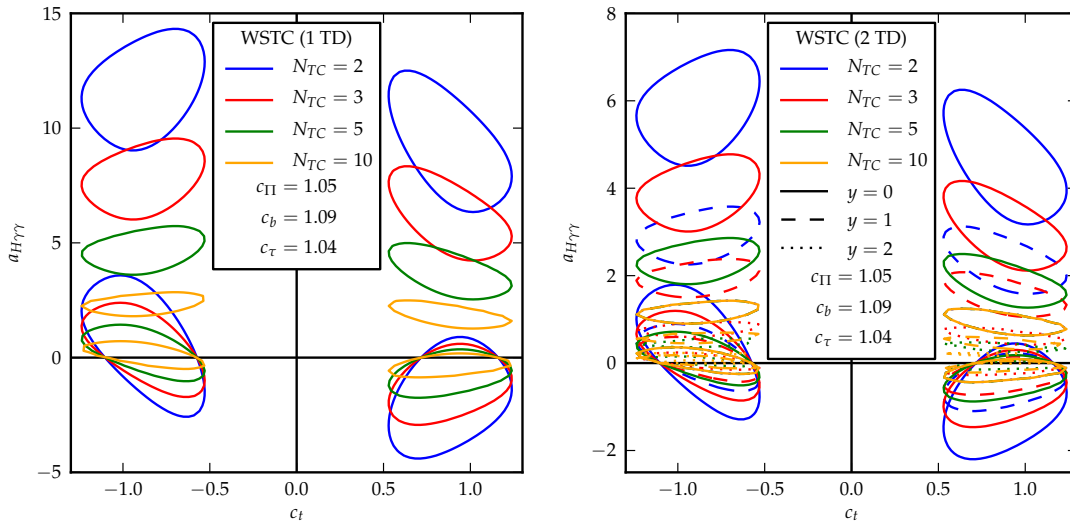


Figure 6.5: Left: 2σ exclusion contours of WSTC with one weak technidoublet and different numbers of technicolours. These fits apply also to PGTC and 2STC. Right: WSTC with two weak technidoublets, varying numbers of technicolours, and different values of the hypercharge parameter y . The parameters not plotted are set to their best-fit values, given in the legends.

(2STC) [113] theories where one electroweak technidoublet is in the fundamental representation of $SU(N_{TC})$ whilst the other technidoublets are in higher representations. We consider a particular example of 2STC called ultra-minimal Technicolor (UMT) where $N_{TC} = 2$ and there is one technidoublet in the fundamental and two electroweak neutral technifermions in the adjoint representation. UMT has the smallest “naive” S parameter of any TC theory with near-conformal dynamics.

Note that Table 6.1 only shows the techifermions with electroweak charge (these are needed to calculate the Higgs loop couplings). The extra technifermions in the Weinberg-Susskind class of theories discussed here purely affect the running of the coupling so as to achieve near-conformal dynamics. For the purposes of the Higgs fits, then, PGTC and 2STC are equivalent to pure WSTC with $N_D = 1$, and the 2σ exclusion contours, for this theory and for WSTC with $N_D = 2$, are shown in Figure 6.5. For $N_D = 1$, the hypercharge must be zero by anomaly cancellation, whereas the additional particles when $N_D = 2$ allow the hypercharge of the first technidoublet to take any value as long as the other doublet has the opposite value.

6.6.3 One-family Technicolor

The final class of TC theories we considered was one-family Technicolor (OFTC), defined in [114]. In OFTC theories, one adds technifermions with the correct SM quantum numbers to form a complete SM fermion family. There are hints from Schwinger-Dyson analysis that such a theory will have walking dynamics and this is being investigated

in lattice studies [115, 116, 117] as well. The technigauge group is $SU(N_{\text{TC}})$, and the technifermions each transform under the fundamental representation. We also relaxed the SM hypercharge assignment as shown in Table 6.1: the SM value coincides with the choice $y = 1/3$ in the parameterisation shown.

Using approximate values for the loop functions, and setting $c_{\Pi} \approx 1$, we can calculate the loop couplings to be

$$g_{H\gamma\gamma} \simeq \frac{\alpha}{8\pi} \left| 6 - \frac{16}{9}c_t - \frac{8}{3}N_{\text{TC}}(1 + 3y^2) a_{H\gamma\gamma} \right| \quad (6.27a)$$

$$g_{Hgg} \simeq \frac{\alpha_s}{16\pi} \left| -\frac{4}{3}c_t - \frac{8}{3}N_{\text{TC}} a_{Hgg} \right|. \quad (6.27b)$$

One can see here the previously-mentioned degeneracy between c_t , a_{Hgg} , and $a_{H\gamma\gamma}$. Choosing as an example $N_{\text{TC}} = 2$ and $c_t \approx 1$, we find that the two solutions $a_{Hgg} = -0.5, 0$ give a SM like gluon fusion production rate.

As usual, I plot the exclusion contours in a plane of the parameter space where the other parameters have been set to their best-fit values. To uniquely define the best-fit values (i.e. to break the above degeneracy) I set $c_t \approx 1$. There is an extra parameter a_{Hgg} compared to in the previous models, so I plot the contours in three planes, $(c_t, a_{H\gamma\gamma})$, (c_t, a_{Hgg}) and $(a_{Hgg}, a_{H\gamma\gamma})$: these plots are shown in Figure 6.6. In the $(a_{Hgg}, a_{H\gamma\gamma})$ plane I show several values of the hypercharge parameter y and for the other planes I just show the contours for $y = 1/3$.

It is interesting to note that for $y = 1/3$, the best-fit values of a_{Hgg} are far from unity. To push them up to $a_{Hgg} \approx 1$ would require a large value of c_t . If OFTC were the true theory of nature, and $a_{Hgg} \approx 1$ (implying that working at leading order in the hybrid model is accurate), then there would be a powerful experimentally-testable signature of greatly-enhanced ttH production. However, ETC generally struggles to provide such large values for c_t without violating EW precision tests.

Concentrating on the bottom-right plot in Figure 6.6, we can see the near-degeneracy between c_t and a_{Hgg} . As c_t is varied, the g_{Hgg} coupling can always be accurately predicted provided we pick the appropriate value for a_{Hgg} (a large value of c_t requires a large and negative value of a_{Hgg} so that the techniquark contributions partially cancel the enhanced SM quark contributions). However, this can only be pushed so far: if c_t strays too far from unity, eventually the diphoton rate will be affected (remembering that $a_{H\gamma\gamma}$ is fixed). The effect is weak because for $c_t \approx 1$ the SM quarks only contribute to the diphoton rate sub-dominantly, hence the very elongated ellipses.

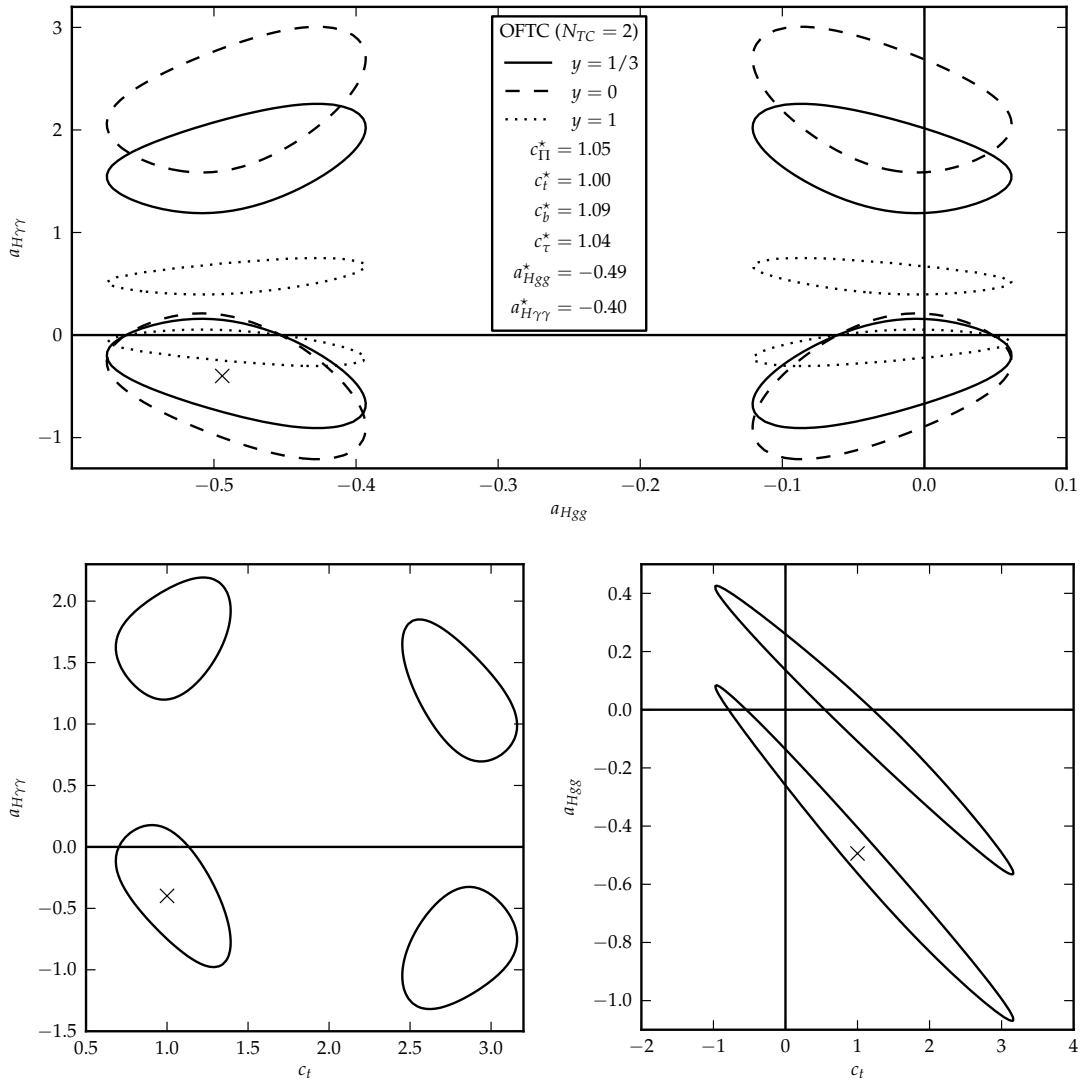


Figure 6.6: 2σ exclusion contours for one-family Technicolor (OFTC) with $N_{TC} = 2$ in three planes of interest. The first subfigure shows the contours for several values of the hypercharge parameter y , while the other plots fix $y = 1/3$. The stars denote the $y = 1/3$ best fit coordinates.

6.7 Conclusions

We have seen that Technicolor, inspired by QCD, provides a natural explanation for weak vector boson masses and can be extended to accommodate fermion masses too. Because there are no fundamental scalars in Technicolor, the role of the Higgs boson is played by the lightest scalar resonance of the composite sector that isn't a Goldstone boson of chiral symmetry breaking, analogous to the σ meson in QCD. Previous work has shown [93, 94, 95, 96, 97] that is possible to arrange for the “techni-Higgs” to have a mass of 125 GeV. We showed that the couplings of the techni-Higgs can (and, indeed, should be expected to) have SM-like couplings to the SM fermions, which is good news since the Higgs boson observed at the LHC is very consistent with the SM predictions.

In particular, we estimated the couplings of the techni-Higgs to the SM gluons and photons using a hybrid model containing fundamental techniquarks and the composite techni-Higgs and evaluating diagrams with triangle loops of techniquarks coupling to the techni-Higgs in proportion to their dynamical masses. This one-loop calculation is the leading order contribution in a $1/N_{\text{TC}}$ expansion and we parameterised the sub-leading corrections using the form factors a_{Hgg} and $a_{H\gamma\gamma}$. We estimated that $|a_{H\gamma\gamma}| \approx 2.37 \pm 0.39$ in QCD-like TC theories by comparing the $\sigma \rightarrow \gamma\gamma$ decay in QCD, but would expect deviations from this in non-QCD-like theories.

Introducing couplings to account for unknown Extended Technicolor effects for the Techni-Higgs coupling to SM particles, we analysed a selection of TC models in the context of the latest LHC Higgs couplings data, making use of two-parameter fits provided by ATLAS and CMS to obviate the need to know precise cut efficiencies and also to account for some of the correlations between systematic errors. We found best-fit values for the model parameters in each of the TC theories studied and plotted 2σ exclusion contours in the $(c_t, a_{H\gamma\gamma})$ plane, setting other parameters to their best-fit values.

The results show that the TC couplings take values very close to their SM values (as expected in TC theories). The near-unity top Yukawa enhancement $c_t \approx 1$ in particular is encouraging because such a value would help to keep the techni-Higgs light by the mechanism described in [97]. The form factor $a_{H\gamma\gamma}$ is also greater than or equal to unity for most of the models, consistent with TC expectations. However, for OFTC, the a_{Hgg} form factor was relevant and the Higgs data is most consistent with a small value of this, which is difficult to explain within TC.

The techni-Higgs is therefore a good candidate for the 125 GeV Higgs boson observed at the LHC. We would like to highlight the $SU(3)_{2S}$ MWT (NMWT) model in particular since it has the same global symmetries as two-flavour QCD and the fit does indeed match the expected $a_{H\gamma\gamma}$ from QCD. The model has been investigated on the lattice, and the results are consistent with a 125 GeV TC Higgs [97, 118, 119].

Chapter 7

Conclusions and outlook

The Standard Model is an excellent description of nature, but it is not without its problems. Some of these were outlined in the introduction, and these problems drive the theoretical physics community to dream up new beyond-the-Standard-Model (BSM) theories to solve them. This is an immensely ambitious undertaking and it has spawned hundreds of disparate theories, each aiming to solve a particular subset of the known issues in the SM. It has therefore become vital to put these theories to the test.

This thesis examined three approaches to the problems of the Standard Model: Minimal Universal Extra Dimensions, the 4D Composite Higgs Model, and Technicolor. MUED was inspired by string theory, itself an attempt to solve the problem of quantum gravity. MUED also potentially solves the Dark Matter problem. The 4DCHM and Technicolor both aim to solve the hierarchy problem of the SM in different ways.

With the switch-on of the LHC, we have been provided with huge volumes of experimental data that we can challenge BSM models with. In this thesis, I have focused on using the data from experimental searches for, and subsequent measurements of, the Higgs boson, discovered with a mass of around 125 GeV. The first Higgs project described here, testing MUED, dated from before the discovery of the Higgs. It was difficult to apply the results of the Higgs searches to try to constrain MUED because of the presentation of results by ATLAS and CMS. We had to infer signal enhancements from observed and expected exclusion limits through a series of approximations that surely introduces uncertainties. However, the quality of the presentation of results has continuously improved with time.

The 4DCHM project was conducted after the discovery of the Higgs and benefited from the signal enhancements being readily available. We saw that the 4DCMH fit the LHC data well for large regions of the parameter space, once direct detection constraints were applied. There was still, however, an element of approximation in the analysis due to the correlations between systematic errors and the cut efficiencies being unavailable. Now,

the experimentalists are increasingly making efficiency factors available, at least in some of the channels, although it would be very valuable for them to go further. ATLAS and CMS do perform their own, statistically sophisticated, “model independent” tests. This generally involves working with an effective Lagrangian with a selection of unknown parameters, and then setting many of the parameters equal to each other in order to thin the parameter space and make scans and plots easy to perform. Such model independent tests are unfortunately no substitute for being able to specifically test BSM models individually: the necessarily-simple parameterisations used do not often correspond to *any* theoretically well-motivated theory.

For the work concerning Technicolor, a considerably more sophisticated technique was available to us due to the ATLAS and CMS collaborations presenting their 2D fits. This allows theorists to account for some of the correlations in systematic errors and avoid problems with unknown efficiencies. Applying this method, we saw that many Technicolor models are consistent with the data and they remain promising candidates to explain the origin of EWSB. The two-parameter-fit method, however, is still only applicable to models with SM-like kinematics and whose W and Z Higgs couplings are uniformly modified.

It is highly encouraging that the experimental collaborations are providing their data in increasingly useful and flexible forms. I hope that soon that they will make available the full likelihood functions in software form so that many different BSM models can be tested easily and to high precision.

Another common theme throughout this thesis is the importance of software when exploring new physics. In the MUED and 4DCHM projects, heavy use was made of CalcHEP software implementations to automate the calculation of couplings, cross-sections and decays. This makes it possible to perform calculations and parameter scans that would be simply to do by hand. Similarly, for the Technicolor project, I wrote a Python program for calculating signal enhancements from an effective Lagrangian and then taking the two-parameter plots made available by ATLAS and CMS and using this to calculate the χ^2 fit of a model to data. We used the code to analyse certain Technicolor theories, but it is easily applicable to a whole range of other theories, and can be trivially updated as new data becomes available. This provides the speed that is absolutely necessary when there are so many hundreds of models that demand testing.

In the coming years, as new Higgs data, better communication between experiment and theory, and new software implementations of models become available, Higgs physics promises to provide increasingly powerful ways to test BSM theories.

Appendix A

MUED Higgs calculation

A.1 Feynman rules

Below is a table of the Feynman rules for the propagators and vertices needed to evaluate the diagrams contributing to the $gg \rightarrow H$ and $H \rightarrow \gamma\gamma$ amplitudes. The vertex rules are given in terms of a general coefficient; underneath this, the value of the coefficient is written for the SM case and for the n th KK level. A $(+ - - -)$ signature and the following momentum conventions are used: fermion momentum flows in the same direction as fermion number and external momentum flows inwards. This convention is shown graphically in Figure 3.6

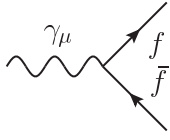
A.1.1 Propagators

$$\begin{array}{c} \longrightarrow \\ p \end{array} = \frac{i(\not{p} + m)}{p^2 - m^2 + i\epsilon} \quad (\text{A.1})$$

$$\begin{array}{c} \cdots\cdots\longrightarrow \\ p \end{array} = \frac{i}{p^2 - m^2 + i\epsilon} \quad (\text{A.2})$$

$$\begin{array}{c} \mu \quad \sim\sim\sim \quad \nu \\ \longrightarrow \\ p \end{array} = \frac{-ig_{\mu\nu}}{p^2 - m^2 + i\epsilon} \quad (\text{Feynman-'t Hooft gauge}) \quad (\text{A.3})$$

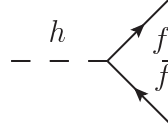
A.1.2 Vertices



$$iG_{ff}\gamma_\mu$$

$$G_{ff}^{\text{SM}} = -eQ_f$$

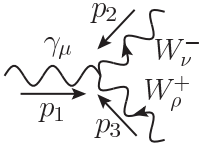
$$G_{ff}^{(n)} = -eQ_f$$



$$i\lambda_{ff}$$

$$\lambda_{ff}^{\text{SM}} = -\frac{gm_f}{2m_W}$$

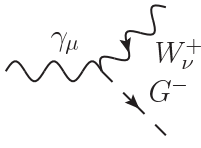
$$\lambda_{ff}^{(n)} = -\frac{gm_f}{2m_W} \sin 2\alpha_f^{(n)}$$



$$iG_{WW}(p_3\mu g_{\nu\rho} - p_3\nu g_{\mu\rho} - p_1\rho g_{\mu\nu} + p_1\nu g_{\mu\rho} + p_2\rho g_{\mu\nu} - p_2\nu g_{\nu\rho})$$

$$G_{WW}^{\text{SM}} = -e$$

$$G_{WW}^{(n)} = -e$$

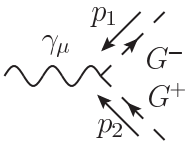


$$= - \left(\text{Feynman diagram with } W_nu^- \text{ and } G^+ \right)$$

$$G_{WG}g_{\mu\nu}$$

$$G_{WG}^{\text{SM}} = em_W$$

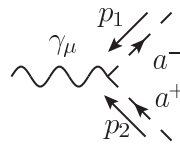
$$G_{WG}^{(n)} = em_{W,n}$$



$$iG_{GG}(p_2 - p_1)_\mu$$

$$G_{GG}^{\text{SM}} = e$$

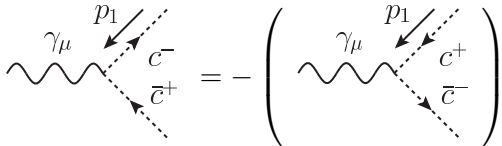
$$G_{GG}^{(n)} = e$$



$$iG_{aa}(p_2 - p_1)_\mu$$

$$G_{aa}^{\text{SM}} = 0$$

$$G_{aa}^{(n)} = e$$

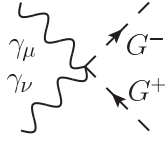


$$= - \left(\text{Feynman diagram with } c^+ \text{ and } c^- \right)$$

$$iG_{\bar{c}c}p_{1\mu}$$

$$G_{\bar{c}c}^{\text{SM}} = -e$$

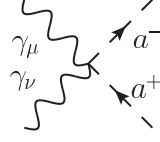
$$G_{\bar{c}c}^{(n)} = -e$$



$$iH_{GG}g_{\mu\nu}$$

$$H_{GG}^{\text{SM}} = 2e^2$$

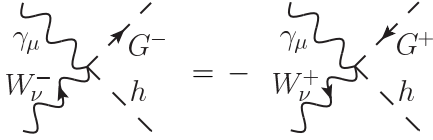
$$H_{GG}^{(n)} = 2e^2$$



$$iH_{aa}g_{\mu\nu}$$

$$H_{aa}^{\text{SM}} = 0$$

$$H_{aa}^{(n)} = 2e^2$$



$$I_{WG}g_{\mu\nu}$$

$$I_{WG}^{\text{SM}} = -\frac{eg}{2}$$

$$I_{WG}^{(n)} = -\frac{eg}{2} \frac{m_W}{m_{W,n}}$$

A.2 $gg \rightarrow H$ amplitude

Here I detail the calculation of the generic 1-loop amplitude for two gluons to produce a Higgs boson via a quark loop. The couplings and quark masses are left general for now and will be specialised to the SM and MUED case below.

$$i(\mathcal{A}_{ggH,q})_{\mu\nu}^{ab} = 2 \times$$

To form the amplitude this should be contracted with the gluon polarisation vectors which carry Lorentz and group indices. The labeled arrows denote momentum flow; the other labels designate the particle names.

The KK and SM quarks couple to gluons identically as $ig_s t_a$, where g_s is the strong coupling constant and t^a is an $SU(3)$ generator. Let us call the Yukawa coupling $i\lambda_q$.

Performing the loop momentum integral in $D = 4 - \epsilon$ dimensions to regulate the divergence (and introducing the renormalisation scale μ to compensate), the amplitude

without polarisation vectors is

$$i(\mathcal{A}_{ggH,q})_{\mu\nu}^{ab} = -2(ig_s)^2(i\lambda_q)\text{Tr}(t^a t^b)\mu^{4-D} \quad (\text{A.4})$$

$$\times \int \frac{d^D k}{(2\pi)^D} \text{tr} \left\{ \frac{i(\not{k} + m)}{k^2 - m^2 + i\epsilon} \gamma^\mu \frac{i(\not{k} + \not{p} + m)}{(k+p)^2 - m^2 + i\epsilon} \frac{i(\not{k} - \not{q} + m)}{(k-q)^2 - m^2 + i\epsilon} \gamma^\nu \right\} \quad (\text{A.5})$$

with the overall minus sign due to the fermion loop. The propagator conventions used here are given in Appendix A.1 with the mass set to a general quark mass m (the symbol m_q is reserved for the SM mass of quark q). The trace Tr is over the $\text{SU}(3)$ generators and tr is over the product of Dirac matrices.

The rest of the calculation (and all following calculations) assumes that the gluons and Higgs boson are physical, so $p^2 = q^2 = 0$, $p^\mu \epsilon_\mu(p) = q^\nu \epsilon_\nu(q) = 0$ and $(p+q)^2 = m_H^2$. The approximation that the Higgs is real is justified if the ‘‘narrow width approximation’’ is valid (see Sec. 4.9.1 for details).

The numerator of the Dirac trace (rejecting off-shell terms as discussed above) is

$$i^3 \times 4m [g_{\mu\nu}(m^2 - k^2 - m_H^2/2) + 4k_\mu k_\nu + p_\nu q_\mu] = i^3 \times 4m \{ [(m^2 - m_H^2/2)g_{\mu\nu} + p_\nu q_\mu] - g_{\mu\nu} k^2 + 4k_\mu k_\nu \}. \quad (\text{A.6})$$

In terms of PV functions (defined in Appendix A.4) the amplitude becomes

$$i(\mathcal{A}_{ggH,q})_{\mu\nu}^{ab} = -2(ig_s)^2(i\lambda_q)\text{Tr}(t^a t^b) i^3 \frac{i\pi^2}{(2\pi)^4} 4m \{ [(m^2 - m_H^2/2)g_{\mu\nu} + p_\nu q_\mu] C_0 + g_{\mu\nu} C_\rho^\rho + 4C_{\mu\nu} \}. \quad (\text{A.7})$$

Performing Passarino-Veltman reduction, and carefully taking the limit $D \rightarrow 4$, we see that

$$i(\mathcal{A}_{ggH,q})_{\mu\nu}^{ab} = \frac{i}{2\pi^2} \lambda_q g_s^2 \text{Tr}(t^a t^b) m \left(\frac{g_{\mu\nu} m_H^2}{2} - p_\nu q_\mu \right) \left[\frac{2}{m_H^2} - \left(1 - \frac{4m^2}{m_H^2} \right) C_0 \right]. \quad (\text{A.8})$$

For $\text{SU}(3)$ generators, $\text{Tr}(t^a t^b) = \frac{1}{2} \delta^{ab}$ so the quark q 's total contribution to the amplitude is

$$i(\mathcal{A}_{ggH,q})_{\mu\nu}^{ab} = \frac{i\alpha_s}{\pi} \delta^{ab} \left(\frac{g_{\mu\nu} m_H^2}{2} - p_\nu q_\mu \right) \lambda_q m \left[\frac{2}{m_H^2} - \left(1 - \frac{4m^2}{m_H^2} \right) C_0(m, m_H) \right], \quad (\text{A.9})$$

where $\alpha_s = g_s^2/4\pi$.

It is useful to factor out the Lorentz and colour dependence by defining the ‘‘reduced amplitude’’ $\tilde{\mathcal{A}}$ for a particular process in terms of the the full (*sans* polarisation vectors) amplitude $\mathcal{A}_{\mu\nu}^{ab}$:

$$\mathcal{A}_{\mu\nu}^{ab} = \tilde{\mathcal{A}} \times \delta^{ab} \left(\frac{g_{\mu\nu} m_H^2}{2} - p_\nu q_\mu \right), \quad (\text{A.10})$$

so in this case

$$\tilde{\mathcal{A}}_{ggH,q} = \frac{\alpha_s}{\pi} \lambda_q m \left[\frac{2}{m_H^2} - \left(1 - \frac{4m^2}{m_H^2} \right) C_0(m, m_H) \right], \quad (\text{A.11})$$

which can be written in terms of the function defined in (3.37a) as

$$\tilde{\mathcal{A}}_{ggH,q} = \frac{\alpha_s}{4\pi} \lambda_q \frac{1}{m} f_F(m). \quad (\text{A.12})$$

A.2.1 Specialising couplings

A.2.1.1 Standard Model

Equation A.12 is in terms of the mass m and Yukawa coupling λ_q of a general quark q . For the SM quarks, let $m = m_q$ with $q \in \{u, d, s, c, b, t\}$. The SM Yukawa coupling in terms of the Higgs vev v is $\lambda_q^{\text{SM}} = -m_q/v$, so

$$\tilde{\mathcal{A}}_{ggH}^{\text{SM}} = -\frac{\alpha_s}{4\pi v} F_{ggH}^{\text{SM}}, \quad (\text{A.13})$$

where

$$F_{ggH}^{\text{SM}} = \sum_q f_F(m_q), \quad (\text{A.14})$$

which is the expression shown in (4.63) and the following paragraph in Section 4.9.1.

A.2.1.2 Including KK modes

At each KK level n , there are two types of quarks $q_1^{(n)}$ and $q_2^{(n)}$ for each SM quark q . At tree level, these quarks' masses would both be $\sqrt{m_q^2 + n^2/R^2}$, but if one-loop mass corrections are included then they split. However, Yukawa couplings to the Higgs are shifted equally under mass corrections so $\lambda_q^{(n)} = -m_q \sin(2\alpha_q^{(n)})/v$ for both $q_1^{(n)}$ and $q_2^{(n)}$. Here $\alpha_q^{(n)}$ is the mixing angle between quark flavour eigenstates ($q_L^{(n)}, q_R^{(n)}$) and mass eigenstates ($q_1^{(n)}, q_2^{(n)}$) as explained in Section 4.5.2.

The contribution to $\tilde{\mathcal{A}}_{ggH}$ from the KK level n quarks is then $\tilde{\mathcal{A}}_{ggH}^{(n)} = -\frac{\alpha_s}{4\pi v} F_{ggH}^{(n)}$, where

$$F_{ggH}^{(n)} = \sum_q \sin(2\alpha_q^{(n)}) \left(\frac{m_q}{m_{q,1}^{(n)}} f_F(m_{q,1}^{(n)}, m_H) + \frac{m_q}{m_{q,2}^{(n)}} f_F(m_{q,2}^{(n)}, m_H) \right). \quad (\text{A.15})$$

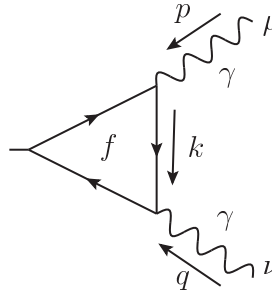
The full expression for F_{ggH} (and hence $\tilde{\mathcal{A}}_{ggH}$), as given in Equation 4.65, is obtained by summing over the KK number n and adding the SM contribution from Equation A.14.

A.3 $H \rightarrow \gamma\gamma$ amplitude

The full $H \rightarrow \gamma\gamma$ amplitude receives contributions from fermions (quarks and leptons), W bosons and charged scalars a^\pm (which appear at KK number 1 and above). I use the subscript f , W and a to distinguish these contributions.

A.3.1 Fermion contribution

For each fermion there are two contributing diagrams (equal to each other and related by the swapping external photons).

$$i(\mathcal{A}_f)_{\mu\nu} = 2 \times \left[-\frac{h}{\mathcal{D}} \right] \times \text{Diagram} \quad (\text{A.16})$$


Leaving the couplings general and using the Feynman rules in Appendix A.1 we find that

$$i(\mathcal{A}_f)_{\mu\nu} = -2(+iG_{ff})^2(+i\lambda_{ff})(+i)^3 \int_k \frac{1}{\mathcal{D}} \text{tr}[(\not{k} + m)\gamma_\mu(\not{k} + \not{p} + m)(\not{k} - \not{q} + m)\gamma_\nu] \quad (\text{A.17})$$

$$= \frac{2iG_{ff}^2\lambda_{ff}}{16\pi^2} \left[4\frac{m}{m_H^2}(4m^2 - m_H^2)C_0 + \frac{8m}{m_H^2} \right] \left(\frac{m_H^2 g_{\mu\nu}}{2} - p_\nu q_\mu \right). \quad (\text{A.18})$$

where I have used the shorthand

$$\int_k \equiv \int \frac{d^D k}{(2\pi)^D} \mu^{4-D} \quad (\text{A.19})$$

for the dimensionally-regularised momentum integral and where we have written the denominator, common to all triangle diagrams considered here, as

$$\mathcal{D} = [k^2 - m^2 + i\epsilon][(k+p)^2 - m^2 + i\epsilon][(k-q)^2 - m^2 + i\epsilon]. \quad (\text{A.20})$$

Factoring out the Lorentz part yields as in the ggH case leaves

$$\tilde{\mathcal{A}}_f = \frac{G_{ff}^2\lambda_{ff}}{8\pi^2} \frac{1}{m} f_F(m), \quad (\text{A.21})$$

with $f_F(m)$ defined as in Equation 3.37a.

Specialising to the SM using the rules in Appendix A.1 gives

$$\tilde{\mathcal{A}}_f^{\text{SM}} = -\frac{Q_f^2 e^2}{8\pi^2 v} f_F(m_f), \quad (\text{A.22})$$

where $v = 2m_W/g$ is the Higgs vev and $Q_f e$ is the charge of the fermion.

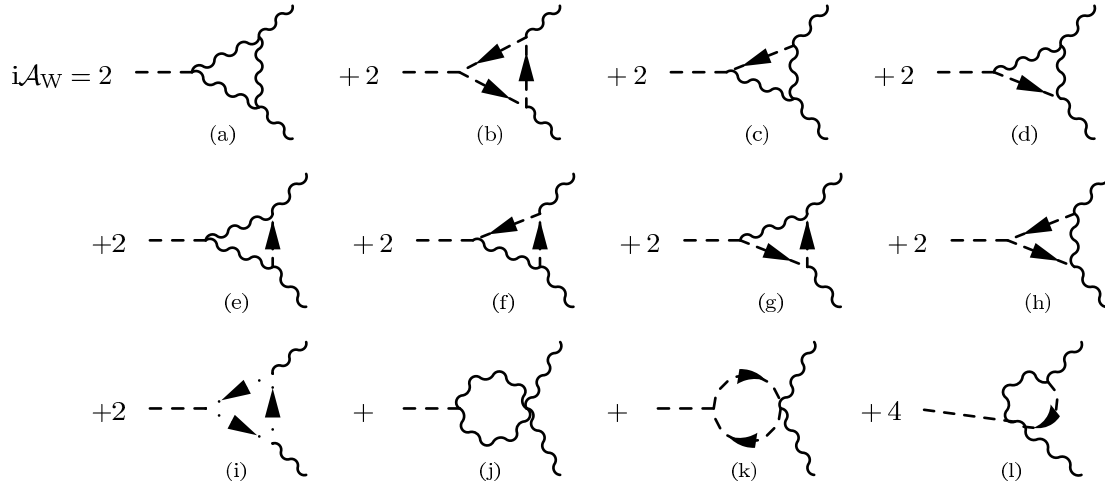
The contribution from an n th level KK fermion is

$$\tilde{\mathcal{A}}_f^{(n)} = -\frac{Q_f^2 e^2}{8\pi^2 v} \sin 2\alpha_f^{(n)} f_F(m_f^{(n)}), \quad (\text{A.23})$$

where $\alpha_f^{(n)}$ is the mixing angle for converting from the flavour to the mass eigenbasis of the KK fermion.

A.3.2 Gauge boson contribution

There is an additional (in fact dominant) contribution to the $h \rightarrow \gamma\gamma$ amplitude from SM and KK W bosons and their associated Goldstone bosons and Faddeev-Popov ghosts. I performed the calculation in the 't Hooft-Feynman gauge (the R_ξ gauge with $\xi = 1$). The relevant diagrams, including Goldstone (dashed) and ghost (dotted) internal lines, are as follows.



In the following I calculate the general expression for each diagram in turn and the corresponding SM and n th KK level expressions using the values for the couplings in Equation A.1.

There are two W diagrams (related by crossing the external photons):

$$\begin{aligned}
i(\mathcal{A}_a)_{\mu\nu} &= 2 \times (iG_{WW})^2 (i\lambda_{WW}) (-i)^3 \int_k \frac{1}{D} g^{\rho\sigma} [-(k+p)_\mu g_{\sigma\lambda} + (k+p)_\sigma g_{\mu\lambda} - p_\lambda g_{\mu\sigma} + p_\sigma g_{\mu\lambda} \\
&\quad + k_\lambda g_{\mu\sigma} - k_\mu g_{\sigma\lambda}] g^{\lambda\kappa} g_{\kappa\alpha} g^{\alpha\beta} [-k_\nu g_{\beta\rho} + k_\beta g_{\nu\rho} - q_\rho g_{\nu\beta} + q_\beta g_{\nu\rho} + (k-q)_\rho g_{\nu\beta} - (k-q)_\nu g_{\beta\rho}] \\
&= 2G_{WW}^2 \lambda_{WW} \frac{i\pi^2}{(2\pi)^4} [2g_{\mu\nu} g^{\rho\sigma} C_{\rho\sigma} + g_{\mu\nu} (p-q)^\rho C_\rho - \frac{5g_{\mu\nu} m_H^2}{2} C_0 + 10C_{\mu\nu} + p_\nu C_\mu - q_\mu C_\nu \\
&\quad + 4p_\nu q_\mu C_0] \\
&= \frac{iG_{WW}^2 \lambda_{WW}}{8\pi^2} [2Dg_{\mu\nu} C_{00} - 2m_H^2 g_{\mu\nu} C_{12} - g_{\mu\nu} m_H^2 C_1 - \frac{5g_{\mu\nu} m_H^2}{2} C_0 + 10g_{\mu\nu} C_{00} - 10p_\nu q_\mu C_{12} \\
&\quad - 2p_\nu q_\mu C_1 + 4p_\nu q_\mu C_0] \\
&= \frac{iG_{WW}^2 \lambda_{WW}}{8\pi^2} \left[\left(Dm^2 g_{\mu\nu} + 3m^2 g_{\mu\nu} - \frac{5}{2} m_H^2 g_{\mu\nu} - \frac{10m^2 p_\nu q_\mu}{m_H^2} + 4p_\nu q_\mu \right) C_0 \right. \\
&\quad + \left(\frac{1}{2} Dg_{\mu\nu} - \frac{2p_\nu q_\mu}{m_H^2} + \frac{3}{2} g_{\mu\nu} \right) B_0(m_H^2, m^2) + \left(g_{\mu\nu} + \frac{2p_\nu q_\mu}{m_H^2} \right) B_0(0, m^2) + \frac{Dg_{\mu\nu}}{2} + \frac{3g_{\mu\nu}}{2} \\
&\quad \left. - \frac{5p_\nu q_\mu}{m_H^2} \right] \\
&= \frac{iG_{WW}^2 \lambda_{WW}}{8\pi^2} \left[\left(4m^2 g_{\mu\nu} + 3m^2 g_{\mu\nu} - \frac{5}{2} m_H^2 g_{\mu\nu} - \frac{10m^2 p_\nu q_\mu}{m_H^2} + 4p_\nu q_\mu \right) C_0 \right. \\
&\quad + \left(2g_{\mu\nu} - \frac{2p_\nu q_\mu}{m_H^2} + \frac{3}{2} g_{\mu\nu} \right) B_0(m_H^2, m^2) + \left(g_{\mu\nu} + \frac{2p_\nu q_\mu}{m_H^2} \right) B_0(0, m^2) + \frac{5g_{\mu\nu}}{2} \\
&\quad \left. - \frac{5p_\nu q_\mu}{m_H^2} \right].
\end{aligned} \tag{A.24}$$

Throughout the calculation let us work in $D = 4 - \epsilon$ dimensions except for the last equality where we will take the $\epsilon \rightarrow 0^+$ limit. Care must be taken in the case of the first B_0 function:

$$\lim_{\epsilon \rightarrow 0^+} [DB_0(m_H^2, m^2)] = 4 \lim_{\epsilon \rightarrow 0^+} [B_0(m_H^2, m^2)] - 2; \tag{A.25}$$

this is the origin of the extra $-g_{\mu\nu}$ term in the last line.

The two Goldstone loop diagrams evaluate to

$$\begin{aligned}
i(\mathcal{A}_b)_{\mu\nu} &= 2 \times (iG_{GG})^2 (i\lambda_{GG}) (+i)^3 \int_k \frac{1}{D} [-(k+p) - k]_\mu [-k - (k-q)]_\nu \\
&= -2G_{GG}^2 \lambda_{GG} \frac{i\pi^2}{(2\pi)^4} 4C_{\mu\nu} \\
&= -\frac{iG_{GG}^2 \lambda_{GG}}{2\pi^2} (C_{00} g_{\mu\nu} - p_\nu q_\mu C_{12}) \\
&= -\frac{iG_{GG}^2 \lambda_{GG}}{2\pi^2} \left[\left(\frac{m^2 g_{\mu\nu}}{2} - \frac{m^2 p_\nu q_\mu}{m_H^2} \right) C_0 + \frac{g_{\mu\nu}}{4} B_0(m_H^2, m^2) + \left(\frac{g_{\mu\nu}}{4} - \frac{p_\nu q_\mu}{2m_H^2} \right) \right].
\end{aligned} \tag{A.26}$$

There are 3×2 diagrams with two W s and one Goldstone. The first four give¹

$$\begin{aligned}
i(\mathcal{A}_c)_{\mu\nu} &= i(\mathcal{A}_d)_{\mu\nu} = 2 \times (-G_{WG})(\lambda_{WG})(iG_{WW})(-i)^2(+i) \int_k \frac{1}{\mathcal{D}} g^{\rho\sigma} g_{\mu\sigma} [-(p+q) - (k+p)]_\lambda \\
&\quad \times g^{\lambda\kappa} [-k_\nu g_{\kappa\rho} + k_\kappa g_{\nu\rho} - q_\rho g_{\nu\kappa} + q_\kappa g_{\nu\rho} + (k-q)_\rho g_{\nu\kappa} - (k-q)_\nu g_{\kappa\rho}] \\
&= \frac{iG_{WG}G_{WW}\lambda_{WG}}{8\pi^2} \\
&\quad \times [g_{\mu\nu}g^{\rho\sigma}C_{\rho\sigma} + 2g_{\mu\nu}(p+q)^\rho C_\rho + g_{\mu\nu}m_H^2 C_0 - C_{\mu\nu} + 2p_\nu C_\mu - 4q_\mu C_\nu - 4p_\nu q_\mu C_0] \\
&= \frac{iG_{WG}G_{WW}\lambda_{WG}}{8\pi^2} [(D-1)g_{\mu\nu}C_{00} - (m_H^2 g_{\mu\nu} - p_\nu q_\mu)C_{12} + (m_H^2 g_{\mu\nu} - 4p_\nu q_\mu)C_1 \\
&\quad - (m_H^2 g_{\mu\nu} + 2p_\nu q_\mu)C_2 + (m_H^2 g_{\mu\nu} - 4p_\nu q_\mu)C_0] \\
&= \frac{iG_{WG}G_{WW}\lambda_{WG}}{8\pi^2} \left[\left(\frac{(D-1)g_{\mu\nu}}{4} - \frac{6p_\nu q_\mu}{m_H^2} \right) B_0(m_H^2, m^2) + \frac{6p_\nu q_\mu}{m_H^2} B_0(0, m^2) \right. \\
&\quad \left. + \left(\frac{(D-3)}{2} m^2 g_{\mu\nu} + m_H^2 g_{\mu\nu} + \frac{m^2}{m_H^2} p_\nu q_\mu - 4p_\nu q_\mu \right) C_0 + \frac{(D-3)g_{\mu\nu}}{4} + \frac{p_\nu q_\mu}{2m_H^2} \right] \\
&= \frac{iG_{WG}G_{WW}\lambda_{WG}}{8\pi^2} \left[\left(\frac{3}{4} g_{\mu\nu} - \frac{6p_\nu q_\mu}{m_H^2} \right) B_0(m_H^2, m^2) - \frac{g_{\mu\nu}}{2} + \frac{6p_\nu q_\mu}{m_H^2} B_0(0, m^2) \right. \\
&\quad \left. \left(\frac{m^2}{2} g_{\mu\nu} + m_H^2 g_{\mu\nu} + \frac{m^2}{m_H^2} p_\nu q_\mu - 4p_\nu q_\mu \right) C_0 + \frac{g_{\mu\nu}}{4} + \frac{p_\nu q_\mu}{2m_H^2} \right].
\end{aligned} \tag{A.27}$$

The second two yield

$$\begin{aligned}
i(\mathcal{A}_e)_{\mu\nu} &= 2 \times (G_{WG})(-G_{WG})(i\lambda_{WW})(i)(-i)^2 \int_k \frac{1}{\mathcal{D}} \left(g_{\mu\rho} g^{\rho\sigma} g_{\sigma\lambda} g^{\lambda\kappa} g_{\kappa\nu} \right) \\
&= \frac{i\lambda_{WW}G_{Wf}^2 g^{\mu\nu}}{8\pi^2} C_0.
\end{aligned} \tag{A.28}$$

¹As in the case of $\tilde{\mathcal{A}}_a$, one must be careful when taking the $D \rightarrow 4$ limit in the last equality.

There are similarly 3×2 diagrams involving one W and two Goldstones. The first four evaluate to

$$\begin{aligned}
i(\mathcal{A}_f)_{\mu\nu} &= i(\mathcal{A}_g)_{\mu\nu} = 2 \times (iG_{GG})(\lambda_{WG})(-G_{WG})(+i)^2(-i) \\
&\quad \int_k \frac{1}{\mathcal{D}} [-(k+p) - k]_{\mu} [-(p+q) - (k+p)]_{\rho} g^{\rho\sigma} g_{\nu\sigma} \\
&= 2G_{GG}G_{WG}\lambda_{WG} \int_k \frac{1}{\mathcal{D}} 2k_{\mu}(2p+q+k)_{\nu} \\
&= \frac{iG_{GG}G_{WG}\lambda_{WG}}{4\pi^2} (2p_{\nu}C_{\mu} + C_{\mu\nu}) \\
&= \frac{iG_{GG}G_{WG}\lambda_{WG}}{4\pi^2} (-2p_{\nu}q_{\mu}C_1 + g_{\mu\nu}C_{00} - p_{\nu}q_{\mu}C_{12}) \\
&= \frac{iG_{GG}G_{WG}\lambda_{WG}}{4\pi^2} \left[\left(\frac{m^2 g_{\mu\nu}}{2} - \frac{m^2 p_{\nu}q_{\mu}}{m_H^2} \right) C_0 + \left(\frac{g_{\mu\nu}}{4} - \frac{2p_{\nu}q_{\mu}}{m_H^2} \right) B_0(m_H^2, m^2) \right. \\
&\quad \left. + \frac{2p_{\nu}q_{\mu}}{m_H^2} B_0(0, m^2) + \left(\frac{g_{\mu\nu}}{4} - \frac{p_{\nu}q_{\mu}}{2m_H^2} \right) \right]
\end{aligned} \tag{A.29}$$

while the other two give

$$\begin{aligned}
i(\mathcal{A}_h)_{\mu\nu} &= 2 \times (-G_{WG})(+G_{WG})(+i\lambda_{GG})(i)^2(-i) \int_k \frac{1}{\mathcal{D}} g^{\rho\sigma} g_{\mu\sigma} g_{\nu\rho} \\
&= \frac{i\lambda_{GG}G_{WG}^2 g_{\mu\nu}}{8\pi^2} C_0.
\end{aligned} \tag{A.30}$$

The last triangle diagrams are the two involving Faddeev-Popov ghosts:

$$\begin{aligned}
i(\mathcal{A}_i)_{\mu\nu} &= -2 \times (-iG_{\bar{c}c})^2 (+i\lambda_{\bar{c}c})(+i)^3 \int_k \frac{1}{\mathcal{D}} [-(k+p)]_{\mu} (-k)_{\nu} \\
&= 2G_{\bar{c}c}^2 \lambda_{\bar{c}c} \frac{i\pi^2}{(2\pi)^4} C_{\mu\nu} \\
&= \frac{iG_{\bar{c}c}^2 \lambda_{\bar{c}c}}{8\pi^2} (C_{00}g_{\mu\nu} - p_{\nu}q_{\mu}C_{12}) \\
&= \frac{iG_{\bar{c}c}^2 \lambda_{\bar{c}c}}{8\pi^2} \left[\left(\frac{m^2}{m_H^2} C_0 + \frac{1}{2m_H^2} \right) \left(\frac{m_H^2 g_{\mu\nu}}{2} - p_{\nu}q_{\mu} \right) + \frac{g_{\mu\nu}}{4} B_0(m_H^2, m^2) \right].
\end{aligned} \tag{A.31}$$

There are six remaining (non-triangle) diagrams involving four-point vertices. The W diagram evaluates to

$$\begin{aligned}
i(\mathcal{A}_j)_{\mu\nu} &= (iH_{WW})(i\lambda_{WW})(-i)^2 \int_k \frac{g^{\rho\sigma}}{k^2 - m^2 + i\epsilon} g_{\sigma\lambda} \frac{g^{\lambda\kappa}}{(k-p-q)^2 - m^2 + i\epsilon} (2g_{\mu\nu}g_{\kappa\rho} - g_{\mu\rho}g_{\nu\kappa} - g_{\mu\kappa}g_{\nu\rho}) \\
&= H_{WW}\lambda_{WW}2g_{\mu\nu}(D-1)\frac{i\pi^2}{(2\pi)^4}B_0(m_H^2, m^2) \\
&= \frac{iH_{WW}\lambda_{WW}(D-1)g_{\mu\nu}}{8\pi^2}B_0(m_H^2, m^2) \\
&= \frac{iH_{WW}\lambda_{WW}g_{\mu\nu}}{8\pi^2}[3B_0(m_H^2, m^2) - 2],
\end{aligned} \tag{A.32}$$

and the Goldstone diagram evaluates to

$$\begin{aligned}
i(\mathcal{A}_k)_{\mu\nu} &= (iH_{GG})(i\lambda_{GG})(i)^2g_{\mu\nu} \int_k \frac{1}{k^2 - m^2 + i\epsilon} \frac{1}{(k-p-q)^2 - m^2 + i\epsilon} \\
&= \frac{iH_{GG}\lambda_{GG}g_{\mu\nu}}{16\pi^2}B_0(m_H^2, m^2).
\end{aligned} \tag{A.33}$$

The last four diagrams are related to diagram (1) (shown above) by swapping external momenta and changing the direction of internal particle number flow:

$$\begin{aligned}
i(\mathcal{A}_l)_{\mu\nu} &= 4 \times (-G_{WG})(+I_{WG})(-i)(+i) \int_k \frac{g^{\rho\sigma}g_{\mu\sigma}g_{\nu\rho}}{(k^2 - m^2 + i\epsilon)[(k+p)^2 - m^2 + i\epsilon]} \\
&= -\frac{iG_{WG}I_{WG}g_{\mu\nu}}{4\pi^2}B_0(0, m^2).
\end{aligned} \tag{A.34}$$

A.3.3 Summing the diagrams

We now need to sum the diagrams to find the SM and n th KK level contributions. I have checked the following expressions in Mathematica.

Putting in the SM values for masses and couplings gives the following. The Goldstone and ghost have the same mass as the W boson. (The same applies for the higher KK modes.)

$$\begin{aligned}
i(\mathcal{A}_W^{\text{SM}})_{\mu\nu} &= \frac{3ie^2gm_H^2m_Wg_{\mu\nu}C_0}{8\pi^2} + \frac{3ie^2gm_W^3g_{\mu\nu}C_0}{4\pi^2} + \frac{3ie^2gm_Wp^\nu q^\mu C_0}{4\pi^2} - \frac{3ie^2gm_W^3p_\nu q_\mu C_0}{2\pi^2m_H^2} \\
&+ \frac{ie^2gm_H^2g_{\mu\nu}}{16\pi^2m_W} + \frac{3ie^2gm_Wg_{\mu\nu}}{8\pi^2} - \frac{3ie^2gm_Wp_\nu q_\mu}{4\pi^2m_H^2} - \frac{ie^2gp_\nu q_\mu}{8\pi^2m_W}.
\end{aligned} \tag{A.35}$$

Factoring out the Lorentz part and writing things in terms of the dimensionless function f_V , defined in Equation 3.37b, gives

$$\tilde{\mathcal{A}}_W = -\frac{e^2g}{16\pi^2m_W}f_V(m_W). \tag{A.36}$$

The sum of the diagrams at the n th KK level is

$$i(\mathcal{A}_W^{(n)})_{\mu\nu} = \frac{ie^2 g m_W}{8\pi^2 m_H^2 m_{W,n}^2} [m_H^2 + 6m_{W,n}^2 + (12m_{W,n}^4 - 6m_H^2 m_{W,n}^2) C_0] \left(\frac{m_H^2 g_{\mu\nu}}{2} - p_\nu q_\mu \right), \quad (\text{A.37})$$

so

$$\tilde{\mathcal{A}}_W^{(n)} = -\frac{e^2 g}{16\pi^2 m_W} \left(\frac{m_W}{m_{W,n}} \right)^2 f_V(m_{W,n}). \quad (\text{A.38})$$

A.3.4 Scalar contribution

For KK number $n \geq 1$ there exist charged scalar particles a_n^\pm not seen at the SM level. At tree level these have the same masses as their W_n^\pm counterparts but loop corrections split this degeneracy.

There are three allowed diagrams at each KK level contributing to the $h \rightarrow \gamma\gamma$ amplitude that involve a charged scalar (two of them are numerically equal and are related by swapping the photon momenta):

$$i(\mathcal{A}_{a^\pm}^{(n)})_{\mu\nu} = 2 \times \left[\text{Diagram 1} \right] + \left[\text{Diagram 2} \right] \quad (\text{A.39})$$

These diagrams are exactly the same as the similar Goldstone diagrams \mathcal{A}_b and \mathcal{A}_k evaluated in the previous section, but with a different particle mass and different couplings.

Using the couplings from Sec. A.1, we get that

$$\begin{aligned} i(\mathcal{A}_{a^\pm}^{(n)})_{\mu\nu} &= -\frac{2ie^2 \lambda_{aa}}{4\pi^2} \left[\left(\frac{m_{a,n}^2 g_{\mu\nu}}{2} - \frac{m_{a,n}^2 p_\nu q_\mu}{m_H^2} \right) C_0 + \frac{g_{\mu\nu}}{4} - \frac{p_\nu q_\mu}{2m_H^2} \right] \\ &= \frac{ie^2 g}{4\pi^2 m_H^2 m_W} \left[2 \frac{m_{a,n}^2}{m_{W,n}^2} m_W^2 + m_H^2 \left(1 - \frac{m_W^2}{m_{W,n}^2} \right) \right] \left(\frac{1}{2} + m_{a,n}^2 C_0 \right) \left(\frac{m_H^2 g_{\mu\nu}}{2} - p_\nu q_\mu \right), \end{aligned} \quad (\text{A.40})$$

so

$$\tilde{\mathcal{A}}_{a^\pm}^{(n)} = -\frac{e^2 g}{16\pi^2 m_W} f_S(m_{a,n}, m_{W,n}), \quad (\text{A.41})$$

where $f_S(m_{a,n}, m_{W,n})$ is defined in Equation 4.77.

A.4 P-V functions and conventions

A.4.1 Three-point PV function

The three-point scalar Passarino-Veltman function is frequently encountered when evaluating triangle diagrams. It is defined by

$$\frac{i\pi^2}{(2\pi)^4} C_0(p^2, (p+q)^2, q^2, m_0^2, m_1^2, m_2^2) \equiv \mu^{4-D} \int \frac{d^D k}{(2\pi)^D} \{(k^2 - m_0^2)[(k+p)^2 - m_1^2][(k-q)^2 - m_2^2]\}^{-1}. \quad (\text{A.42})$$

We encounter this integral exclusively in the special case that the internal masses are equal:

$$\frac{i\pi^2}{(2\pi)^4} C_0 \equiv \mu^{4-D} \int \frac{d^D k}{(2\pi)^D} \frac{1}{\mathcal{D}}, \quad (\text{A.43})$$

where \mathcal{D} is the denominator from the general expression with $m_0 = m_1 = m_2 \equiv m$:

$$\mathcal{D} = (k^2 - m^2)[(k+p)^2 - m^2][(k-q)^2 - m^2]. \quad (\text{A.44})$$

This integral can be evaluated [55] to give

$$C_0(m) = \begin{cases} -\frac{2}{m_H^2} \left[\arcsin\left(\frac{m_H}{2m}\right) \right]^2 & m^2 \geq m_H^2/4 \\ \frac{1}{2m_H^2} \left[\ln\left(\frac{1+\sqrt{1-4m^2/m_H^2}}{1-\sqrt{1-4m^2/m_H^2}}\right) - i\pi \right]^2 & m^2 < m_H^2/4. \end{cases} \quad (\text{A.45})$$

It is convenient to define a dimensionless version of this expression:

$$c_0(m) = -\frac{m_H^2}{2} C_0(m), \quad (\text{A.46})$$

(where the normalisation matches the `fiRe` and `fiIm` functions defined in the `SLHApus` library for `CalcHEP/MicrOMEGAS` [120]).

A.4.2 Two-point PV function

We also frequently come across the scalar two-point PV function:

$$\frac{i\pi^2}{(2\pi)^4} B_0(p^2, m^2) \equiv \mu^{4-D} \int \frac{d^D k}{(2\pi)^D} \{(k^2 - m^2)[(k+p)^2 - m^2]\}^{-1}. \quad (\text{A.47})$$

We encounter the following two special cases

$$B_0(m_H^2, m^2) = \frac{1}{\epsilon} - \ln \frac{m^2}{\mu^2} + 2 - \sqrt{1 - 4m^2/m_H^2} \sqrt{2m_H^2 C_0(m)} \quad (\text{A.48})$$

and

$$B_0(0, m^2) = \frac{1}{\bar{\epsilon}} - \ln \frac{m^2}{\mu^2}, \quad (\text{A.49})$$

with $D = 4 - \epsilon$ and

$$\frac{1}{\bar{\epsilon}} = \frac{2}{\epsilon} - \gamma_E - \ln \pi, \quad (\text{A.50})$$

$\gamma_E \approx 0.57721$ being the Euler-Mascheroni constant.

A.4.3 PV Reduction

More generally, we come across three-point momentum integrals with more complex Lorentz structure that can be written generically as

$$\frac{i\pi^2}{(2\pi)^4} C^{\rho\sigma\dots\kappa} \equiv \mu^{4-D} \int \frac{d^D k}{(2\pi)^D} \frac{k^\rho k^\sigma \dots k^\kappa}{\mathcal{D}}. \quad (\text{A.51})$$

These can be simplified through ‘‘Pasarino-Veltman reduction’’ to expressions involving the scalar three-point and two-point PV functions defined in (A.45), (A.48) and (A.49); for on-shell external momenta (p^μ and q^ν) we get

$$\begin{aligned} C^{\mu\nu} &= g^{\mu\nu} C_{00} - p^\nu q^\mu C_{12} \\ g_{\rho\sigma} C^{\rho\sigma} &= DC_{00} - m_H^2 C_{12} \\ C^\mu &= -q^\mu C_2 \\ C^\nu &= p^\nu C_1. \end{aligned} \quad (\text{A.52})$$

The coefficient functions expand further to

$$\begin{aligned} C_{00} &= \frac{1}{2} m^2 C_0 + \frac{1}{4} B_0(m_H^2, m^2) + \frac{1}{4} \\ C_{12} &= \frac{m^2}{m_H^2} C_0 + \frac{1}{2m_H^2} \\ C_1 = C_2 &= \frac{B_0(m_H^2, m^2)}{m_H^2} - \frac{B_0(0, m^2)}{m_H^2}. \end{aligned} \quad (\text{A.53})$$

I used the `PaVeReduce` function in the `FeynCalc` package for `Mathematica` to check this.

Ultimately one must take the $D \rightarrow 4$ limit. Particular care must be taken in the case of C_{00} :

$$\lim_{D \rightarrow 4} DC_{00} = 4C_{00} + \lim_{\epsilon \rightarrow 0} \frac{\epsilon}{4\bar{\epsilon}} = 4C_{00} + \frac{1}{2}. \quad (\text{A.54})$$

References

- [1] G. Belanger, A. Belyaev, M. Brown, M. Kakizaki and A. Pukhov, *Higgs Phenomenology of Minimal Universal Extra Dimensions*, *EPJ Web Conf.* **28** (2012) 12070 [[1201.5582](#)].
- [2] G. Belanger, A. Belyaev, M. Brown, M. Kakizaki and A. Pukhov, *Testing Minimal Universal Extra Dimensions Using Higgs Boson Searches at the LHC*, [1207.0798](#).
- [3] A. Belyaev, M. Brown, J. Moreno and C. Papineau, *Discovering Minimal Universal Extra Dimensions (MUED) at the LHC*, [1212.4858](#).
- [4] D. Barducci, A. Belyaev, M. Brown, S. De Curtis, S. Moretti *et. al.*, *The 4-Dimensional Composite Higgs Model (4DCHM) and the 125 GeV Higgs-like signals at the LHC, (Submitted to JHEP on 10th February 2013)* (2013) [[1302.2371](#)].
- [5] A. Belyaev, M. S. Brown, R. Foadi and M. T. Frandsen, *The Technicolor Higgs in the Light of LHC Data*, [1309.2097](#).
- [6] M. S. Brown, D. Barducci, A. Belyaev, S. de Curtis, S. Moretti *et. al.*, *BSM Physics: What the Higgs Can Tell Us*, [1310.2579](#).
- [7] S. Weinberg, *A model of leptons*, *Phys. Rev. Lett.* **19** (Nov, 1967) 1264–1266.
- [8] S. Glashow, *Partial Symmetries of Weak Interactions*, *Nucl.Phys.* **22** (1961) 579–588.
- [9] G. S. Guralnik, C. R. Hagen and T. W. B. Kibble, *Global conservation laws and massless particles*, *Phys. Rev. Lett.* **13** (Nov, 1964) 585–587.
- [10] F. Englert and R. Brout, *Broken symmetry and the mass of gauge vector mesons*, *Phys. Rev. Lett.* **13** (Aug, 1964) 321–323.
- [11] B. W. Lee and J. Zinn-Justin, *Spontaneously broken gauge symmetries. i. preliminaries*, *Phys. Rev. D* **5** (Jun, 1972) 3121–3137.

- [12] G. 't Hooft and M. Veltman, *Combinatorics of gauge fields*, *Nucl.Phys.* **B50** (1972) 318–353.
- [13] G. 't Hooft and M. Veltman, *Regularization and Renormalization of Gauge Fields*, *Nucl.Phys.* **B44** (1972) 189–213.
- [14] **ATLAS** Collaboration, G. Aad *et. al.*, *Observation of a new particle in the search for the Standard Model Higgs boson with the ATLAS detector at the LHC*, *Phys.Lett.* **B716** (2012) 1–29 [[1207.7214](#)].
- [15] **CMS** Collaboration, S. Chatrchyan *et. al.*, *Observation of a new boson at a mass of 125 GeV with the CMS experiment at the LHC*, *Phys.Lett.* **B716** (2012) 30–61 [[1207.7235](#)].
- [16] **HIRES** Collaboration, D. Bird *et. al.*, *Evidence for correlated changes in the spectrum and composition of cosmic rays at extremely high-energies*, *Phys.Rev.Lett.* **71** (1993) 3401–3404.
- [17] K. F. Riley, M. P. Hobson and S. J. Bence, *Mathematical Methods for Physics and Engineering: A Comprehensive Guide*. Cambridge University Press, 3 ed., Mar., 2006.
- [18] ATLAS Collaboration, *Study of the spin of the new boson with up to 25 fb⁻¹ of atlas data*, Tech. Rep. ATLAS-CONF-2013-040, CERN, Geneva, April, 2013.
- [19] CMS Collaboration, *Properties of the observed higgs-like resonance using the diphoton channel*, Tech. Rep. CMS-PAS-HIG-13-016, CERN, Geneva, July, 2013.
- [20] CMS Collaboration, *Properties of the higgs-like boson in the decay h to zz to 4l in pp collisions at sqrt s = 7 and 8 tev*, Tech. Rep. CMS-PAS-HIG-13-002, CERN, Geneva, March, 2013.
- [21] ATLAS Collaboration, *Combined coupling measurements of the higgs-like boson with the atlas detector using up to 25 fb⁻¹ of proton-proton collision data*, Tech. Rep. ATLAS-CONF-2013-034, CERN, Geneva, March, 2013.
- [22] CMS Collaboration, *Combination of standard model higgs boson searches and measurements of the properties of the new boson with a mass near 125 gev*, Tech. Rep. CMS-PAS-HIG-13-005, CERN, Geneva, 2013.
- [23] A. Djouadi, *The Anatomy of electro-weak symmetry breaking. I: The Higgs boson in the standard model*, *Phys. Rept.* **457** (2008) 1–216 [[hep-ph/0503172](#)].
- [24] **LEP Working Group for Higgs boson searches, ALEPH Collaboration, DELPHI Collaboration, L3 Collaboration, OPAL Collaboration** Collaboration, R. Barate *et. al.*, *Search for the standard model Higgs boson at LEP*, *Phys.Lett.* **B565** (2003) 61–75 [[hep-ex/0306033](#)].

- [25] LHC Higgs Cross Section Working Group, S. Dittmaier, C. Mariotti, G. Passarino and R. Tanaka (Eds.), *Handbook of LHC Higgs Cross Sections: 1. Inclusive Observables*, CERN-2011-002 (CERN, Geneva, 2011) [[1101.0593](#)].
- [26] A. L. Read, *Modified frequentist analysis of search results (the cl_s method)*. [oai:cds.cern.ch:451614](https://cds.cern.ch/451614), .
- [27] ATLAS Collaboration, *Procedure for the lhc higgs boson search combination in summer 2011*, Tech. Rep. ATL-PHYS-PUB-2011-011, CERN, Geneva, Aug, 2011.
- [28] E. L. CROW and R. S. GARDNER, *Confidence intervals for the expectation of a poisson variable*, *Biometrika* **46** (1959), no. 3-4 441–453 [<http://biomet.oxfordjournals.org/content/46/3-4/441.full.pdf+html>].
- [29] ATLAS Collaboration, *Jet energy scale and its systematic uncertainty in proton-proton collisions at $\sqrt{s}=7$ tev with atlas 2011 data*, Tech. Rep. ATLAS-CONF-2013-004, CERN, Geneva, Jan, 2013.
- [30] G. Cacciapaglia, A. Deandrea and J. Llodra-Perez, *Higgs to Gamma Gamma beyond the Standard Model*, *JHEP* **0906** (2009) 054 [[0901.0927](#)].
- [31] I. Antoniadis, N. Arkani-Hamed, S. Dimopoulos and G. Dvali, *New dimensions at a millimeter to a Fermi and superstrings at a TeV*, *Phys.Lett.* **B436** (1998) 257–263 [[hep-ph/9804398](#)].
- [32] T. Appelquist, H.-C. Cheng and B. A. Dobrescu, *Bounds on universal extra dimensions*, *Phys.Rev.* **D64** (2001) 035002 [[hep-ph/0012100](#)].
- [33] N. Arkani-Hamed, S. Dimopoulos and G. Dvali, *The Hierarchy problem and new dimensions at a millimeter*, *Phys.Lett.* **B429** (1998) 263–272 [[hep-ph/9803315](#)].
- [34] L. Randall and R. Sundrum, *Large mass hierarchy from a small extra dimension*, *Phys. Rev. Lett.* **83** (Oct, 1999) 3370–3373.
- [35] B. A. Dobrescu and E. Poppitz, *Number of fermion generations derived from anomaly cancellation*, *Phys. Rev. Lett.* **87** (2001) 031801 [[hep-ph/0102010](#)].
- [36] T. Appelquist, B. A. Dobrescu, E. Ponton and H.-U. Yee, *Proton stability in six-dimensions*, *Phys.Rev.Lett.* **87** (2001) 181802 [[hep-ph/0107056](#)].
- [37] H.-C. Cheng, J. L. Feng and K. T. Matchev, *Kaluza-Klein dark matter*, *Phys.Rev.Lett.* **89** (2002) 211301 [[hep-ph/0207125](#)].
- [38] G. Servant and T. M. Tait, *Is the lightest Kaluza-Klein particle a viable dark matter candidate?*, *Nucl.Phys.* **B650** (2003) 391–419 [[hep-ph/0206071](#)].
- [39] A. Belyaev, N. D. Christensen and A. Pukhov, *CalcHEP 3.4 for collider physics within and beyond the Standard Model*, [1207.6082](#).

- [40] **CompHEP** Collaboration, E. Boos *et. al.*, *CompHEP 4.4: Automatic computations from Lagrangians to events*, *Nucl.Instrum.Meth.* **A534** (2004) 250–259 [[hep-ph/0403113](#)].
- [41] J. Alwall, M. Herquet, F. Maltoni, O. Mattelaer and T. Stelzer, *MadGraph 5 : Going Beyond*, *JHEP* **1106** (2011) 128 [[1106.0522](#)].
- [42] T. Hahn, *Generating Feynman diagrams and amplitudes with FeynArts 3*, *Comput.Phys.Commun.* **140** (2001) 418–431 [[hep-ph/0012260](#)].
- [43] T. Hahn and M. Perez-Victoria, *Automatized one loop calculations in four-dimensions and D-dimensions*, *Comput.Phys.Commun.* **118** (1999) 153–165 [[hep-ph/9807565](#)].
- [44] A. Semenov, *LanHEP - a package for automatic generation of Feynman rules from the Lagrangian. Updated version 3.1*, *arXiv:1005.1909* (2010) [[1005.1909](#)].
- [45] N. D. Christensen and C. Duhr, *FeynRules - Feynman rules made easy*, *Comput.Phys.Commun.* **180** (2009) 1614–1641 [[0806.4194](#)].
- [46] A. Datta, K. Kong and K. T. Matchev, *Minimal Universal Extra Dimensions in CalcHEP/CompHEP*, *New J. Phys.* **12** (2010) 075017 [[1002.4624](#)].
- [47] N. D. Christensen *et. al.*, *A comprehensive approach to new physics simulations*, [0906.2474](#).
- [48] H.-C. Cheng, K. T. Matchev and M. Schmaltz, *Radiative corrections to Kaluza-Klein masses*, *Phys. Rev.* **D66** (2002) 036005 [[hep-ph/0204342](#)].
- [49] A. Belyaev, C. Leroy, R. Mehdiyev and A. Pukhov, *Leptoquark single and pair production at LHC with CalcHEP/CompHEP in the complete model*, *JHEP* **0509** (2005) 005 [[hep-ph/0502067](#)].
- [50] A. Belyaev. Private communication.
- [51] K. Nishiwaki, K.-y. Oda, N. Okuda and R. Watanabe, *A bound on Universal Extra Dimension Models from up to 2/fb of LHC Data at 7TeV*, *Phys.Lett.* **B707** (2012) 506–511 [[1108.1764](#)].
- [52] J. R. Ellis, M. K. Gaillard and D. V. Nanopoulos, *A Phenomenological Profile of the Higgs Boson*, *Nucl.Phys.* **B106** (1976) 292.
- [53] M. A. Shifman, A. Vainshtein, M. Voloshin and V. I. Zakharov, *Low-Energy Theorems for Higgs Boson Couplings to Photons*, *Sov.J.Nucl.Phys.* **30** (1979) 711–716.
- [54] F. J. Petriello, *Kaluza-Klein effects on Higgs physics in universal extra dimensions*, *JHEP* **05** (2002) 003 [[hep-ph/0204067](#)].

- [55] G. 't Hooft and M. Veltman, *Scalar One Loop Integrals*, *Nucl.Phys.* **B153** (1979) 365–401.
- [56] M. Spira, *QCD effects in Higgs physics*, *Fortsch. Phys.* **46** (1998) 203–284 [[hep-ph/9705337](#)].
- [57] A. Azatov, R. Contino and J. Galloway, *Model-Independent Bounds on a Light Higgs*, [1202.3415](#).
- [58] G. Belanger, M. Kakizaki and A. Pukhov, *Dark matter in UED : the role of the second KK level*, [1012.2577](#).
- [59] I. Gogoladze and C. Macesanu, *Precision electroweak constraints on Universal Extra Dimensions revisited*, *Phys. Rev.* **D74** (2006) 093012 [[hep-ph/0605207](#)].
- [60] U. Haisch and A. Weiler, *Bound on minimal universal extra dimensions from anti-B \rightarrow gt; X(s)gamma*, *Phys.Rev.* **D76** (2007) 034014 [[hep-ph/0703064](#)].
- [61] **CMS** Collaboration, S. Chatrchyan *et. al.*, *Combined results of searches for the standard model Higgs boson in pp collisions at sqrt(s) = 7 TeV*, [1202.1488](#).
- [62] The ATLAS Collaboration, *An update to the combined search for the standard model higgs boson with the atlas detector at the lhc using up to 4.9 fb1 of pp collision data at 7 tev*, Tech. Rep. ATLAS-CONF-2012-019, CERN, Geneva, March, 2012.
- [63] **CMS** Collaboration, S. Chatrchyan *et. al.*, *Observation of a new boson at a mass of 125 GeV with the CMS experiment at the LHC*, *Phys.Lett.B* (2012) [[1207.7235](#)].
- [64] **ATLAS** Collaboration, G. Aad *et. al.*, *Observation of a new particle in the search for the Standard Model Higgs boson with the ATLAS detector at the LHC*, [1207.7214](#).
- [65] CMS Collaboration, *Evidence for a new state decaying into two photons in the search for the standard model higgs boson in pp collisions*, Tech. Rep. CMS-PAS-HIG-12-015, CERN, Geneva, July, 2012.
- [66] CMS Collaboration, *Evidence for a new state in the search for the standard model higgs boson in the h to zz to 4 leptons channel in pp collisions at sqrt(s) = 7 and 8 tev*, Tech. Rep. CMS-PAS-HIG-12-016, CERN, Geneva, July, 2012.
- [67] K. Agashe, R. Contino and A. Pomarol, *The Minimal composite Higgs model*, *Nucl.Phys.* **B719** (2005) 165–187 [[hep-ph/0412089](#)].
- [68] D. Barducci, A. Belyaev, S. De Curtis, S. Moretti and G. M. Pruna, *Exploring Drell-Yan signals from the 4D Composite Higgs Model at the LHC*, [1210.2927](#).

- [69] S. De Curtis, M. Redi and A. Tesi, *The 4D Composite Higgs*, *JHEP* **1204** (2012) 042 [[1110.1613](#)].
- [70] **Particle Data Group** Collaboration, J. Beringer *et. al.*, *Review of Particle Physics (RPP)*, *Phys.Rev.* **D86** (2012) 010001.
- [71] A. Carmona and F. Goertz, *Custodial Leptons and Higgs Decays*, *JHEP* **1304** (2013) 163 [[1301.5856](#)].
- [72] **CMS** Collaboration, S. Chatrchyan *et. al.*, *Search for heavy, top-like quark pair production in the dilepton final state in pp collisions at $\sqrt{s} = 7$ TeV*, *Phys.Lett.* **B716** (2012) 103–121 [[1203.5410](#)].
- [73] **CMS** Collaboration, S. Chatrchyan *et. al.*, *Search for a Vector-like Quark with Charge 2/3 in $t + Z$ Events from pp Collisions at $\sqrt{s} = 7$ TeV*, *Phys.Rev.Lett.* **107** (2011) 271802 [[1109.4985](#)].
- [74] **CMS** Collaboration, S. Chatrchyan *et. al.*, *Search for heavy bottom-like quarks in 4.9 inverse femtobarns of pp collisions at $\sqrt{s} = 7$ TeV*, *JHEP* **1205** (2012) 123 [[1204.1088](#)].
- [75] **CMS** Collaboration, *Search B' to bZ* , .
- [76] M. Cacciari, M. Czakon, M. Mangano, A. Mitov and P. Nason, *Top-pair production at hadron colliders with next-to-next-to-leading logarithmic soft-gluon resummation*, *Phys.Lett.* **B710** (2012) 612–622 [[1111.5869](#)].
- [77] A. Collaboration, *Measurements of the properties of the higgs-like boson in the two photon decay channel with the atlas detector using 25 fb⁻¹ of proton-proton collision data*, Tech. Rep. ATLAS-CONF-2013-012, CERN, Geneva, March, 2013.
- [78] G. Belanger, B. Dumont, U. Ellwanger, J. Gunion and S. Kraml, *Global fit to Higgs signal strengths and couplings and implications for extended Higgs sectors*, [1306.2941](#).
- [79] P. Bechtle, S. Heinemeyer, O. Stål, T. Stefaniak and G. Weiglein, *HiggsSignals: Confronting arbitrary Higgs sectors with measurements at the Tevatron and the LHC*, [1305.1933](#).
- [80] T. Corbett, O. Eboli, J. Gonzalez-Fraile and M. Gonzalez-Garcia, *Constraining anomalous Higgs interactions*, *Phys.Rev.* **D86** (2012) 075013 [[1207.1344](#)].
- [81] G. Cacciapaglia, A. Deandrea, G. D. La Rochelle and J.-B. Flament, *Higgs couplings beyond the Standard Model*, [1210.8120](#).
- [82] J. Espinosa, C. Grojean, M. Muhlleitner and M. Trott, *First Glimpses at Higgs' face*, *JHEP* **1212** (2012) 045 [[1207.1717](#)].

- [83] A. Azatov, R. Contino, D. Del Re, J. Galloway, M. Grassi *et. al.*, *Determining Higgs couplings with a model-independent analysis of h to $\gamma\gamma$* , *JHEP* **1206** (2012) 134 [[1204.4817](#)].
- [84] A. Azatov, R. Contino and J. Galloway, *Contextualizing the Higgs at the LHC*, [1206.3171](#).
- [85] A. Falkowski, F. Riva and A. Urbano, *Higgs At Last*, [1303.1812](#).
- [86] P. P. Giardino, K. Kannike, I. Masina, M. Raidal and A. Strumia, *The universal Higgs fit*, [1303.3570](#).
- [87] Atlas Collaboration, *An update of combined measurements of the new higgs-like boson with high mass resolution channels*, Tech. Rep. ATLAS-CONF-2012-170, CERN, Geneva, Dec, 2012.
- [88] CMS Collaboration, *Combination of standard model higgs boson searches and measurements of the properties of the new boson with a mass near 125 gev*, Tech. Rep. CMS-PAS-HIG-12-045, CERN, Geneva, 2012.
- [89] L. H. C. S. W. Group, A. David, A. Denner, M. Duehrssen, M. Grazzini *et. al.*, *LHC HXSWG interim recommendations to explore the coupling structure of a Higgs-like particle*, [1209.0040](#).
- [90] J. Espinosa, C. Grojean and M. Muhlleitner, *Composite Higgs Search at the LHC*, *JHEP* **1005** (2010) 065 [[1003.3251](#)].
- [91] S. Weinberg, *Implications of Dynamical Symmetry Breaking*, *Phys.Rev.* **D13** (1976) 974–996.
- [92] L. Susskind, *Dynamics of Spontaneous Symmetry Breaking in the Weinberg-Salam Theory*, *Phys.Rev.* **D20** (1979) 2619–2625.
- [93] K. Yamawaki, M. Bando and K.-i. Matumoto, *Scale Invariant Technicolor Model and a Technidilaton*, *Phys.Rev.Lett.* **56** (1986) 1335.
- [94] F. Sannino and K. Tuominen, *Orientifold theory dynamics and symmetry breaking*, *Phys.Rev.* **D71** (2005) 051901 [[hep-ph/0405209](#)].
- [95] D. K. Hong, S. D. Hsu and F. Sannino, *Composite Higgs from higher representations*, *Phys.Lett.* **B597** (2004) 89–93 [[hep-ph/0406200](#)].
- [96] T. Appelquist and Y. Bai, *A Light Dilaton in Walking Gauge Theories*, *Phys.Rev.* **D82** (2010) 071701 [[1006.4375](#)].
- [97] R. Foadi, M. T. Frandsen and F. Sannino, *125 GeV Higgs from a not so light Technicolor Scalar*, [1211.1083](#).

- [98] F. Giacosa, T. Gutsche and V. E. Lyubovitskij, *On the two-photon decay width of the sigma meson*, *Phys.Rev.* **D77** (2008) 034007 [[0710.3403](#)].
- [99] E. van Beveren, F. Kleefeld, G. Rupp and M. D. Scadron, *Comment on ‘Two-photon decay of the sigma meson’*, *Phys.Rev.* **D79** (2009) 098501 [[0811.2589](#)].
- [100] Kalinovsky and Volkov, *Two photon decays of scalar mesons in the quark NJL model*, *Phys.Atom.Nucl.* **73** (2010) 443–447 [[0809.1795](#)].
- [101] M. Volkov, Y. Bystritskiy and E. Kuraev, *2 gamma-decays of scalar mesons (sigma(600), f(0)(980) and a(0)(980)) in the Nambu-Jona-Lasinio model*, [0901.1981](#).
- [102] W. J. Marciano, C. Zhang and S. Willenbrock, *Higgs Decay to Two Photons*, *Phys.Rev.* **D85** (2012) 013002 [[1109.5304](#)].
- [103] **Particle Data Group** Collaboration, S. Eidelman *et. al.*, *Review of particle physics. Particle Data Group*, *Phys.Lett.* **B592** (2004) 1.
- [104] S. S. Wilks, *The large-sample distribution of the likelihood ratio for testing composite hypotheses*, *The Annals of Mathematical Statistics* **9** (1938), no. 1 pp. 60–62.
- [105] G. Cowan, K. Cranmer, E. Gross and O. Vitells, *Asymptotic formulae for likelihood-based tests of new physics*, *European Physical Journal C* **71** (Feb., 2011) 1554 [[1007.1727](#)].
- [106] A. R. Zerwekh, *Associate higgs and gauge boson production at hadron colliders in a model with vector resonances*, *Eur.Phys.J.* **C46** (2006) 791–795 [[hep-ph/0512261](#)].
- [107] A. Belyaev, R. Foadi, M. T. Frandsen, M. Jarvinen, F. Sannino *et. al.*, *Technicolor Walks at the LHC*, *Phys.Rev.* **D79** (2009) 035006 [[0809.0793](#)].
- [108] F. Boudjema, G. Cacciapaglia, K. Cranmer, G. Dissertori, A. Deandrea *et. al.*, *On the presentation of the LHC Higgs Results*, [1307.5865](#).
- [109] E. Witten, *An SU(2) Anomaly*, *Phys.Lett.* **B117** (1982) 324–328.
- [110] D. D. Dietrich, F. Sannino and K. Tuominen, *Light composite Higgs from higher representations versus electroweak precision measurements: Predictions for CERN LHC*, *Phys.Rev.* **D72** (2005) 055001 [[hep-ph/0505059](#)].
- [111] M. A. Luty, *Strong Conformal Dynamics at the LHC and on the Lattice*, *JHEP* **0904** (2009) 050 [[0806.1235](#)].
- [112] T. A. Ryttov and F. Sannino, *Ultra Minimal Technicolor and its Dark Matter TIMP*, *Phys.Rev.* **D78** (2008) 115010 [[0809.0713](#)].

- [113] K. D. Lane and E. Eichten, *Two Scale Technicolor*, *Phys.Lett.* **B222** (1989) 274.
- [114] E. Farhi and L. Susskind, *A Technicolored G.U.T.*, *Phys.Rev.* **D20** (1979) 3404–3411.
- [115] F. Bursa, L. Del Debbio, L. Keegan, C. Pica and T. Pickup, *Mass anomalous dimension in $SU(2)$ with six fundamental fermions*, *Phys.Lett.* **B696** (2011) 374–379 [[1007.3067](#)].
- [116] H. Ohki, T. Aoyama, E. Itou, M. Kurachi, C.-J. D. Lin *et. al.*, *Study of the scaling properties in $SU(2)$ gauge theory with eight flavors*, *PoS LATTICE2010* (2010) 066 [[1011.0373](#)].
- [117] M. Hayakawa, K.-I. Ishikawa, Y. Osaki, S. Takeda and N. Yamada, *Lattice study on two-color QCD with six flavors of dynamical quarks*, *PoS LATTICE2012* (2012) 040 [[1210.4985](#)].
- [118] Z. Fodor, K. Holland, J. Kuti, D. Negradi, C. Schroeder *et. al.*, *The sextet gauge model, light Higgs, and the dilaton*, *PoS LATTICE2012* (2012) 024 [[1211.6164](#)].
- [119] Z. Fodor, K. Holland, J. Kuti, D. Negradi, C. Schroeder *et. al.*, *Can the nearly conformal sextet gauge model hide the Higgs impostor?*, *Phys.Lett.* **B718** (2012) 657–666 [[1209.0391](#)].
- [120] G. Belanger, N. D. Christensen, A. Pukhov and A. Semenov, *SLHAplus: a library for implementing extensions of the standard model*, [1008.0181](#).